January 2015

Modeling and Direct Adaptive Robust Control of Flexible Cable-Actuated Systems

Jayender Rajgopal Bhardhwaj
Purdue University

Graduate School Form 30
Updated 1/15/2015

PURDUE UNIVERSITY
GRADUATE SCHOOL
Thesis/Dissertation Acceptance

This is to certify that the thesis/dissertation prepared

By Jayender Rajgopal Bhardhwaj

Entitled
MODELING AND DIRECT ADAPTIVE ROBUST CONTROL OF FLEXIBLE CABLE-ACTUATED SYSTEMS

For the degree of Doctor of Philosophy

Is approved by the final examining committee:

BIN YAO
Chair

DANIEL DELAURENTIS

PETER H. MECKL

GEORGE T.C. CHIU

To the best of my knowledge and as understood by the student in the Thesis/Dissertation Agreement, Publication Delay, and Certification Disclaimer (Graduate School Form 32), this thesis/dissertation adheres to the provisions of Purdue University's "Policy of Integrity in Research" and the use of copyright material.

Approved by Major Professor(s): BIN YAO

Approved by: GANESH SUBBARAYAN 7/1/2015
Head of the Departmental Graduate Program Date

MODELING AND DIRECT ADAPTIVE ROBUST CONTROL OF FLEXIBLE CABLE-ACTUATED SYSTEMS

A Dissertation

Submitted to the Faculty

of

Purdue University

by

Jayender Bhardhwaj

In Partial Fulfillment of the

Requirements for the Degree

of

Doctor of Philosophy

August 2015

Purdue University

West Lafayette, Indiana

To my loving wife and parents
whose patience and support made this possible.

ACKNOWLEDGMENTS

I would like to thank my advisor Dr. Bin Yao for his insightful guidance, support and feedback on my research that helped fuel my motivation.

I also appreciate the interest shown by Dr. Arvind Raman and his guidance during the initial stages of my work.

I would also like to thank my committee members Dr. George Chiu, Dr. Peter Meckl and Dr. Daniel DeLaurentis for their time and valuable feedback.

I am very grateful to the Mechanical Engineering staff including Paul Niles and Bert Gramelspacher from the electronic shop, John Wheeler and Adam Krichbaum from the machine shop and Jill Clauson from the business office for their help.

TABLE OF CONTENTS

Page

LIST OF TABLES

LIST OF FIGURES

SYMBOLS

A	cross sectional area of cable
c_u	longitudinal linear wave velocity
c_w	transverse linear wave velocity
dl	cable element before pre-stretch
dx	cable element after pre-stretch
ds	cable element during operation of system
dt	time increment used for simulation
E	young's modulus of cable material
ϵ_0	cable strain due to equilibrium tension
ϵ	true cable strain
g	acceleration due to gravity
J_1	rotational moment of inertia of drive pulley
J_2	rotational moment of inertia of load pulley
L	length of cable between pulleys under no tension
L_e	length of cable between pulleys under equilibrium tension
λ	apparent cable strain
ρ	linear mass density of cable
r_1	radius of drive pulley
r_2	radius of load pulley
σ	Courant-Friedrichs-Lewy number
τ	drive motor torque
T_0	cable equilibrium tension
$T_1(x_1, t)$	net tension at point x_1 at time t
$T_2(x_2, t)$	net tension at point x_2 at time t
θ_1	angle of rotation of left pulley w.r.t. Z_1 axis

θ_2	angle of rotation of right pulley w.r.t. Z_1 axis
$u_1(x_1, t)$	displacement of point on cable 1 located at x_1 in the X_1 direction
$u_2(x_2, t)$	displacement of point on cable 2 located at x_2 in the X_2 direction
$v_1(x_1, t)$	displacement of point on cable 1 located at x_1 in the Y_1 direction
$v_2(x_2, t)$	displacement of point on cable 2 located at x_2 in the Y_2 direction
$w_1(x_1, t)$	displacement of point on cable 1 located at x_1 in the Z_1 direction
$w_2(x_2, t)$	displacement of point on cable 2 located at x_2 in the Z_2 direction
x_1	distance of a point along cable 1 from drive pulley at equilibrium
x_2	distance of a point along cable 2 from load pulley at equilibrium

NOMENCLATURE

u_1'	$\frac{\partial u_1(x_1,t)}{\partial x_1}$
u_2'	$\frac{\partial u_2(x_2,t)}{\partial x_2}$
v_1'	$\frac{\partial v_1(x_1,t)}{\partial x_1}$
v_2'	$\frac{\partial v_2(x_2,t)}{\partial x_2}$
w_1'	$\frac{\partial w_1(x_1,t)}{\partial x_1}$
w_2'	$\frac{\partial w_2(x_2,t)}{\partial x_2}$
u_1''	$\frac{\partial^2 u(x_1,t)}{\partial x_1^2}$
u_2''	$\frac{\partial^2 u(x_2,t)}{\partial x_2^2}$
v_1''	$\frac{\partial^2 v(x_1,t)}{\partial x_1^2}$
v_2''	$\frac{\partial^2 v(x_2,t)}{\partial x_2^2}$
w_1''	$\frac{\partial^2 w(x_1,t)}{\partial x_1^2}$
w_2''	$\frac{\partial^2 w(x_2,t)}{\partial x_2^2}$
$\dot{u}_1$	$\frac{\partial u_1(x_1,t)}{\partial t}$
$\dot{u}_2$	$\frac{\partial u_2(x_2,t)}{\partial t}$
$\dot{v}_1$	$\frac{\partial v_1(x_1,t)}{\partial t}$
$\dot{v}_2$	$\frac{\partial v_2(x_2,t)}{\partial t}$
$\dot{w}_1$	$\frac{\partial w_1(x_1,t)}{\partial t}$
$\dot{w}_2$	$\frac{\partial w_2(x_2,t)}{\partial t}$
$\ddot{u}_1$	$\frac{\partial^2 u_1(x_1,t)}{\partial t^2}$
$\ddot{u}_2$	$\frac{\partial^2 u_2(x_2,t)}{\partial t^2}$
$\ddot{v}_1$	$\frac{\partial^2 v_1(x_1,t)}{\partial t^2}$
$\ddot{v}_2$	$\frac{\partial^2 v_2(x_2,t)}{\partial t^2}$
$\ddot{w}_1$	$\frac{\partial^2 w_1(x_1,t)}{\partial t^2}$
$\ddot{w}_2$	$\frac{\partial^2 w_2(x_2,t)}{\partial t^2}$

ABSTRACT

Bhardhwaj, Jayender PhD, Purdue University, August 2015. Modeling and Direct Adaptive Robust Control of Flexible Cable-Actuated Systems. Major Professor: Bin Yao, School of Mechanical Engineering.

Cable-actuated systems provide an effective method for precise motion transmission over various distances in many robotic systems. In general, the use of cables has many potential advantages such as high-speed manipulation, larger payloads, larger range of motion, access to remote locations and applications in hazardous environments. However, cable flexibility inevitably causes vibrations and poses a concern in high-bandwidth, high-precision applications.

Cable vibrations typically occur in both the longitudinal and mutually perpendicular transverse directions and are coupled. The coupling between longitudinal and transverse modes is usually assumed to be minimal since longitudinal resonances are usually at much higher frequencies compared to transverse frequencies. In a cable-pulley system, the coupling between the cable and high-inertia components such as pulleys can lead to a drastic reduction in the fundamental longitudinal mode. This coupling becomes more prominent under conditions of autoparametric or internal resonance in the system. When these conditions are met, transverse cable vibrations and pulley rotations exchange significant energy leading to higher amplitudes of oscillations not predicted by classical linear analyses. The design parameters needed to facilitate autoparametric resonance are further examined through a parametric analysis of the system.

The coupled cable-pulley dynamics are derived and the flexible modes of the overall system are calculated analytically and verified experimentally. In the system examined, the dominant resonance mode is caused by cable elasticity and cannot be ignored in high-bandwidth high-precision applications. This is in contrast to most robot ma-

nipulators where the resonant modes are assumed to be dominated either by joint or link flexibility. Experimental observations of the system's frequency response are used to model the cables as axial springs and a trajectory tracking problem is formulated using a lumped parameter model of the system with matched uncertainty in the drive motor dynamics as well as unmatched uncertainty in the load pulley dynamics. The controller is constructed using a Lyapunov-type direct adaptive robust control (DARC) framework with necessary design modifications to accommodate uncertain and non-smooth nonlinearities in the system. The proposed controller guarantees prescribed output-tracking transient performance as well as final tracking accuracy in the presence of both parametric uncertainties and other uncertain nonlinearities. Experimental results are presented to demonstrate its effectiveness.

1. INTRODUCTION

1.1 Overview and Motivation

Cable-actuated systems are extensively used for the manipulation of a variety of robotic devices such as rehabilitative devices [1], remote telemanipulators [2], micro air vehicles [3] and robotic hands ([4], [5]). Some of these examples are shown in Figure 1.1. Cable-actuation also has many uses in transporter systems such as high-rise elevators [57], cranes [6] and cable-cars [7] as shown in Figure 1.2. In the case of cable-driven parallel manipulators, an end-effector is usually connected in parallel to a number of actuators using cables and controlled using cable forces which are constrained to be tensile. This is in contrast to a serial link structure where the base actuator would need to support the inertia of the entire structure as well as any payload, resulting in either a heavy robot with large actuators or slow speed. Serial link structures also have the disadvantage of accumulating joint angle errors leading to lower positioning accuracy. Cables provide a useful alternative to rigid links commonly used in robotic manipulators. In general, the use of cables has many potential advantages such as high-speed manipulation [8], larger payloads, larger range of motion, access to remote locations and applications in hazardous environments [9]. They are also easier to transport, assemble/disassemble and reconfigure.

Since the cables used in such systems are flexible, they can vibrate in both the axial and transverse directions leading to loss of performance and stability. This may be an important concern especially in applications requiring high bandwidth or high stiffness. Cable vibrations are a highly nonlinear and coupled phenomenon and the effect of their vibrations on the performance of some of these applications has only been partially studied. In this work, a prototypical cable-pulley system is proposed

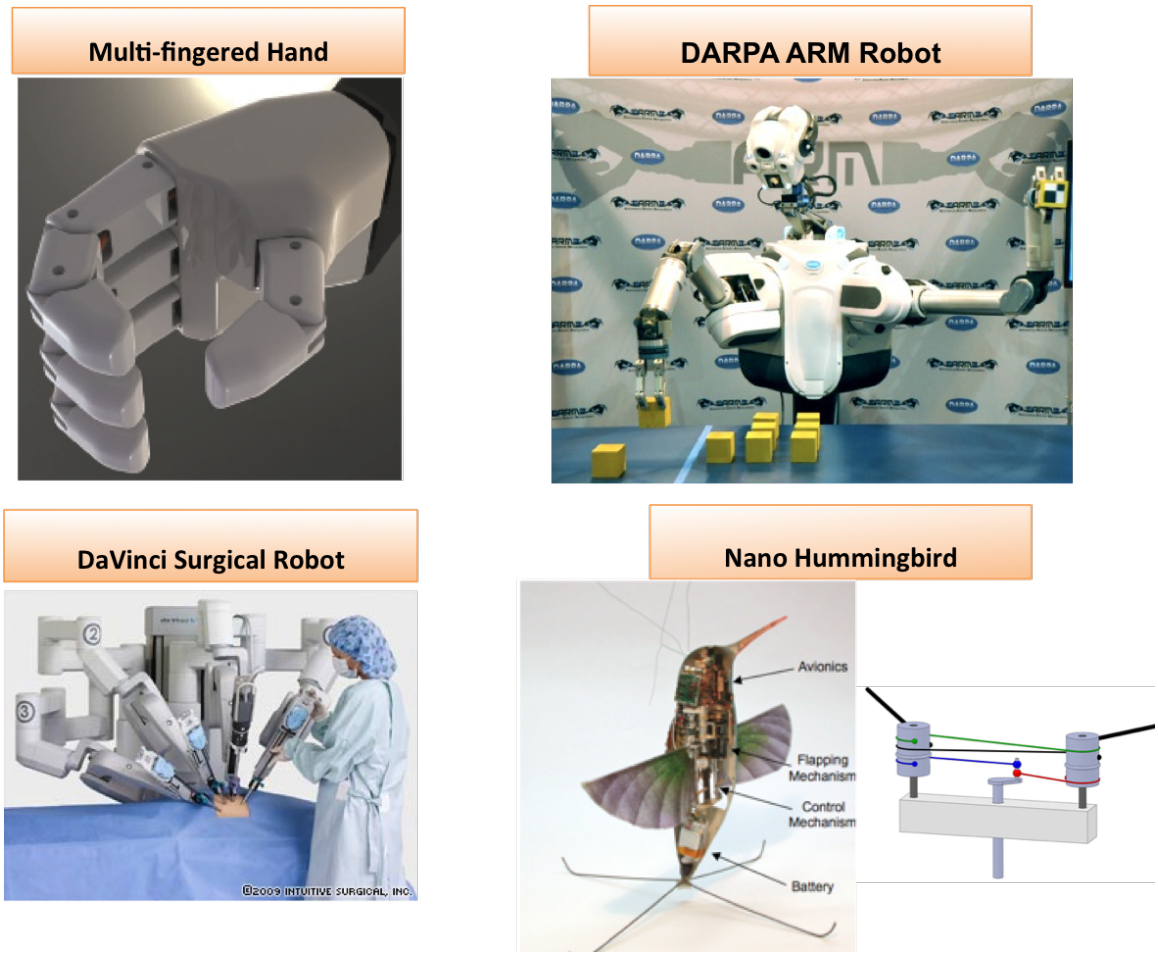

Figure 1.1. Cable-driven technologies.

and the nature of nonlinear cable vibrations and the effect of cable flexibility on the system's overall stiffness is studied in detail.

1.2 Literature Review

1.2.1 Flexible Cable Modeling

Some of the earliest analyses of the free vibrations of a string with fixed ends and time-varying tension was performed by Carrier ([11], [12]) and solved using the per-

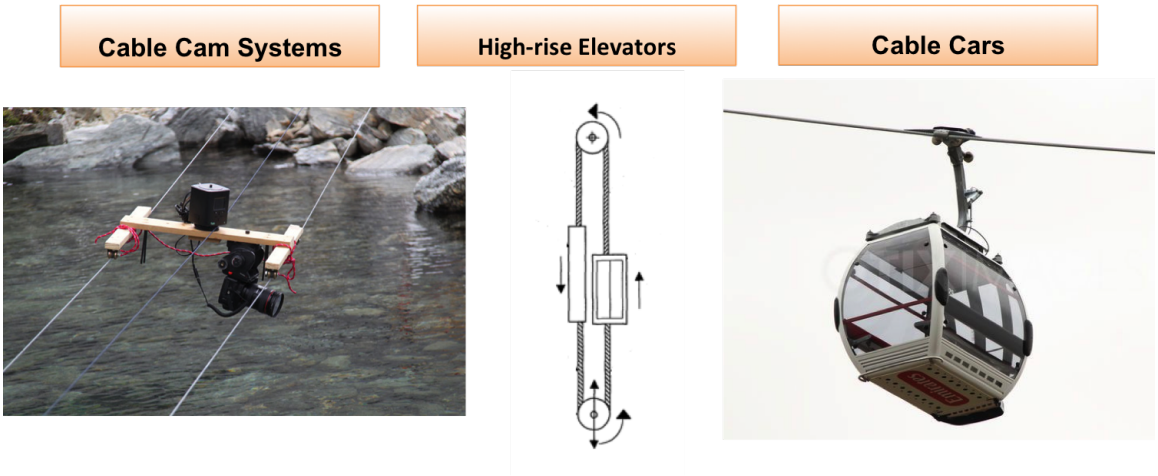

Figure 1.2. Cable-transporter systems.

turbation method assuming that the amplitude of oscillations is small. Coulson and Jeffrey [13] derived the nonlinear wave equation for transverse vibrations of a flexible string fixed at both ends, under constant equilibrium tension. The equations are simplified to the standard second order wave equation and solved using D'Alembert's method for cases without sudden changes in displacement. Gottlieb [18] presented modal solutions to Coulson's equation after modifying it to include both small and large vibrations. The derived partial differential equation is different from the one derived earlier by Carrier. Some common assumptions of flexible cable motion include small slopes, small displacements compared to the string length, constant or small changes in tension compared to the equilibrium value, negligible longitudinal motion and planar motion. Classical linear derivations of the wave equation governing cable motion can be found in ([13], [14]). The boundary condition that allows for constant tension was described by Morse and Ingard [14]. In general, there has been some inconsistency in the governing equations for nonlinear vibrations of strings due to the different assumptions made. Narasimha [20] examined these assumptions while formulating more exact equations of string motion starting with the tension-

displacement relationship which takes into account the cross-sectional area change in the string due to stretching.

Naturally occurring practical examples of nonlinear vibrating systems are more common today. It is well known that transverse vibrations of a stretched string induce axial motion which causes changes in tension. These changes in tension can in turn lead to coupling between mutually perpendicular transverse modes of a cable. Murthy and Ramakrishna [16] presented an analysis of a pair of coupled nonlinear partial differential equations for the two components of transverse motion of the string. In the absence of a second component of transverse displacement, the equations reduce to one given earlier by Lee [15]. In both cases longitudinal vibrations were ignored and the string slopes were assumed small. Anand [17] showed that for nonplanar cable vibration, the curve traced by a point on the cable in the transverse directions is an ellipse with slowly rotating and shrinking axes. Small displacements and gradients were assumed while longitudinal motion was approximated assuming that the frequency spectrum of the driving force was well below the lowest longitudinal resonance frequency. Gottlieb studied the forced [18] and free [19] transverse vibrations of a constant-tension string with an emphasis on whirling solutions. The coupling between transverse and longitudinal vibrations in stretched strings was studied in [21]- [23]. Kurmyshev [21] discussed the parametric generation of a second transverse spatial mode caused by transverse and longitudinal mode coupling. More recently, Agrawal [24] numerically simulated transverse-longitudinal coupling in a flexible cable-transporter system assuming small vibrations. In general, the assumption that longitudinal vibrations are small compared to the transverse and the neglect of transverse-longitudinal vibration coupling in cables is very common. Such an approximation is valid only in applications where transverse and longitudinal resonances occur at very different frequencies thereby ensuring a lack of interaction between them. It may not be possible to ignore this coupling in systems where the motion of continuous flexible cables is closely coupled with discrete high-inertia components.

Systems where flexible cables are coupled with high-inertia components require a closer study since the presence of such components affects the overall natural frequencies of the system. Many studies of bandsaw systems were done by Mote ([25]- [27]) in which he examined axially moving belts with finite bending stiffness. Vibration coupling between two band spans in a band supported by two wheels was found to occur and caused by the finite curvature of the spans. The coupling was found to reduce with increased tension as the spans became more straight. The same coupling was reportedly not observed when the belt was replaced by a string with negligible bending stiffness. The natural vibration modes of a serpentine belt drive system was investigated by Beikmann et al. [29] taking into account the effect of belt and pulley coupling. This study helped establish the relationship between the longitudinal vibration modes of a cable-driven system and discrete high-inertia components. The possibility of parametric excitation in the same system was explored in a following study by Beikmann [30].

1.2.2 Autoparametric Resonance

The phenomenon of parametric excitation of vibrations was first treated theoretically by Lord Rayleigh ([31], [32]) who showed that if the tension of a stretched wire is varied periodically at twice one of its transverse mode frequencies, then the system is unstable and oscillations grow. Elliot ([33], [34]) analyzed the parametric coupling of two polarizations of transverse oscillation in stretched strings and showed the spontaneous exchange of energy between the perpendicular modes. Approximate solutions to Murthy's [16] equations give a good description of the observed resonance response, hysteresis, the jump phenomenon and tubular motion in stretched strings. It is shown that when a driving force approaches transverse resonance frequency, the amplitude of vibrations increases causing the tension to vary, making the string motion essentially nonlinear even for small driving forces. More experimental studies of parametric excitation was done by Rao [35]. Most of these theoretical

and experimental studies focus on the internal resonance of cable vibrations under forced external excitations where the frequency and amplitude of the driving force can be changed or controlled based on the system's natural frequencies. This is in contrast to the study of flexible systems where internal resonance between transverse and longitudinal modes is inherent and is known as autoparametric resonance.

The study of autoparametric resonance is relatively recent compared to the study of cable vibrations and the best known example of such a system is the elastic pendulum [37]. Beikmann et al. [30] also studied the coupling between transverse vibration of a cable span and rotational oscillation of a pulley in a serpentine belt drive system. The conditions for autoparametric resonance were explored along with its effect on engine performance at critical belt speeds. Though only steady state experiments were performed, some predictions were made on the coupling and growth of transient vibrations using simulations. Tondl [36] presents a study of autoparametric resonance in many mechanical systems. Autoparametric resonance in a cable-stayed beam structure was studied by Fujino [38] in the context of suspension bridges. Bhardhwaj and Yao [39] studied autoparametric resonance in a cable-pulley system used for motion transmission and positioning. The parametric conditions leading to strong coupling between transverse and rotational modes of the system were studied in detail. Suggestions for the design of similar robotic manipulators were made in order to avoid internal resonance.

1.2.3 Control Design

There has been some research effort on motion control of cable-actuated systems that focuses on the suppression of either longitudinal or transverse cable vibrations individually while ignoring the coupling between them. Control of transverse vibrations has been more widely studied in cable-actuated systems [60]- [64] and axially moving cable systems [67], [63]. While active control schemes have been shown to improve desired performance, both passive and active controllers have been proposed

with a focus on stabilizing the system by dampening the transverse vibrations through energy dissipation. Some of these schemes are boundary-control strategies designed to use measurements of cable displacement, velocity, slope or its time derivative at the actuated end and are hard or impractical to implement.

In contrast, longitudinal vibration suppression in cable-driven systems has been less studied due to the associated frequencies being much higher than the required bandwidth. In [57], residual longitudinal vibrations in high-rise elevators were dampened using an open-loop controller and a differential-difference equation relating actuator input to the output position. Agrawal [58] proposed the attenuation of residual longitudinal vibrations in a cable transporter system using an LQG controller. An approximate finite-dimensional model of the system was used. Many feedforward command shaping techniques have also been proposed to control residual vibrations in rigid link robot manipulators. The goal in the above studies was residual vibration dampening using a simplified controller for point-to-point motion and not precise motion tracking. The dominant flexible mode of the cable-pulley system studied here is caused by cable elasticity unlike most prior work where the focus is on joint or link flexibility [40]- [47]. Experimental results have been used to prove the validity of approximating cables as axial springs. As a result, the overall cable-pulley system is approximated using a lumped parameter model either as a 2-mass spring or a 3-mass spring problem.

Traditionally, many control schemes have been proposed for vibration control in 2-mass spring problems. Hamamoto [70] and Kawanishi [71] used LMI optimization to propose controllers that satisfy H_∞ performance and pole-placement assignment in a prescribed region, in the presence of physical parameter perturbations. The above approaches require modeling all performance specifications using LMIs, which can be difficult. Limitations on control effort were considered by Braatz [72] and Wolfgang [74], using μ synthesis and H_∞ loop shaping design, respectively. They presented simulation results for the stabilization of an undamped pair of coupled masses with a noncollocated sensor and actuator. A robust controller was designed

by Mario [73] using mixed l_∞/H_∞ optimization to include time-domain specifications. These approaches resulted in a complex controller of very high order and are usually hard to implement. Moreover, since they are not adaptive in nature, i.e., unknown parameters are not estimated, the designed controllers are more conservative than required. Reducing the controller order leads to relaxing of some performance specifications. Lastly, reducing the control effort through optimization requires proper weight selection and multiple trial-and-error iterations. Simulation results have been presented by Xu [75] for the suppression of torsional vibrations in an electric motor drive system using LQR. Disturbances and uncertainties were not considered. A hybrid model predictive controller was used by Takodoro [76] for position control of a 2-mass spring system with static and kinetic friction. Though simulation results were presented, the proposed controller requires a precise system model with accurate parameter estimates that are rarely available in practice. An adaptive backstepping control approach was proposed and simulated by Liu [77] for the velocity regulation of 2-mass-spring systems with load uncertainty. The formulation is very specific to velocity regulation and cannot be extended easily to position tracking. Also, since the parameter adaptation may not be bounded in the presence of modeling errors and other uncertain nonlinearities, the closed-loop stability is not guaranteed experimentally. In contrast, a direct adaptive robust controller was designed for position tracking of a flexible cable-pulley system by Bhardhwaj and Yao [79] that achieved guaranteed output-tracking transient performance as well as final tracking accuracy, in the presence of matched model uncertainties. This adaptive robust control design strategy has also been extended to a cable-pulley system with unmatched model uncertainties.

1.3 Research Contributions

In this research, the behavior of a prototypical cable-pulley system is studied in the context of cable-actuated robots used for motion transmission. Flexible cable

modeling shows the presence of strong coupling phenomena that can affect remote position tracking performance. Both analytical and simulation results are used to calculate the vibration modes of the overall cable-pulley system. Experiments have been used to validate key results leading to a better understanding of modeling approximations made to simplify control design without losing fidelity of the model. Extensive experimental work has also been done in the area of control design and implementation for position tracking at high bandwidths. The main contributions of this work are summarized as follows:

1. The governing equations of cable vibrations are studied without the simplifying assumptions made in most prior work. The dynamics are then carefully simplified to a weakly nonlinear form which is still capable of representing key nonlinear coupling phenomena.

2. The longitudinal vibration modes of a cable-pulley system are calculated and it is shown that the fundamental natural frequency of the system is a function of cable as well as pulley properties. As a result, a large reduction in the fundamental frequency is predicted analytically and validated experimentally. Unlike cable-driven robots studied before, this fundamental mode is shown to dominate other modes of the system caused by joint or link flexibility.

3. The phenomenon of autoparametric resonance in the cable-pulley system has been explored and strong coupling between transverse cable vibrations and pulley rotations has been observed. The physical parameters necessary to facilitate internal resonance are studied with implications to the design of such systems.

4. A clear distinction has been made between vibration modes of the system caused by joint flexibility and cable elasticity. Experimental results are used to validate a reduced-order lumped parameter model of the overall system without losing model fidelity. An adaptive robust controller is designed and implemented to achieve very good position tracking performance at high bandwidth in the presence of both parametric uncertainties and uncertain nonlinearities.

1.4 Organization

In Chapter 2, the exact dynamics of flexible cable vibrations are derived without the simplifying assumptions made in most prior work. A carefully simplified weakly nonlinear form of the dynamics is also derived to retain key coupling phenomena. The pulley dynamics along with cable boundary conditions are described in order to fully define the governing equations of a cable-pulley system. Lastly, a stable finite difference scheme necessary for numerical simulation of the overall system is specified.

In Chapter 3, the vibration modes of the cable-pulley system are calculated analytically using modal analysis and validated experimentally. The analysis is extended to a cable-transporter system. The implications of the fundamental vibration mode on future analysis of such systems are discussed.

In Chapter 4, the experimental setup and its components are described in detail. The parameters of the motor and load are identified using linear least square methods. Further experimental results on the system's frequency response are used to validate the parameters.

Chapter 5 explores the conditions of autoparametric resonance in the cable-pulley system. The constraints on the physical parameters of the system needed to ensure autoparametric resonance are used to suggest implications on design through a parametric analysis. Experiments on the free and forced vibrations of the system are used to show the effect of autoparametric resonance through strong coupling between transverse cable vibrations and pulley rotations.

In Chapter 6, reduced-order lumped parameter models of the overall cable-pulley system are defined. Frequency response experiments are used to model the cables as axial springs. A clear distinction is made between flexible modes of the system due to cable elasticity and joint flexibility with the former being dominant. A direct adaptive robust controller is designed for precise position tracking assuming both matched uncertainty in the drive motor dynamics and unmatched uncertainty in the

load pulley dynamics. High closed-loop bandwidth is achieved in the presence of both parametric uncertainty and uncertain nonlinearities.

Chapter 7 concludes the research work presented here and discusses possible directions for future work in this area.

2. SYSTEM DYNAMICS

In the following section, the nonplanar coupled dynamic equations for a stretched flexible cable are derived without simplifying assumptions.

2.1 Exact Nonlinear Cable Dynamics

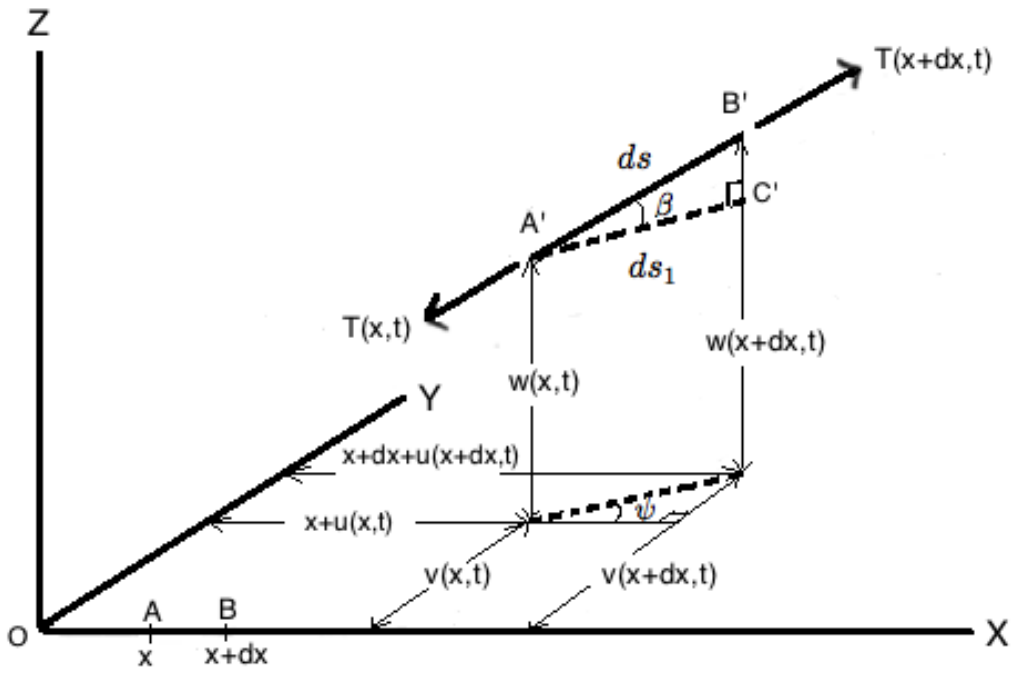

Figure 2.1. Cable element stretched during vibration.

We first consider an unstretched cable segment of length dl. When subject to a constant equilibrium tension T_0, the segment is stretched to a length dx. We represent this element of length dx by the segment AB shown in Figure 2.1 and assume it to be along the X axis for simplicity. The equilibrium strain in the element can hence be calculated as the ratio of change in length to original length as follows:

$$\epsilon_0 = \frac{dx - dl}{dl} = \frac{dx}{dl} - 1 \tag{2.1}$$

During vibrations of the cable, the segment AB of length dx changes further to the segment $A'B'$ of length ds as shown in Figure 2.1. We define the displacements of point A parallel to the X, Y and Z axes to be $u(x,t)$, $v(x,t)$ and $w(x,t)$, respectively. Similarly, the displacements of point B are $u(x+dx,t)$, $v(x+dx,t)$ and $w(x+dx,t)$. Hence the coordinates of A, B, A', B' are as follows:

$$\begin{aligned}
A \quad & (x, 0, 0) \\
B \quad & (x + dx, 0, 0) \\
A' \quad & (x + u(x,t), v(x,t), w(x,t)) \\
B' \quad & (x + dx + u(x + dx, t), v(x + dx, t), w(x + dx, t))
\end{aligned}$$

As shown in Figure 2.1, $A'C'$ is the projection of $A'B'$ on the XY plane and has length ds_1. The net strain on AB can be calculated as the sum of the equilibrium strain ϵ_0 and the added strain due to cable vibration. Since the original length used to calculate the added strain is still dl, the net strain is given by,

$$\epsilon(x,t) = \epsilon_0 + \frac{ds - dx}{dl} \tag{2.2}$$

Based on the coordinates of A, B, A', B', the stretched length ds of the cable segment is given by,

$$\begin{aligned}
ds = \Big(& (u(x + dx, t) + dx - u(x,t))^2 + (v(x + dx, t) - v(x,t))^2 \\
& + (w(x + dx, t) - w(x,t))^2 \Big)^{\frac{1}{2}}
\end{aligned} \tag{2.3}$$

Using Taylor expansion,

$$u(x+dx,t) = u(x,t) + u'dx + O(dx^2) \tag{2.4a}$$

$$v(x+dx,t) = v(x,t) + v'dx + O(dx^2) \tag{2.4b}$$

$$w(x+dx,t) = w(x,t) + w'dx + O(dx^2) \tag{2.4c}$$

where

$$u' = \frac{\partial u(x,t)}{\partial x} \tag{2.5a}$$

$$v' = \frac{\partial v(x,t)}{\partial x} \tag{2.5b}$$

$$w' = \frac{\partial w(x,t)}{\partial x} \tag{2.5c}$$

Assuming that the cable segment dx is infinitesimally small, powers of dx greater than 2 are ignored. Substituting Eq. (2.4) in Eq. (2.3) we get the stretched segment length ds as,

$$ds = dx\sqrt{(1+u')^2 + v'^2 + w'^2} \tag{2.6}$$

Defining the apparent strain measured with respect to the equilibrium configuration of the cable as λ,

$$\lambda = \frac{ds}{dx} - 1 = \sqrt{(1+u')^2 + v'^2 + w'^2} - 1 \tag{2.7}$$

Substituting for ds from Eq. (2.6) in Eq. (2.2) the net strain in the cable segment is given by,

$$\epsilon(x,t) = \epsilon_0 + \frac{dx}{dl}\left(\sqrt{(1+u')^2 + v'^2 + w'^2} - 1\right) \tag{2.8}$$

Using the equilibrium strain in Eq. (2.1), the true strain in the cable is defined from Eq. (2.2) and Eq. (2.6) to be,

$$\epsilon(x,t) = \epsilon_0 + (1+\epsilon_0)\left(\sqrt{(1+u')^2 + v'^2 + w'^2} - 1\right) \tag{2.9}$$

Assuming only that net cable strain is small enough for Hooke's law to be valid, the net tension in the cable at the point originally at x is given by,

$$\begin{aligned} T(x,t) &= EA\epsilon(x,t) \\ &= T_0 + EA(1+\epsilon_0)\left(\sqrt{(1+u')^2+v'^2+w'^2}-1\right) \end{aligned} \tag{2.10}$$

where E is Young's modulus of the cable material and A is the area of cross section. From Figure 2.1, the X, Y and Z components of the tension can be obtained as follows:

$$T_x = T\cos\beta\cos\psi \tag{2.11a}$$

$$T_y = T\cos\beta\sin\psi \tag{2.11b}$$

$$T_z = T\sin\beta \tag{2.11c}$$

From the geometry in Figure 2.1, we also observe the following geometric relationships:

$$\sin\beta = \frac{B'C'}{A'B'} = \frac{w(x+dx,t)-w(x,t)}{ds} = w'\frac{dx}{ds} \tag{2.12a}$$

$$\cos\beta = \frac{ds_1}{ds} \tag{2.12b}$$

$$\cos\psi = \frac{u(x+dx,t)+dx-u(x,t)}{ds_1} = (1+u')\frac{dx}{ds_1} \tag{2.12c}$$

$$\sin\psi = \frac{v(x+dx,t)-v(x,t)}{ds_1} = v'\frac{dx}{ds_1} \tag{2.12d}$$

Substituting Eq. (2.12) in Eq. (2.11), we get the tension components as

$$T_x = T(1+u')\frac{dx}{ds} = \frac{T(1+u')}{\sqrt{(1+u')^2+v'^2+w'^2}} \tag{2.13a}$$

$$T_y = Tv'\frac{dx}{ds} = \frac{Tv'}{\sqrt{(1+u')^2+v'^2+w'^2}} \tag{2.13b}$$

$$T_z = Tw'\frac{dx}{ds} = \frac{Tw'}{\sqrt{(1+u')^2+v'^2+w'^2}} \tag{2.13c}$$

In the absence of gravity and cable damping forces, the dynamics of the cable element can be obtained by equating the net tension force in each direction to the rate of change of momentum ([11], [12]).

$$\rho\ddot{u}(x,t) = \frac{\partial T_x}{\partial x} = \frac{\partial T}{\partial x}\frac{(1+u')}{\lambda+1} + T\frac{\partial}{\partial x}\frac{(1+u')}{\lambda+1} \tag{2.14a}$$

$$\rho\ddot{v}(x,t) + \Gamma\rho\dot{v}(x,t) = \frac{\partial T_y}{\partial x} = \frac{\partial T}{\partial x}\frac{v'}{\lambda+1} + T\frac{\partial}{\partial x}\frac{v'}{\lambda+1} \tag{2.14b}$$

$$\rho\ddot{w}(x,t) + \Gamma\rho\dot{w}(x,t) = \frac{\partial T_z}{\partial x} = \frac{\partial T}{\partial x}\frac{w'}{\lambda+1} + T\frac{\partial}{\partial x}\frac{w'}{\lambda+1} \tag{2.14c}$$

where ρ is the static linear mass density of the cable, Γ is the transverse damping force per unit velocity per unit linear density in the transverse directions and Eq. (2.7) has been used.

2.1.1 Longitudinal Cable Dynamics

Substituting for cable tension from Eq. (2.10) in Eq. (2.14a), we get the following coupled nonlinear longitudinal dynamics of the cable.

$$\begin{aligned}\ddot{u} =& \frac{u''c_w^2 + c_u^2(1+u')\frac{(1+u')u''+v'v''+w'w''}{\lambda+1}}{\lambda+1} + \frac{c_u^2u''\lambda}{\lambda+1} \\ & - \frac{(1+u')((1+u')u''+v'v''+w'w'')(c_w^2+c_u^2\lambda)}{(\lambda+1)^3} \\ =& F(u,v,w,u',v',w',u'',v'',w'')\end{aligned} \tag{2.15}$$

where $c_u^2 = \frac{EA(1+\epsilon_0)}{\rho}$ is the longitudinal wave velocity.

2.1.2 Transverse Cable Dynamics

Substituting Eq. (2.10) in Eq. (2.14b) and Eq. (2.14c), we get the following coupled nonlinear transverse dynamics of the cable.

$$\begin{aligned}\ddot{v} + \Gamma\dot{v} =& \frac{v''c_w^2 + c_u^2v'\frac{(1+u')u''+v'v''+w'w''}{\lambda+1}}{\lambda+1} + \frac{c_u^2v''\lambda}{\lambda+1} \\ & - \frac{v'((1+u')u''+v'v''+w'w'')(c_w^2+c_u^2\lambda)}{(\lambda+1)^3} \\ =& G(u,v,w,u',v',w',u'',v'',w'')\end{aligned} \tag{2.16}$$

$$\begin{aligned}\ddot{w}+\Gamma\dot{w} =& \frac{w''c_w^2+c_u^2w'\frac{(1+u')u''+v'v''+w'w''}{\lambda+1}}{\lambda+1}+\frac{c_u^2w''\lambda}{\lambda+1}\\ &-\frac{w'((1+u')u''+v'v''+w'w'')(c_w^2+c_u^2\lambda)}{(\lambda+1)^3}\\ =& H(u,v,w,u',v',w',u'',v'',w'')\end{aligned} \tag{2.17}$$

where $c_w^2=\frac{EA\epsilon_0}{\rho}$ is the transverse wave velocity. Gravity has been ignored here but will be included in the cable-pulley dynamics.

2.2 Weakly Nonlinear Dynamics

In this section, the exact cable dynamics are simplified to a weakly nonlinear form as proposed by Narasimha [20] where the most significant nonlinearity arises when $u=O(v^2)=O(w^2)$ and all higher order terms are neglected. As a result, the stretched cable segment ds in Eq. (2.6) can be rewritten as,

$$\begin{aligned}ds =& dx(1+2u'+u'^2+v'^2+w'^2)^{\frac{1}{2}}\\ \approx& dx\left(1+u'+\frac{v'^2+w'^2}{2}\right)\end{aligned} \tag{2.18}$$

The apparent strain is hence given by,

$$\lambda=u'+\frac{v'^2+w'^2}{2} \tag{2.19}$$

Substituting for ds from Eq. (2.18) in Eq. (2.2) and using the equilibrium strain equation in Eq. (2.1), the true strain is given by

$$\begin{aligned}\epsilon(x,t) =& \epsilon_0+\frac{dx}{dl}\left(u'+\frac{v'^2+w'^2}{2}\right)\\ =& \epsilon_0+(1+\epsilon_0)\left(u'+\frac{v'^2+w'^2}{2}\right)\end{aligned} \tag{2.20}$$

Assuming cable strain to be small enough to be in the elastic range and ignoring the change in cable cross section due to stretching, cable tension in Eq. (2.10) can be rewritten as follows:

$$\begin{aligned} T(x,t) &= EA\epsilon(x,t) \\ &= T_0 + EA(1+\epsilon_0)\left(u' + \frac{v'^2 + w'^2}{2}\right) \end{aligned} \tag{2.21}$$

As mentioned before, the dynamics of the cable element are given by equating the net force in each direction to the rate of change of momentum,

$$\rho\ddot{u}(x,t) = \frac{\partial T_x}{\partial x} \tag{2.22a}$$

$$\rho\ddot{v}(x,t) = \frac{\partial T_y}{\partial x} - \Gamma\rho\dot{v}(x,t) \tag{2.22b}$$

$$\rho\ddot{w}(x,t) = \frac{\partial T_z}{\partial x} - \Gamma\rho\dot{w}(x,t) \tag{2.22c}$$

Substituting for tension using Eq. (2.13) and Eq. (2.21) in Eq. (2.22), we get the following weakly nonlinear longitudinal and mutually perpendicular transverse cable dynamics.

$$\begin{aligned} \ddot{u} &= c_u^2\lambda'\frac{1+u'}{1+\lambda} + (c_w^2 + c_u^2\lambda)\frac{(1+\lambda)u'' - (1+u')\lambda'}{(1+\lambda)^2} \\ &= F(u,v,w,u',v',w',u'',v'',w'') \end{aligned} \tag{2.23}$$

$$\begin{aligned} \ddot{v} + \Gamma\dot{v} &= c_u^2\lambda'\frac{v'}{1+\lambda} + (c_w^2 + c_u^2\lambda)\frac{(1+\lambda)v'' - v'\lambda'}{(1+\lambda)^2} \\ &= G(u,v,w,u',v',w',u'',v'',w'') \end{aligned} \tag{2.24}$$

$$\begin{aligned} \ddot{w} + \Gamma\dot{w} &= c_u^2\lambda'\frac{w'}{1+\lambda} + (c_w^2 + c_u^2\lambda)\frac{(1+\lambda)w'' - w'\lambda'}{(1+\lambda)^2} \\ &= H(u,v,w,u',v',w',u'',v'',w'') \end{aligned} \tag{2.25}$$

2.3 Cable-Pulley System

Figure 2.2 shows a cable-pulley setup in its equilibrium configuration, consisting of (1) a driving pulley, (2) a load pulley, and (3) a single cable loop under equilibrium tension T_0. The distance between the pulleys is $L_e = L(1+\epsilon_0)$ where L is the

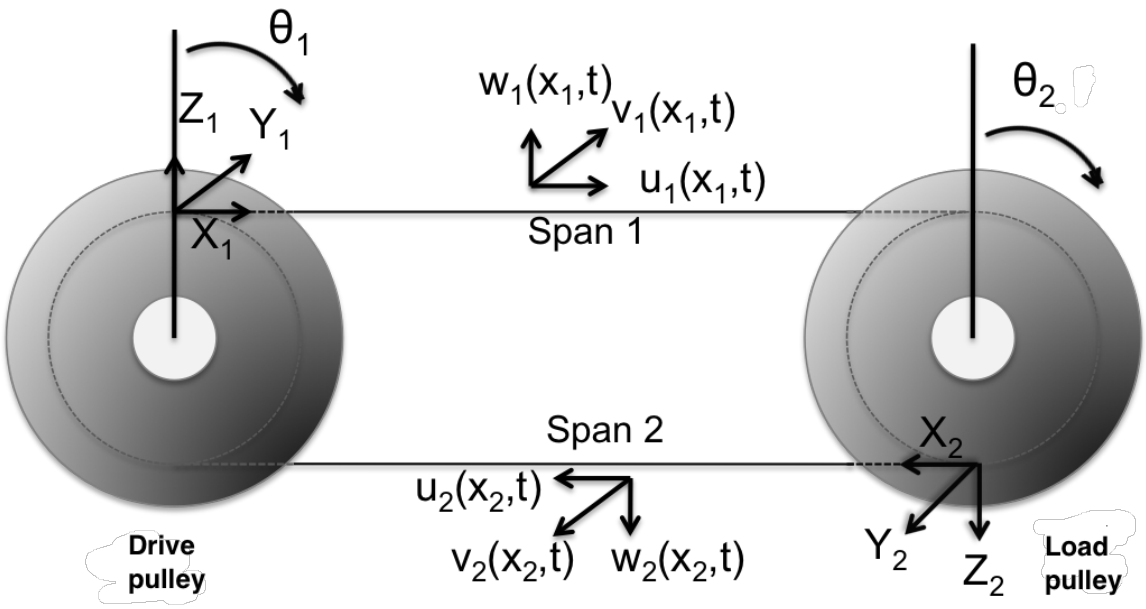

Figure 2.2. Cable-pulley system.

distance between pulleys when the cable is not under tension. Two separate but related coordinate systems have been defined. X_1, Y_1, Z_1 is fixed at the first point of contact between the drive pulley on the left and the upper cable. Similarly, X_2, Y_2, Z_2 is fixed at the first point of contact between the load pulley on the right and the lower cable. At equilibrium, both X_1 and X_2 are along the axial cable directions and gravity acts vertically downwards. Using these coordinate systems, Eqs. (2.15)-(2.17) can be written for the upper and lower cable spans as follows:

$$\begin{aligned} \ddot{u}_1(x_1,t) &= F_1 \\ \ddot{v}_1(x_1,t) + \Gamma\dot{v}_1(x_1,t) &= G_1 \\ \ddot{w}_1(x_1,t) + \Gamma\dot{w}_1(x_1,t) &= H_1 - g \end{aligned} \tag{2.26}$$

and

$$\begin{aligned} \ddot{u}_2(x_2,t) &= F_2 \\ \ddot{v}_2(x_2,t) + \Gamma\dot{v}_2(x_2,t) &= G_2 \\ \ddot{w}_2(x_2,t) + \Gamma\dot{w}_2(x_2,t) &= H_2 + g \end{aligned} \tag{2.27}$$

2.4 Pulley Dynamics

The pulley dynamics is coupled with the cable vibrations at the boundaries through cable tension, which is a function of cable strain. Assuming that friction between the cable loop and pulleys is large enough to prevent slipping, the free motion of the pulleys in the absence of external torque is governed by,

$$J_1\ddot{\theta}_1 + b_1\dot{\theta}_1 + c_1 S(\dot{\theta}_1) = \big(T_1(0,t) - T_2(L_e,t)\big)r_1 \tag{2.28a}$$

$$J_2\ddot{\theta}_2 + b_2\dot{\theta}_2 + c_2 S(\dot{\theta}_2) = \big(T_2(0,t) - T_1(L_e,t)\big)r_2 \tag{2.28b}$$

where J_1, J_2 are the rotational moments of inertia of the drive and load pulleys respectively. θ_1, θ_2 are their corresponding angular rotations. r_1, r_2 are their radii. b_1, b_2 are the damping coefficients and c_1, c_2 are coulomb friction coefficients of the drive and load pulleys respectively. $S(\bullet)$ represents the usual signum function.

2.5 Boundary Conditions

Since the cable ends are attached to the pulleys, their displacements are constrained by the rotation of the pulleys. Friction between the cable and pulleys is assumed sufficient to prevent cable slip, leading to the following boundary conditions.

$$\begin{aligned} u_1(0,t) &= u_2(L_e,t) = r_1\theta_1(t) \\ u_1(L_e,t) &= u_2(0,t) = r_2\theta_2(t) \end{aligned} \tag{2.29}$$

In the transverse directions, the boundary conditions are essentially the same as for a cable fixed to rigid supports on both ends to prevent displacement only.

$$\begin{aligned} v_1(0,t) = v_1(L_e,t) = v_2(0,t) = v_2(L_e,t) = 0 \\ w_1(0,t) = w_1(L_e,t) = w_2(0,t) = w_2(L_e,t) = 0 \end{aligned} \tag{2.30}$$

2.6 Finite Difference Scheme

Traditionally, linear second-order wave equations have been discretized either using explicit central difference time-marching schemes or implicit backward difference schemes. Since implicit schemes are generally computationally more intensive, to reduce the computational burden, an explicit central difference scheme has been used to discretize the nonlinear cable dynamics in Eqs. (2.26) and (2.27). Based on the chosen configuration of the system, physical parameters such as $E, A, L, \rho, r_1, r_2, T_0$ are assumed to be known. Dividing each of the two cable spans into n equal segments of length $dx = \frac{L_e}{n-1}$ as shown in Figure 2.3, the numerical time step is obtained as follows:

$$\begin{aligned} c_u &= \sqrt{\frac{EA}{\rho}} \\ dt &= \sigma \frac{dx}{c_u} \end{aligned} \tag{2.31}$$

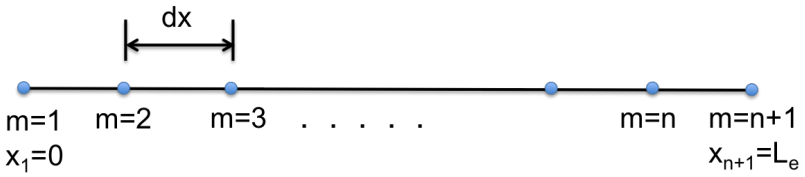

Figure 2.3. Cable span divided into n equal segments.

where σ is the Courant-Friedrichs-Lewy (CFL) number. The condition $\sigma < 1$ must be satisfied for stability of the explicit numerical scheme [80]. The discretized cable dynamics for $i = 1, 2$ are as follows:

$$\frac{u_i(t_{j+1}, x_m) - 2u_i(t_j, x_m) + u_i(t_{j-1}, x_m)}{dt^2} = F_i|_{(t_j, x_m)} \tag{2.32a}$$

$$\frac{v_i(t_{j+1}, x_m) - 2v_i(t_j, x_m) + v_i(t_{j-1}, x_m)}{dt^2} + \Gamma \frac{v_i(t_{j+1}, x_m) - v_i(t_{j-1}, x_m)}{2dt} = G_i|_{(t_j, x_m)} \tag{2.32b}$$

$$\frac{w_1(t_{j+1}, x_m) - 2w_i(t_j, x_m) + w_i(t_{j-1}, x_m)}{dt^2} + \Gamma \frac{w_i(t_{j+1}, x_m) - w_i(t_{j-1}, x_m)}{2dt} = H_i|_{(t_j, x_m)} \pm g \tag{2.32c}$$

Eq. (2.32) can be used to calculate $u_i, v_i, w_i,\ i = 1, 2$ at every successive time step given by t_{j+1}. The nonlinear functions F_i, G_i, H_i evaluated at (t_j, x_m) are functions of $u_i', v_i', w_i', u_i'', v_i'', w_i''$ evaluated at (t_j, x_m) . These spatial derivatives, for $i = 1, 2$, are calculated using central differences as follows:

$$u_i'|_{(t_j, x_m)} = \frac{u_i(t_j, x_{m+1}) - u_i(t_j, x_{m-1})}{2dx} \tag{2.33a}$$

$$v_i'|_{(t_j, x_m)} = \frac{v_i(t_j, x_{m+1}) - v_i(t_j, x_{m-1})}{2dx} \tag{2.33b}$$

$$w_i'|_{(t_j, x_m)} = \frac{w_i(t_j, x_{m+1}) - w_i(t_j, x_{m-1})}{2dx} \tag{2.33c}$$

and

$$u_i''|_{(t_j, x_m)} = \frac{u_i(t_j, x_{m+1}) - 2u_i(t_j, x_m) + u_i(t_j, x_{m-1})}{2dx} \tag{2.34a}$$

$$v_i''|_{(t_j, x_m)} = \frac{v_i(t_j, x_{m+1}) - 2v_i(t_j, x_m) + v_i(t_j, x_{m-1})}{2dx} \tag{2.34b}$$

$$w_i''|_{(t_j, x_m)} = \frac{w_i(t_j, x_{m+1}) - 2w_i(t_j, x_m) + w_i(t_j, x_{m-1})}{2dx} \tag{2.34c}$$

The boundary conditions in Eqs. (2.29) and (2.30) are applied at $m = 1, n+1$. Hence at any given time t_j, the following conditions are enforced:

$$u_1(t_j, x_1 = 0) = u_2(t_j, x_{n+1} = L_e) = r_1\theta_1(t_j) \tag{2.35a}$$

$$u_1(t_j, x_{n+1} = L_e) = u_2(t_j, x_1 = 0) = r_2\theta_2(t_j) \tag{2.35b}$$

For $i = 1, 2$,

$$v_i(t_j, x_1 = 0) = v_i(t_j, x_{n+1} = L_e) = 0 \tag{2.36a}$$

$$w_i(t_j, x_1 = 0) = w_i(t_j, x_{n+1} = L_e) = 0 \tag{2.36b}$$

The pulley dynamics in Eq. (2.28) are discretized as follows:

$$J_1 \frac{\theta_1(t_{j+1}) - 2\theta_1(t_j) + \theta_1(t_{j-1})}{dt^2} + b_1 \frac{\theta_1(t_{j+1}) - \theta_1(t_{j-1})}{2dt} = K_1(t_j) \tag{2.37a}$$

$$J_2 \frac{\theta_2(t_{j+1}) - 2\theta_2(t_j) + \theta_2(t_{j-1})}{dt^2} + b_2 \frac{\theta_2(t_{j+1}) - \theta_2(t_{j-1})}{2dt} = K_2(t_j) \tag{2.37b}$$

where coulomb friction is ignored for convenience. $\theta_1(t_{j+1}), \theta_2(t_{j+1})$ are obtained from Eq. (2.37) and applied to the numerical boundary conditions in Eq. (2.35) at the appropriate time step. $K_1(t_j), K_2(t_j)$ are calculated as follows:

$$K_1(t_j) = EA(1+\epsilon_0) r_1 \left(\sqrt{(1+u_1')^2 + {v_1'}^2 + {w_1'}^2} \Big|_{(t_j,0)} - \sqrt{(1+u_2')^2 + {v_2'}^2 + {w_2'}^2} \Big|_{(t_j,L_e)} \right) \tag{2.38a}$$

$$K_2(t_j) = EA(1+\epsilon_0) r_2 \left(\sqrt{(1+u_2')^2 + {v_2'}^2 + {w_2'}^2} \Big|_{(t_j,0)} - \sqrt{(1+u_1')^2 + {v_1'}^2 + {w_1'}^2} \Big|_{(t_j,L_e)} \right) \tag{2.38b}$$

Since $\theta(t_{j+1})$ depends on $\theta(t_j)$ and $\theta(t_{j-1})$, the pulley angles at the first two time instants need to be known. $\theta_1(0), \theta_2(0), \dot{\theta}_1(0), \dot{\theta}_2(0)$ are obtained from the initial conditions of the system. $\theta_1(dt)$ and $\theta_2(dt)$ can be calculated as follows:

$$\begin{aligned} \theta_1(dt) &= \theta_1(0) + dt\dot{\theta}_1(0) + \frac{dt^2}{2}\ddot{\theta}_1(0) + O(dt^3) \\ &\approx dt\dot{\theta}_1(0) + \frac{dt^2}{2J_1}(K_1(0) - b_1\dot{\theta}_1(0)) \end{aligned} \tag{2.39a}$$

$$\theta_2(dt) \approx \theta_2(0) + dt\dot{\theta}_2(0) + \frac{dt^2}{2J_2}(K_2(0) - b_2\dot{\theta}_2(0)) \tag{2.39b}$$

The values of $u_i, v_i, w_i,\ i = 1, 2$ at $t = 0, dt$ can be calculated similarly. Hence the discretized form in Eqs. (2.32)-(2.39) can be simulated with the relevant initial conditions of the cable spans and pulleys.

3. MODAL ANALYSIS

The effect of cable elasticity on the vibration modes of cable-driven robotic systems has been largely neglected. Joint flexibility has been modeled in many studies of cable-actuated robot manipulators [40], [41], [42], [43] while the cables are assumed to be rigid. Zeinali and Khajepour [40] designed an adaptive sliding mode controller for a parallel cable-driven manipulator using only rigid body dynamics of the system. Flexible modes resulting from the cable were considered to be high-frequency dynamics modeled as a bounded lumped uncertainty for stability purposes. Trevisani et al. [41] proposed a hybrid serial/parallel architecture for a planar translational cable-driven robot with two redundant actuators to ensure positive cable tension. The end effector was controlled using four cable-actuators while also being supported by a passive two-degree-of-freedom serial manipulator that provided stiffness normal to the plane of motion. Korayem et al. [42] calculated the dynamic load carrying capacity of a cable-driven robot for both rigid and flexible joints. Impedance control of a multi-stage cable-pulley-driven robot with flexible joints and rigid cables was considered by Pitakwatchara [43]. The effect of cable tension on stiffness and stability of cable manipulators was studied by Behzadipour [44]. In more recent numerical studies by Diao and Ma [45], it was shown that the modeling of cables as axial springs can help accurately predict natural frequencies of a 6-DOF cable manipulator, though the results were not experimentally verified. It was concluded that in space robotic applications, the fundamental frequency of the manipulator due to cable flexibility was still much higher than those attributed to joint or link vibration modes. It was also shown that transverse vibrations of the cables can be ignored compared to the axial modes simply by increasing cable tension, since the effect of cable tension on axial modes is not significant in the linear elastic range. These studies also indicate that in cable-driven robot manipulators used in high-bandwidth applications where

the fundamental frequency due to cable elasticity is sufficiently low, it is important to consider cable stiffness in the dynamic model of the system, since it affects overall stiffness of the manipulator.

The cable-pulley setup in Figure 2.2 is a prototypical system that can be used to understand the effect of cable flexibility on the performance of various high-speed, motion control applications. Since the goal is precise motion tracking and cable-driven motion is only possible through tensile cable forces, the system studied is such that the cables are always in tension during operation. The load pulley angle is controlled using an external torque acting from the drive pulley, while tension in the cables is used to transmit forces. Due to their inherent flexibility, cable vibrations can lead to performance issues during motion transmission. It is hence necessary to calculate the overall system's natural vibration modes resulting from cable elasticity. This helps model the system more accurately by including its lower-frequency modes while neglecting only the high-frequency modes based on available controller bandwidth.

3.1 Linear Cable Dynamics

To determine the longitudinal vibration modes of the system, a modal analysis is performed using the linear equations of motion. As mentioned earlier, classical linear analyses of the vibrating string require simplifying assumptions such as small displacements and slopes, small changes in tension compared to the equilibrium value etc. and can be summarized as follows:

$$u', v', w' << 1 \tag{3.1a}$$

$$u'^2, v'^2, w'^2 << u' \tag{3.1b}$$

Under the assumptions in Eq. (3.1), the stretched cable segment length ds is given by,

$$\begin{aligned} ds &= \left(\sqrt{(1+u')^2 + v'^2 + w'^2}\right)dx \\ &= \left(\sqrt{1 + 2u' + u'^2 + v'^2 + w'^2}\right)dx \\ &\approx (\sqrt{1+2u'})dx \\ &\approx (1+u')dx \end{aligned} \tag{3.2}$$

Hence the true strain and net tension at a point in the cable can be simplified from Eqs. (2.9) and (2.10),

$$\epsilon(x,t) = \epsilon_0 + (1+\epsilon_0)u' \tag{3.3}$$

$$T(x,t) = T_0 + EA(1+\epsilon_0)u' \tag{3.4}$$

The tension components are given by,

$$T_x = T(1+u')\frac{dx}{ds} = T \tag{3.5a}$$

$$T_y = Tv'\frac{dx}{ds} = \frac{Tv'}{1+u'} \approx Tv' \tag{3.5b}$$

$$T_z = Tw'\frac{dx}{ds} = \frac{Tw'}{1+u'} \approx Tw' \tag{3.5c}$$

The dynamics of the cable segment can be rewritten as follows:

$$\rho\ddot{u}(x,t) = \frac{\partial T_x}{\partial x} = \frac{\partial T}{\partial x} \tag{3.6a}$$

$$\rho\ddot{v}(x,t) = \frac{\partial T_y}{\partial x} = \frac{\partial T}{\partial x}v' + Tv'' \tag{3.6b}$$

$$\rho\ddot{w}(x,t) = \frac{\partial T_z}{\partial x} = \frac{\partial T}{\partial x}w' + Tw'' \tag{3.6c}$$

Further simplifying Eq. (3.6) and neglecting all higher order terms, the linear dynamic equations of motion for the cable spans in Figure 2.2 can be decoupled as follows:

$$\ddot{u}_1(x_1,t) = c_u^2 u_1''(x_1,t) \tag{3.7a}$$

Upper Span:

$$\ddot{v}_1(x_1,t) = c_w^2 v_1''(x_1,t) \tag{3.7b}$$

$$\ddot{w}_1(x_1,t) = c_w^2 w_1''(x_1,t) - g \tag{3.7c}$$

and

$$\ddot{u}_2(x_2,t) = c_u^2 u_2''(x_2,t) \tag{3.8a}$$

Lower Span:
$$\ddot{v}_2(x_2,t) = c_w^2 v_2''(x_2,t) \tag{3.8b}$$

$$\ddot{w}_2(x_2,t) = c_w^2 w_2''(x_2,t) + g \tag{3.8c}$$

Ignoring damping and friction in the pulleys for simplicity without losing model fidelity, the dynamic longitudinal boundary conditions of the cables are as follows:

$$\frac{J_1}{r_1}\ddot{\theta}_1(t) = \frac{J_1}{r_1^2}\ddot{u}_1(0,t) = T_1(0,t) - T_2(L_e,t) = EA(1+\epsilon_0)(u_1'(0,t) - u_2'(L_e,t)) \tag{3.9a}$$

$$\frac{J_2}{r_2}\ddot{\theta}_2(t) = \frac{J_2}{r_2^2}\ddot{u}_2(0,t) = T_2(0,t) - T_1(L_e,t) = EA(1+\epsilon_0)(u_2'(0,t) - u_1'(L_e,t)) \tag{3.9b}$$

$$u_1(0,t) = u_2(L_e,t) \tag{3.9c}$$

$$u_2(0,t) = u_1(L_e,t) \tag{3.9d}$$

3.2 Cable-Pulley System

The upper and lower cable span displacements $u_1(x_1,t)$ and $u_2(x_2,t)$ are separated into spatial and temporal functions as follows:

$$\begin{pmatrix} u_1(x_1,t) \\ u_2(x_2,t) \end{pmatrix} = \begin{pmatrix} U_1(x_1) \\ U_2(x_2) \end{pmatrix} e^{i\omega t} \tag{3.10}$$

where $\frac{\omega}{2\pi}$ represents all the natural longitudinal frequencies of the cable-pulley system and $U_i(x_i),\ i = 1,2$ represent the corresponding cable mode shapes. We obtain the following spatial functions by substituting Eq. (3.10) in Eqs. (3.7a) and (3.8a),

$$U_1(x_1) = a_1 \cos(\frac{\omega x_1}{c_u}) + b_1 \sin(\frac{\omega x_1}{c_u}) \tag{3.11a}$$

$$U_2(x_2) = a_2 \cos(\frac{\omega x_2}{c_u}) + b_2 \sin(\frac{\omega x_2}{c_u}) \tag{3.11b}$$

where a_i, b_i are unknown constant coefficients. Substituting the above spatial functions and Eq. (3.10) in boundary conditions Eq. (3.9), we obtain

$$\frac{J_1}{r_1^2}a_1(-\omega^2) = EA(1+\epsilon_0)\frac{\omega}{c_u}\left(b_1 + a_2\sin(\frac{\omega L_e}{c_u}) - b_2\cos(\frac{\omega L_e}{c_u})\right) \tag{3.12a}$$

$$\frac{J_2}{r_2^2}a_2(-\omega^2) = EA(1+\epsilon_0)\frac{\omega}{c_u}\left(b_2 + a_1\sin(\frac{\omega L_e}{c_u}) - b_1\cos(\frac{\omega L_e}{c_u})\right) \tag{3.12b}$$

$$a_1 = a_2\cos(\frac{\omega L_e}{c_u}) + b_2\sin(\frac{\omega L_e}{c_u}) \tag{3.12c}$$

$$a_2 = a_1\cos(\frac{\omega L_e}{c_u}) + b_1\sin(\frac{\omega L_e}{c_u}) \tag{3.12d}$$

With further simplification, Eqs. (3.12a)-(3.12d) can be rewritten in matrix form as follows:

$$\begin{pmatrix} \frac{J_1\omega}{c_u\rho r_1^2} & \sin(\frac{\omega L_e}{c_u}) & 1 & -\cos(\frac{\omega L_e}{c_u}) \\ \sin(\frac{\omega L_e}{c_u}) & \frac{J_2\omega}{c_u\rho r_2^2} & -\cos(\frac{\omega L_e}{c_u}) & 1 \\ 1 & -\cos(\frac{\omega L_e}{c_u}) & 0 & -\sin(\frac{\omega L_e}{c_u}) \\ -\cos(\frac{\omega L_e}{c_u}) & 1 & -\sin(\frac{\omega L_e}{c_u}) & 0 \end{pmatrix} . \begin{pmatrix} a_1 \\ a_2 \\ b_1 \\ b_2 \end{pmatrix} = 0 \tag{3.13}$$

The natural frequencies of the cable-pulley system are obtained by solving Eq. (3.13). For a non-trivial solution to exist, the modal matrix above must be singular. Equating the determinant to zero leads to an implicit characteristic equation in the system's natural frequency $\omega_n, n = 0, 1, 2...$, which has infinitely many solutions. The equation is easy to solve numerically using Matlab's $fzero$ function which uses a combination of bisection, secant and inverse quadratic interpolation methods to find the root of a function. Table 3.1 lists the physical parameters of the cable-pulley system for two different configurations; one where the drive motor is detached from the drive pulley and one where it is connected as reflected in the parameter J_1. Figures 3.1(a) and 3.2(a) show the determinant of the above modal matrix as a function of frequency. The zero-crossings indicate the theoretical natural frequencies of the system.

Figures 3.1(b) and 3.2(b) show the determinant of the modal matrix zoomed at lower frequencies so that the fundamental longitudinal frequency can be seen more clearly. The natural frequencies of both configurations are shown in Table 3.2. It can

Table 3.1. Physical parameters of cable-pulley system.

	Configuration 1	Configuration 2
Cable material	nylon	nylon
J_1	$7.316 \times 10^{-6}\ kgm^2$	$0.0011\ kgm^2$
J_2	$7.316 \times 10^{-6}\ kgm^2$	$7.316 \times 10^{-6}\ kgm^2$
r_1	$3\ cm$	$3\ cm$
r_2	$3\ cm$	$3\ cm$
E	$2.6\ Gpa$	$2.6\ Gpa$
A	$4.26 \times 10^{-7}\ m^2$	$4.26 \times 10^{-7}\ m^2$
ρ	$4.9 \times 10^{-4}\ kg/m$	$4.9 \times 10^{-4}\ kg/m$
L	$1\ m$	$1\ m$
T_0	$5\ N$	$5\ N$

be seen that there is a large gap between the first two natural longitudinal frequencies of the system.

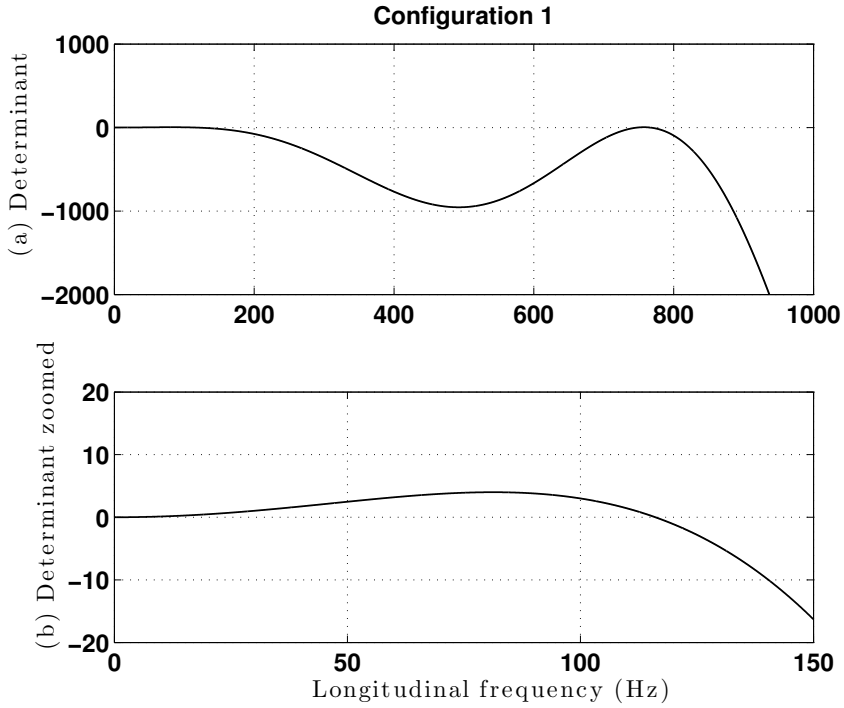

Figure 3.1. Determinant of modal matrix for Configuration 1.

Table 3.2. Modal frequencies of cable-pulley system.

	Fundamental Longitudinal Frequency	Second Longitudinal Frequency	Fundamental Transverse Frequency	Fundamental Longitudinal Frequency with rigid end-supports
Configuration 1	116Hz	766Hz	50.5Hz	751.8Hz
Configuration 2	81.6Hz	757.5Hz	50.5Hz	751.8Hz

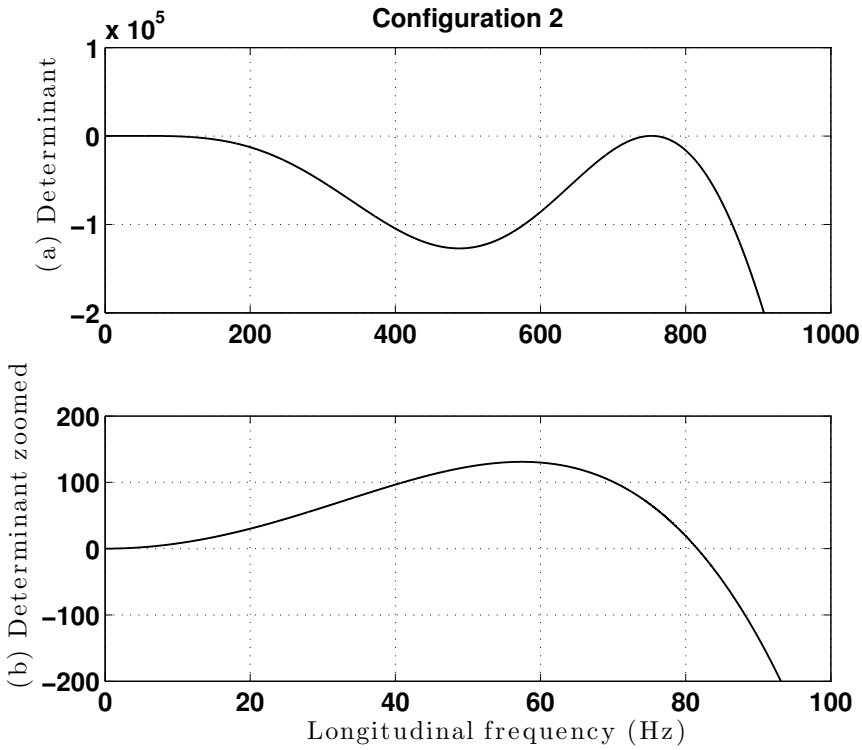

Figure 3.2. Determinant of modal matrix for Configuration 2.

Figures 3.3 and 3.4 show the normalized fundamental longitudinal mode shapes of the cable spans obtained from the null space of the modal matrix in Eq. (3.13), evaluated at the fundamental natural frequency. They are consistent with a spring-like behavior of the two cable spans. Figure 3.5(a) and (b) illustrate the possible fundamental longitudinal modes of the two cable spans in the cable-pulley system. The out-of-phase cable oscillations in Figure 3.5(a) require angular rotation of the pulleys and are consistent with the cable modes in Figures 3.3 and 3.4. They are also consistent with the drastic reduction in fundamental frequency of the cables when compared to a similar arrangement where the boundary conditions are rigid supports instead of pulleys. In contrast, the in-phase cable oscillations in Figure 3.5(b) do not require angular acceleration of the pulleys.

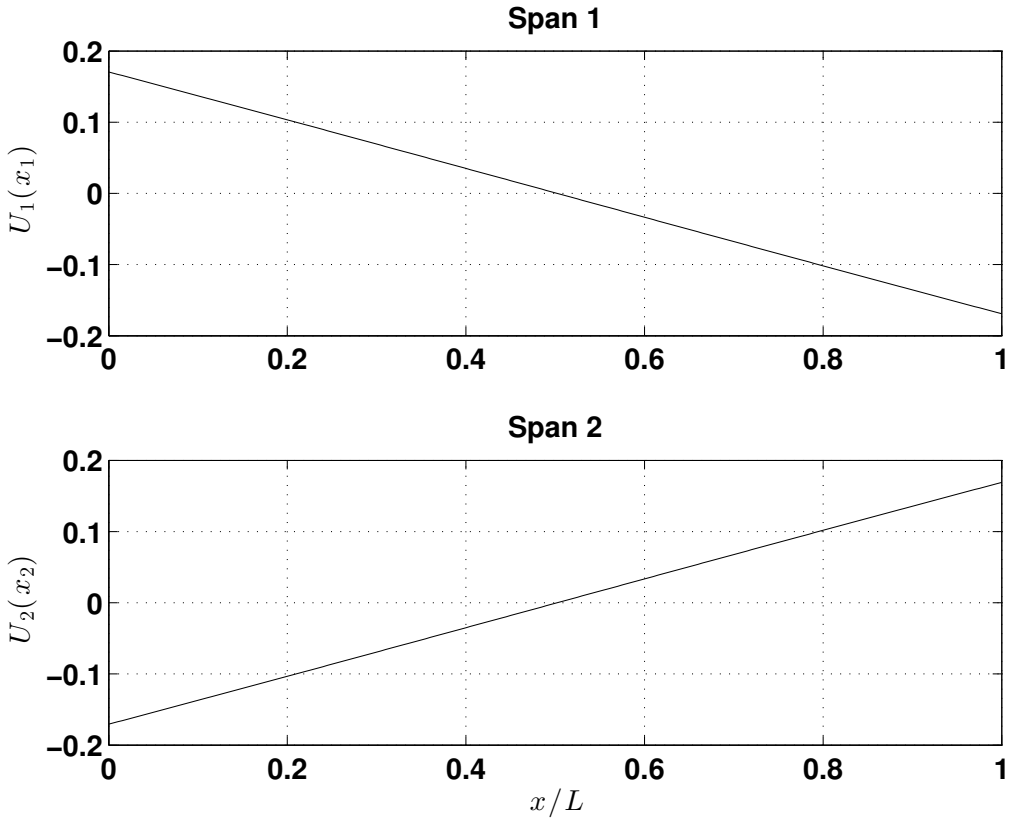

Figure 3.3. Fundamental longitudinal mode shapes of upper and lower cable spans for Configuration 1.

3.2.1 Comparison to Rigid Boundary Conditions

Consider a flexible cable fixed between two rigid supports. The fundamental longitudinal and transverse vibration frequencies are given by,

$$f_{long} = \frac{c_u}{2L} \tag{3.14a}$$

$$f_{transverse} = \frac{c_w}{2L} \tag{3.14b}$$

where $c_u^2 = \frac{EA(1+\epsilon_0)}{\rho}$ and $c_w^2 = \frac{T_0}{\rho}$ are the longitudinal and transverse wave velocities respectively, T_0 is the equilibrium tension, ϵ_0 is the strain due to equilibrium tension and L is cable length between the fixed supports. Using the same parameter values in

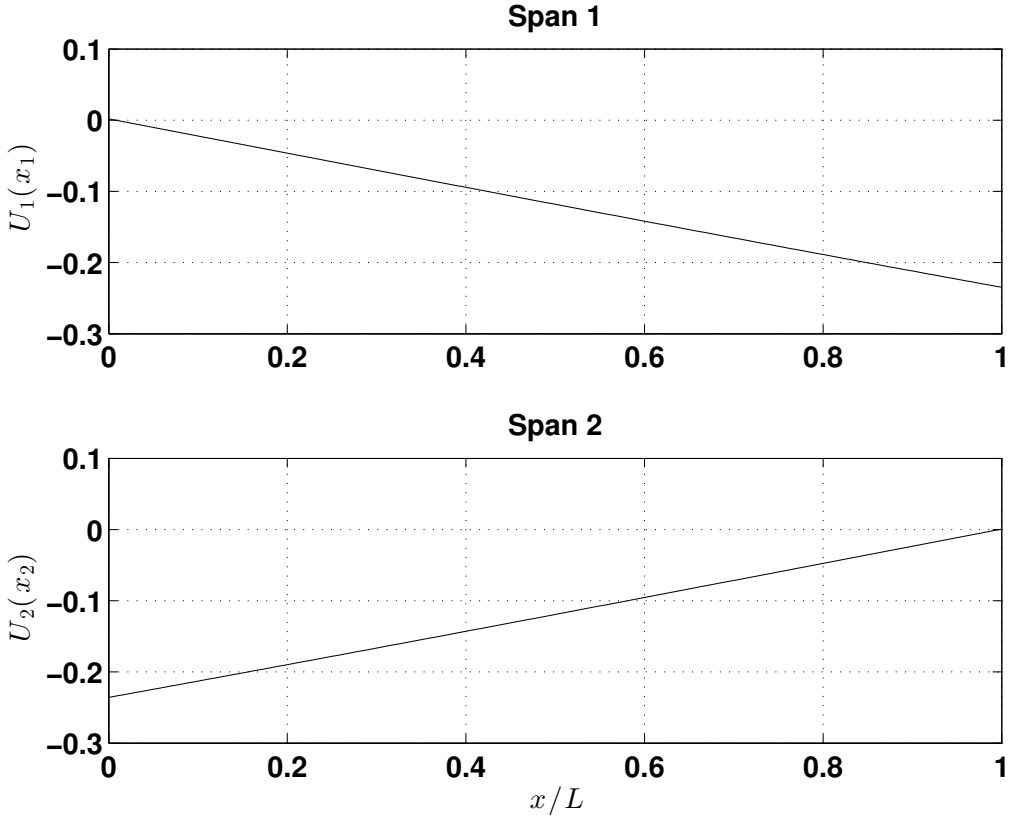

Figure 3.4. Fundamental longitudinal mode shapes of upper and lower cable spans for Configuration 2.

Table 3.1, the fundamental longitudinal frequency of a cable with fixed rigid supports instead of pulleys are calculated using Eq. (3.14a) and shown in Table 3.2. Compared to the cable with rigid end-supports, the cable-pulley system has a much lower fundamental longitudinal frequency. The corresponding fundamental transverse frequency of the cable with rigid end-supports is also calculated using Eq. (3.14b) and shown in Table 3.2. It is worth noting that at lower values of tension (T_0), the fundamental transverse frequency is much lower then the fundamental longitudinal frequency. For this reason, longitudinal cable vibrations are usually ignored or decoupled from trans-

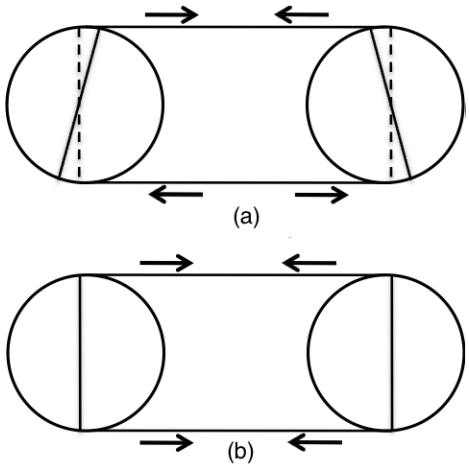

Figure 3.5. Fundamental longitudinal modes (a) out of phase; (b) in-phase.

verse vibrations in most dynamic analyses as well as vibration control applications. The same does not apply in the case of the cable-pulley system.

3.2.2 Experimental Results

A detailed description of the experimental setup can be found in Chapter 4. Both cable spans of the cable-pulley system in configuration 2 shown in Table 3.1 were plucked at their midpoints and load pulley oscillations were recorded using an optical encoder. Figure 3.6 shows the frequency spectrum of the recorded free oscillations of the load pulley. The peak matches closely with the theoretical frequency of 81.6Hz in Table 3.2, validating the analysis so far. In the following section, the modal analysis of the cable-pulley system is extended to cable-transporter systems so that the effect of the transported mass on the vibration modes of the system can be studied in a similar way.

3.3 Cable Transporter System

There have been many studies on suspended cable-mass systems that use long, flexible, lightweight cables in an effort to analyze engineering applications such as

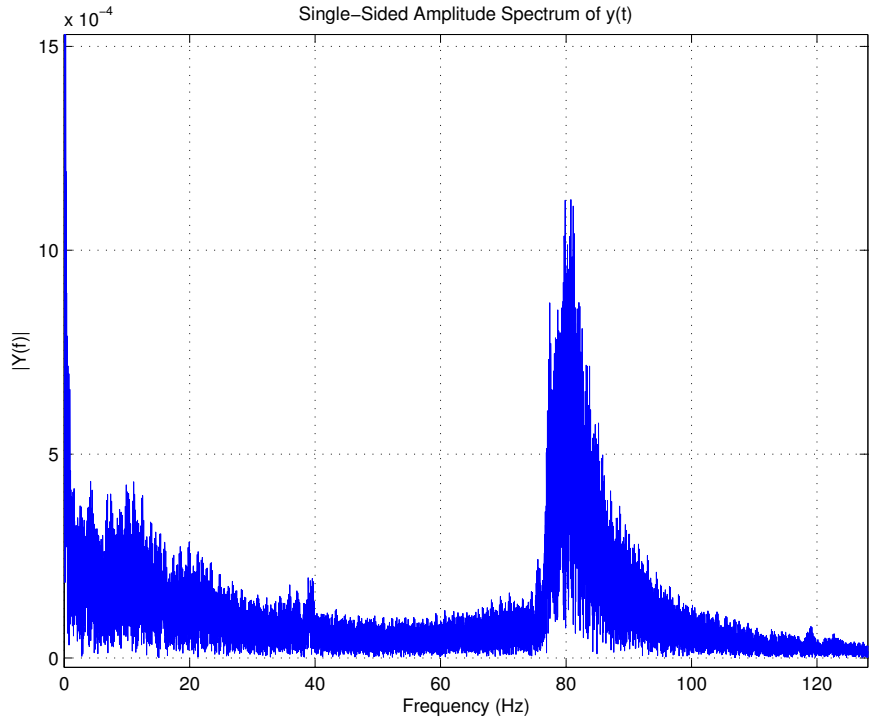

Figure 3.6. Frequency spectrum of cable-pulley system's free oscillations from Configuration 2.

aerial cableways, tramways and cranes. Sergev [48] presented an iterative algorithm to calculate transverse mode shapes and frequencies of a taut cable with attached discrete masses at extremely high mode numbers. Longitudinal modes were not studied but reasonable experimental agreement was found for the first 8-10 transverse modes. Wu and Chen [49] investigated the dynamic behavior of an inextensible stationary cable suspended between two points of equal elevation, under a moving load. The transient dynamics of such a cable-mass system was studied later by Wang [53] under conditions such as a free fall of the mass onto the cable and rapid acceleration or braking, A linearized theoretical model for calculating low and higher order eigensolutions in the transverse direction for an arbitrarily complex array of discrete masses, attached to a suspended sagged cable fixed between two supports was developed by Lin and Perkins [50]. Brownjohn [51] simulated the vertical plane vibrations of a cable

car and compared them with recorded vibrations during emergency halts and when the car passed over support towers. Renezeder et al. [54] analyzed the fundamental transverse modes of a 'rope field' in a monocable ropeway supported between two towers as a function of rope speed. Sofi and Muscolino [55] numerically studied the in-plane vibrations of a cable with small sag-to-span ratio, carrying an array of moving oscillators. The cable was fixed at both ends while the oscillators were allowed to move at arbitrary velocities. Under the small sag-to-span assumption, longitudinal inertial forces were neglected leading to a governing equation in the vertical displacement alone. Hoffmann [56] experimentally studied the effect of cross winds on the oscillation of gondolas such as chairlifts and ropeways. The effect of transported mass on the natural longitudinal frequency of the system has been less studied in literature.

3.3.1 Single Mass with Cable Loop

The schematic of a cable-transporter system with a single mass moved using a cable loop is shown in Figure 3.7. This is a common setup used in elevators and some monocable gondolas. L_1, L_2 are stretched cable lengths as shown in the figure such that $L_1 + L_2 = L_e$ where L_e is the distance between the two pulleys at equilibrium. The following are the linear equations of motion.

$$\ddot{u}_1(x_1, t) = c_u^2 u_1''(x_1, t) \tag{3.15a}$$

$$\ddot{u}_2(x_2, t) = c_u^2 u_2''(x_2, t) \tag{3.15b}$$

$$\ddot{u}_3(x_3, t) = c_u^2 u_3''(x_3, t) \tag{3.15c}$$

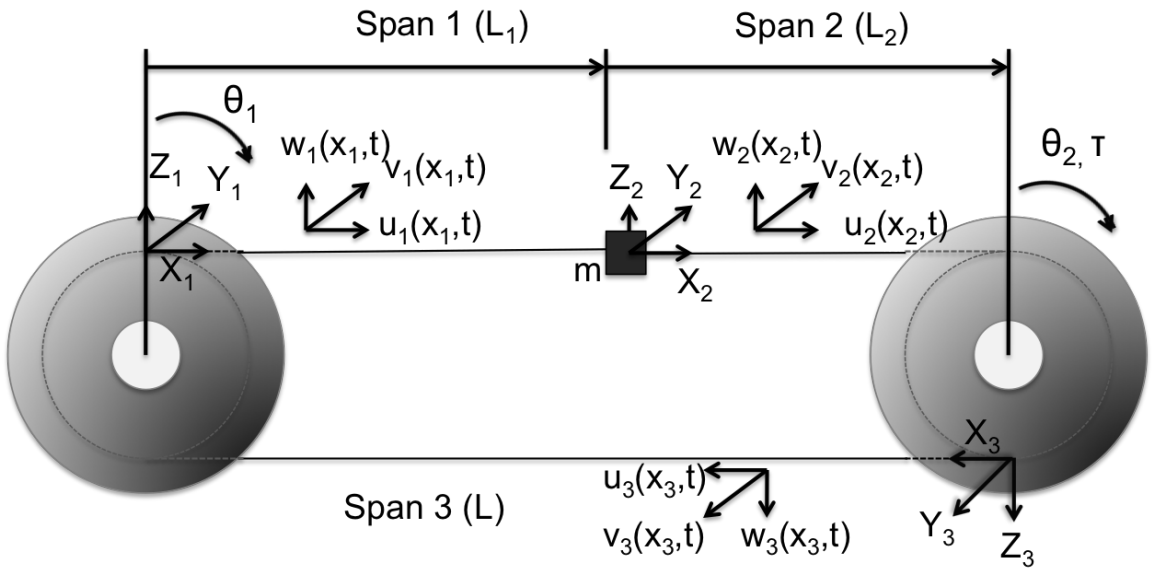

Figure 3.7. Cable transporter system with cable loop.

The dynamic boundary equations and constraints are as follows:

$$m\ddot{u}_2(0,t) = EA(u_2'(0,t) - u_1'(L_1,t)) \tag{3.16a}$$

$$\frac{J_1}{r_1}\ddot{\theta}_1(t) = \frac{J_1}{r_1^2}\ddot{u}_1(0,t) = EA(u_1'(0,t) - u_3'(L_e,t)) \tag{3.16b}$$

$$\frac{J_2}{r_2}\ddot{\theta}_2(t) = \frac{J_2}{r_2^2}\ddot{u}_3(0,t) = EA(u_3'(0,t) - u_2'(L_2,t)) \tag{3.16c}$$

$$u_1(0,t) = u_3(L_e,t) \tag{3.16d}$$

$$u_3(0,t) = u_2(L_2,t) \tag{3.16e}$$

$$u_2(0,t) = u_1(L_1,t) \tag{3.16f}$$

Separating the longitudinal cable displacements into spatial and temporal functions as shown,

$$\begin{pmatrix} u_1(x_1,t) \\ u_2(x_2,t) \\ u_3(x_3,t) \end{pmatrix} = \begin{pmatrix} U_1(x_1) \\ U_2(x_2) \\ U_3(x_3) \end{pmatrix} e^{i\omega t} \tag{3.17}$$

where $\frac{\omega}{2\pi}$ represents all the natural longitudinal frequencies of the system and $U_i(x_i)$ for $i = 1, 2, 3$ represent the mode shapes, we obtain the following spatial functions from substituting Eq. (3.17) in Eq. (3.15),

$$U_1(x_1) = a_1 \cos(\frac{\omega x_1}{c_u}) + b_1 \sin(\frac{\omega x_1}{c_u}) \tag{3.18a}$$

$$U_2(x_2) = a_2 \cos(\frac{\omega x_2}{c_u}) + b_2 \sin(\frac{\omega x_2}{c_u}) \tag{3.18b}$$

$$U_3(x_3) = a_3 \cos(\frac{\omega x_3}{c_u}) + b_3 \sin(\frac{\omega x_3}{c_u}) \tag{3.18c}$$

where a_i, b_i are unknown constant coefficients. Substituting the above spatial functions and Eq. (3.17) in boundary conditions Eq. (3.16), we obtain

$$ma_2(-\omega^2) = EA\frac{\omega}{c_u}\left(b_2 + a_1 \sin(\frac{\omega L_1}{c_u}) - b_1 \cos(\frac{\omega L_1}{c_u})\right) \tag{3.19a}$$

$$\frac{J_1}{r_1^2}a_1(-\omega^2) = EA\frac{\omega}{c_u}\left(b_1 + a_3 \sin(\frac{\omega L_e}{c_u}) - b_3 \cos(\frac{\omega L_e}{c_u})\right) \tag{3.19b}$$

$$\frac{J_2}{r_2^2}a_3(-\omega^2) = EA\frac{\omega}{c_u}\left(b_3 + a_2 \sin(\frac{\omega L_2}{c_u}) - b_2 \cos(\frac{\omega L_2}{c_u})\right) \tag{3.19c}$$

$$a_1 = a_3 \cos(\frac{\omega L_e}{c_u}) + b_3 \sin(\frac{\omega L_e}{c_u}) \tag{3.19d}$$

$$a_3 = a_2 \cos(\frac{\omega L_2}{c_u}) + b_2 \sin(\frac{\omega L_2}{c_u}) \tag{3.19e}$$

$$a_2 = a_1 \cos(\frac{\omega L_1}{c_u}) + b_1 \sin(\frac{\omega L_1}{c_u}) \tag{3.19f}$$

With further simplification, Eqs. (3.19a)-(3.19f) can be re-written in matrix form as follows:

$$\begin{pmatrix} \sin(\frac{\omega L_1}{c_u}) & \frac{m\omega}{c_u\rho} & 0 & -\cos(\frac{\omega L_1}{c_u}) & 1 & 0 \\ \frac{J_1\omega}{c_u\rho r_1^2} & 0 & \sin(\frac{\omega L_e}{c_u}) & 1 & 0 & -\cos(\frac{\omega L_e}{c_u}) \\ 0 & \sin(\frac{\omega L_2}{c_u}) & \frac{J_2\omega}{c_u\rho r_2^2} & 0 & -\cos(\frac{\omega L_2}{c_u}) & 1 \\ 1 & 0 & -\cos(\frac{\omega L_e}{c_u}) & 0 & 0 & -\sin(\frac{\omega L_e}{c_u}) \\ 0 & -\cos(\frac{\omega L_2}{c_u}) & 1 & 0 & -\sin(\frac{\omega L_2}{c_u}) & 0 \\ -\cos(\frac{\omega L_1}{c_u}) & 1 & 0 & -\sin(\frac{\omega L_1}{c_u}) & 0 & 0 \end{pmatrix} \cdot \begin{pmatrix} a_1 \\ a_2 \\ a_3 \\ b_1 \\ b_2 \\ b_3 \end{pmatrix} = 0 \tag{3.20}$$

For a non-trivial solution to exist, the coefficient matrix above must be singular, which leads to an implicit equation in the natural frequency that can be solved numerically.

Figure 3.8 shows the variation of fundamental longitudinal frequency with mass position for different masses, based on configuration 1 in Table 3.1. $\chi_m = \frac{m}{2L_e\rho}$ is the ratio of transported mass to the net cable mass. In the case where $\chi_m = 0$, the fundamental frequency is constant and is as calculated in Table 3.2. As the transported mass becomes heavier, the fundamental frequency reduces for any given position of the mass. Due to the symmetry of configuration 1, when the mass approaches the midpoint between the two pulleys, it reaches a vibration node such that the configuration is equivalent to $\chi_m = 0$. This can be verified using the cable mode shapes associated with the mass at the cable midpoint as shown in Figure 3.9. The three cable spans also behave such that their motion is coupled with pulley rotation as explained in Figure 3.10.

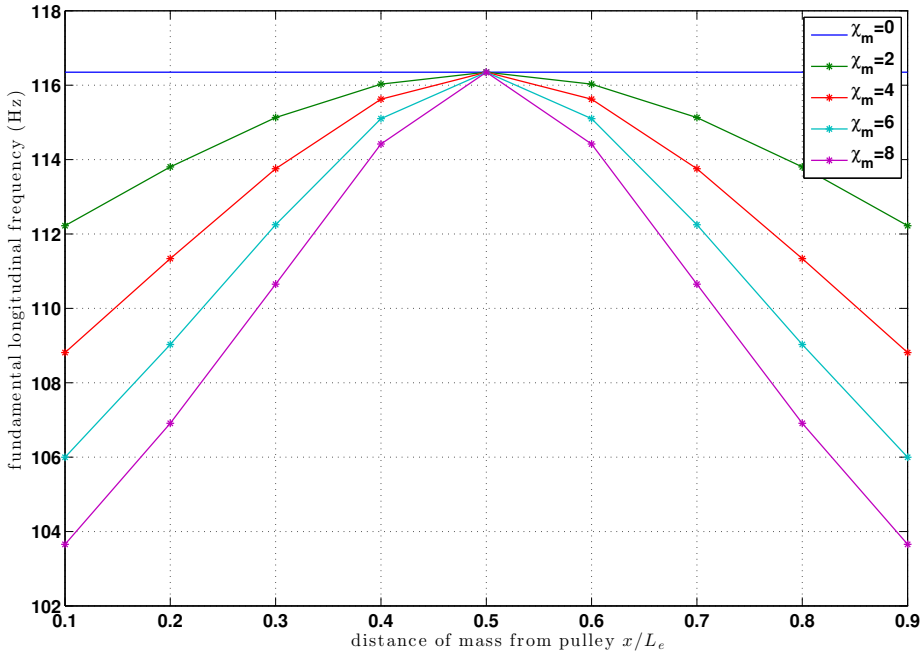

Figure 3.8. Longitudinal frequency as a function of mass and position.

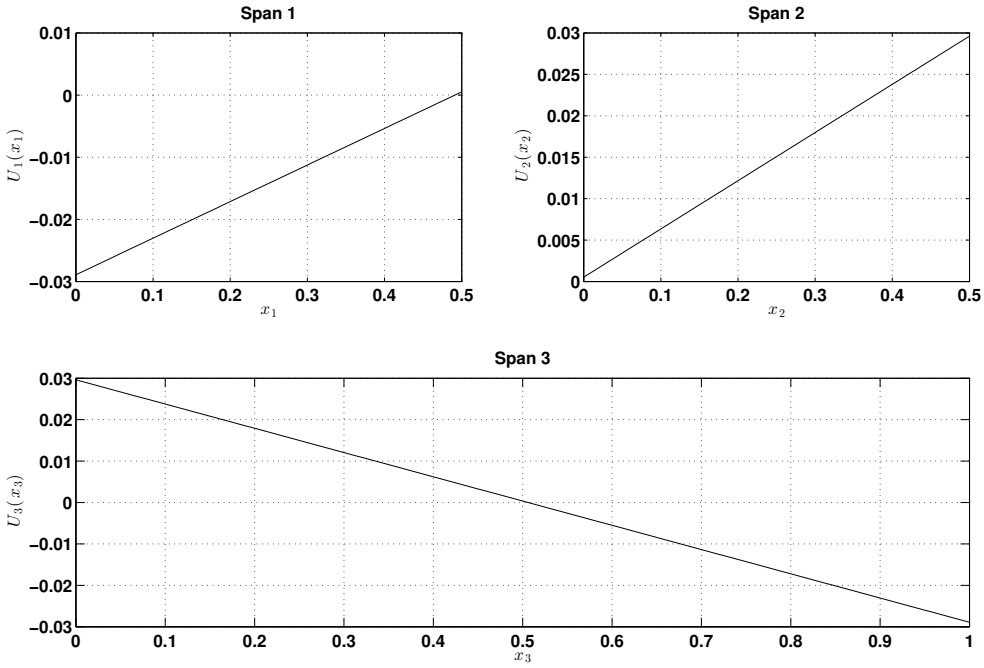

Figure 3.9. Fundamental longitudinal mode shapes for the different cable spans. Mass is at cable midpoint.

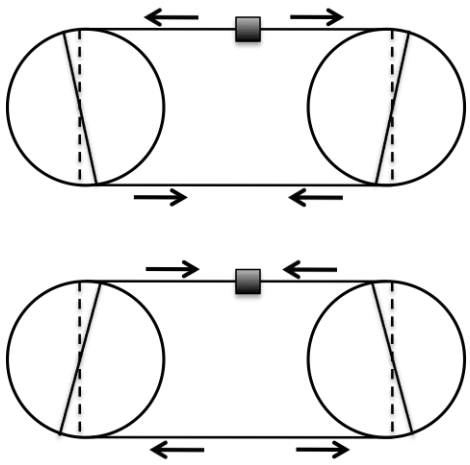

Figure 3.10. Fundamental longitudinal modes of cable transporter system.

3.3.2 Single Mass without Cable Loop

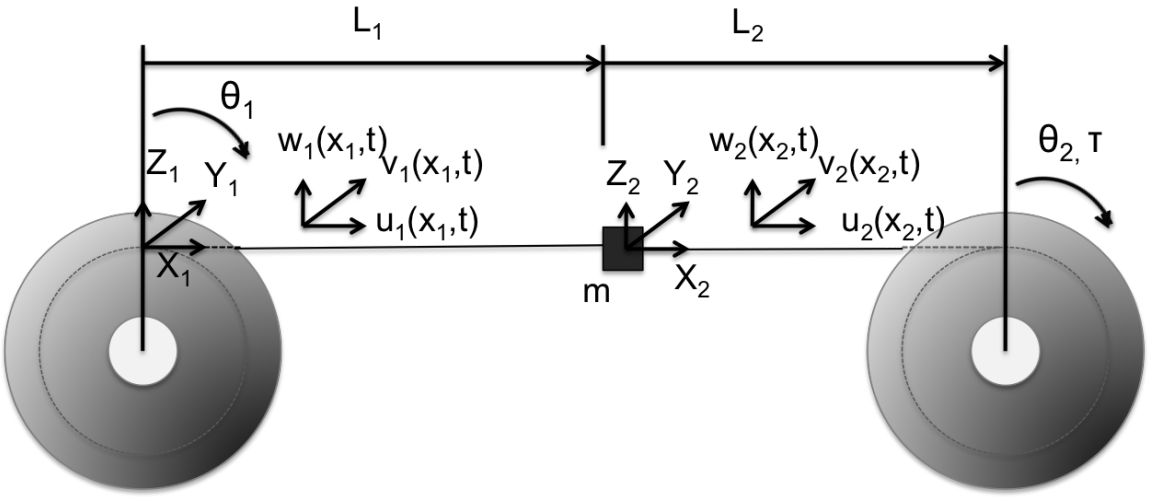

Figure 3.11. Cable transporter system without cable loop.

The linear equations of motion for the cable-transporter system without a cable loop as shown in Figure 3.11, can be written as follows:

$$\ddot{u}_1(x_1,t) = c_u^2 u_1''(x_1,t) \tag{3.21a}$$

$$\ddot{u}_2(x_2,t) = c_u^2 u_2''(x_2,t) \tag{3.21b}$$

The boundary equations and constraints are,

$$m\ddot{u}_2(0,t) = EA(u_2'(0,t) - u_1'(L_1,t) \tag{3.22a}$$

$$\frac{J_1}{r_1}\ddot{\theta}_1(t) = \frac{J_1}{r_1^2}\ddot{u}_1(0,t) = EAu_1'(0,t) \tag{3.22b}$$

$$\frac{J_2}{r_2}\ddot{\theta}_2(t) = \frac{J_2}{r_2^2}\ddot{u}_3(0,t) = EAu_3'(0,t) \tag{3.22c}$$

$$u_2(0,t) = u_1(L_1,t) \tag{3.22d}$$

Using separation of variables for the longitudinal cable displacements into spatial and temporal functions as shown,

$$\begin{pmatrix} u_1(x_1,t) \\ u_2(x_2,t) \end{pmatrix} = \begin{pmatrix} U_1(x_1) \\ U_2(x_2) \end{pmatrix} e^{i\omega t} \tag{3.23}$$

where $\frac{\omega}{2\pi}$ represents all the natural longitudinal frequencies of the system and $U_i(x_i)$ represent the mode shapes. We obtain the following spatial functions from substituting Eq. (3.23) in Eq. (3.21),

$$U_1(x_1) = a_1 \cos(\frac{\omega x_1}{c_u}) + b_1 \sin(\frac{\omega x_1}{c_u}) \tag{3.24a}$$

$$U_2(x_2) = a_2 \cos(\frac{\omega x_2}{c_u}) + b_2 \sin(\frac{\omega x_2}{c_u}) \tag{3.24b}$$

where a_i, b_i are unknown constant coefficients. Substituting the above spatial functions and Eq. (3.23) in boundary conditions Eq. (3.22), we obtain

$$m(-\omega^2)a_2 = \frac{EA\omega}{c_u}\left(b_2 + a_1 \sin(\frac{\omega L_1}{c_u}) - b_1 \cos(\frac{\omega L_1}{c_u})\right) \tag{3.25a}$$

$$\frac{J_1}{r_1^2}(-\omega^2)a_1 = \frac{EA\omega}{c_u} b_1 \tag{3.25b}$$

$$\frac{J_2}{r_2^2}(\omega^2)\left(a_2 \cos(\frac{\omega L_2}{c_u}) + b_2 \sin(\frac{\omega L_2}{c_u})\right) = \frac{EA\omega}{c_u}\left(-a_2 \sin(\frac{\omega L_2}{c_u}) + b_2 \cos(\frac{\omega L_2}{c_u})\right) \tag{3.25c}$$

$$a_1 \cos(\frac{\omega L_1}{c_u}) + b_1 \sin(\frac{\omega L_1}{c_u}) = a_2 \tag{3.25d}$$

Eq. (3.25) re-arranged and written in matrix form is given by,

$$\begin{pmatrix} \sin(\frac{\omega L_1}{c_u}) & \frac{m\omega}{c_u \rho} & -\cos(\frac{\omega L_1}{c_u}) & 1 \\ \frac{J_1 \omega}{c_u \rho r_1^2} & 0 & 1 & 0 \\ 0 & -\frac{J_2 \omega}{c_u \rho r_2^2}\cos(\frac{\omega L_2}{c_u}) - \sin(\frac{\omega L_2}{c_u}) & 0 & -\frac{J_2 \omega}{c_u \rho r_2^2}\sin(\frac{\omega L_2}{c_u}) + \cos(\frac{\omega L_2}{c_u}) \\ \cos(\frac{\omega L_1}{c_u}) & -1 & \sin(\frac{\omega L_1}{c_u}) & 0 \end{pmatrix} \cdot \begin{pmatrix} a_1 \\ a_2 \\ b_1 \\ b_2 \end{pmatrix} = 0 \tag{3.26}$$

The natural frequencies of the system are obtained from the condition of singularity imposed on the above matrix.

3.3.3 Single Mass - Lateral

When the transported mass is not supported in the vertical direction it has an additional degree of freedom. The linear transverse dynamics of the upper cable spans are given by,

$$\ddot{w}_1(x_1,t) = c_w^2 w_1''(x_1,t) \tag{3.27a}$$

$$\ddot{w}_2(x_2,t) = c_w^2 w_2''(x_2,t) \tag{3.27b}$$

The variable-separable solution to the above wave equations are expressed as follows:

$$w_1(x_1,t) = \left(b_{11}\cos(\frac{\omega x_1}{c_w}) + b_{12}\sin(\frac{\omega x_1}{c_w}) \right) e^{i\omega t} \tag{3.28a}$$

$$w_2(x_2,t) = \left(b_{21}\cos(\frac{\omega x_2}{c_w}) + b_{22}\sin(\frac{\omega x_2}{c_w}) \right) e^{i\omega t} \tag{3.28b}$$

where $\frac{\omega}{2\pi}$ represents the transverse oscillation frequency of the transported mass. Figure 3.12 shows the forces on the transported mass at equilibrium and during cable motion respectively. The dynamic equations of the mass at equilibrium and during motion are as follows:

$$T_0 \sin\theta_{1e} + T_0 \sin\theta_{2e} = mg \tag{3.29a}$$

$$T_1 \sin\theta_1 + T_2 \sin\theta_2 - mg = m\ddot{y}(t) \tag{3.29b}$$

where $y(t)$ is the vertical displacement of the transported mass from its equilibrium position and $\theta_1, \theta_2, \theta_{1e}, \theta_{2e}$ are sag angles with respect to the horizontal caused by the mass's vertical displacement. From Figure 3.12 (a) and (b), the following approximate relationships are obtained:

$$\sin\theta_1 = \frac{H - y(t)}{L_1} = \sin\theta_{1e} - \frac{y(t)}{L_1} \tag{3.30a}$$

$$\sin\theta_2 = \frac{H - y(t)}{L_2} = \sin\theta_{2e} - \frac{y(t)}{L_2} \tag{3.30b}$$

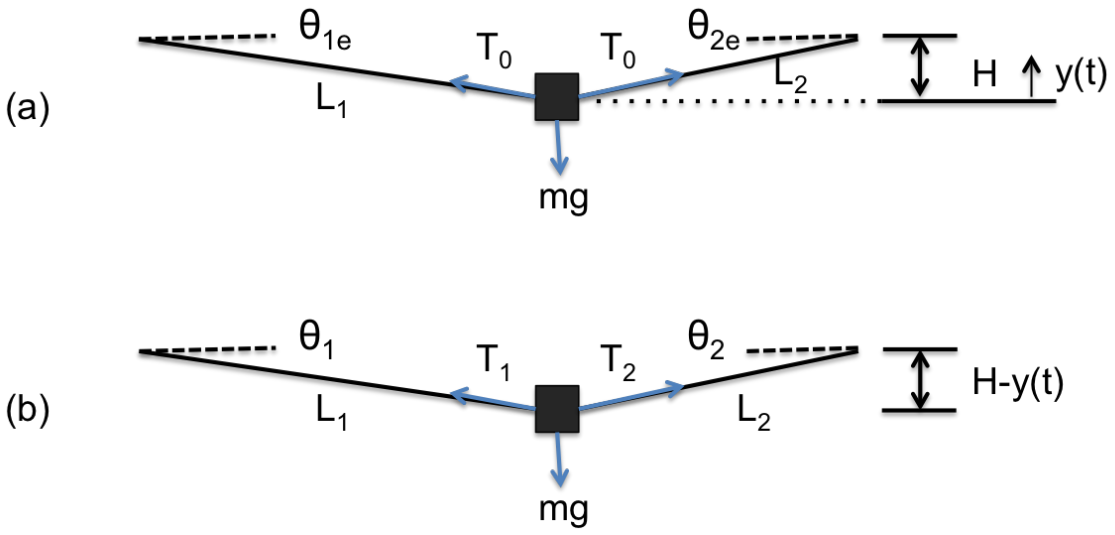

Figure 3.12. Forces on transported mass.

Substituting for tension and the above relationships in Eq. (3.29b),

$$T_0 \sin\theta_{1e} - T_0\frac{y(t)}{L_1} + EAu_1' \sin\theta_1 + T_0 \sin\theta_{2e} \\ - T_0\frac{y(t)}{L_2} + EAu_2' \sin\theta_2 - mg = m\ddot{y}(t) \tag{3.31}$$

Simplifying the above using the equilibrium condition in Eq. (3.29a), we obtain

$$\ddot{y}(t) + \frac{T_0}{m}(\frac{1}{L_1} + \frac{1}{L_2})y(t) = \frac{EA}{m}(u_1' \sin\theta_1 + u_2' \sin\theta_2) \tag{3.32}$$

In applications where cable sag and longitudinal displacements are not negligible, Eq. (3.32) provides a more accurate description of the vertical dynamics of the transported mass, where the right-hand term represents a kind of forcing function. When cable sag and longitudinal cable displacements are small, the higher order terms on the right can be ignored, leading to the following transverse dynamics.

$$\ddot{y}(t) + \frac{T_0}{m}(\frac{1}{L_1} + \frac{1}{L_2})y(t) = 0 \tag{3.33}$$

The mass boundary condition for the second cable span is obtained from Eq. (3.28b) as follows:

$$w_2(0,t) = y(t) = b_{21}e^{i\omega t} \tag{3.34}$$

Substituting the above in Eq. (3.33), the natural transverse vibration frequency of the transported mass is given by,

$$\omega = \frac{1}{2\pi}\sqrt{\frac{T_0}{m}(\frac{1}{L_1}+\frac{1}{L_2})} \tag{3.35}$$

3.3.4 Two Masses in Parallel

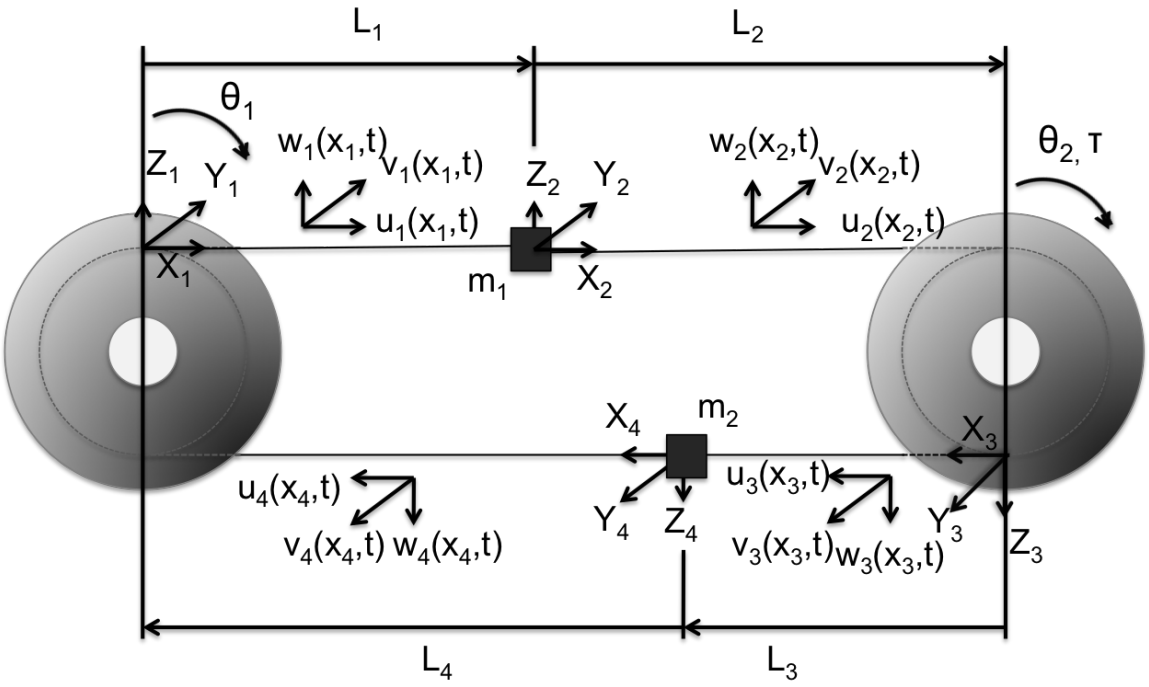

Figure 3.13. Cable transporter system with two masses in parallel.

A 2-mass cable transporter system is shown in Figure 3.13. This is a common configuration used in monocable ropeways. The following are the linear equations of motion of the system.

$$\ddot{u}_1(x_1,t) = c_u^2 u_1''(x_1,t) \tag{3.36a}$$

$$\ddot{u}_2(x_2,t) = c_u^2 u_2''(x_2,t) \tag{3.36b}$$

$$\ddot{u}_3(x_3,t) = c_u^2 u_3''(x_3,t) \tag{3.36c}$$

$$\ddot{u}_4(x_4,t) = c_u^2 u_4''(x_4,t) \tag{3.36d}$$

The dynamic boundary conditions and constraints are as follows,

$$m_1\ddot{u}_2(0,t) = EA(u_2'(0,t) - u_1'(L_1,t)) \tag{3.37a}$$

$$m_2\ddot{u}_4(0,t) = EA(u_4'(0,t) - u_3'(L_3,t)) \tag{3.37b}$$

$$\frac{J_1}{r_1}\ddot{\theta}_1(t) = \frac{J_1}{r_1^2}\ddot{u}_1(0,t) = EA(u_1'(0,t) - u_4'(L_4,t)) \tag{3.37c}$$

$$\frac{J_2}{r_2}\ddot{\theta}_2(t) = \frac{J_2}{r_2^2}\ddot{u}_3(0,t) = EA(u_3'(0,t) - u_2'(L_2,t)) \tag{3.37d}$$

$$u_1(0,t) = u_4(L_4,t) \tag{3.37e}$$

$$u_3(0,t) = u_2(L_2,t) \tag{3.37f}$$

$$u_2(0,t) = u_1(L_1,t) \tag{3.37g}$$

$$u_4(0,t) = u_3(L_3,t) \tag{3.37h}$$

Substituting the variable-separable form of the cable displacements in Eq. (3.37), the following matrix form is obtained:

$$\begin{pmatrix} S_1 & \frac{m_1\omega}{c_u\rho} & 0 & 0 & -C_1 & 1 & 0 & 0 \\ 0 & 0 & S_3 & \frac{m_2\omega}{c_u\rho} & 0 & 0 & -C_3 & 1 \\ \frac{J_1\omega}{c_u\rho r_1^2} & 0 & 0 & S_4 & 1 & 0 & 0 & -C_4 \\ 0 & S_2 & \frac{J_2\omega}{c_u\rho r_2^2} & 0 & 0 & -C_2 & 1 & 0 \\ 1 & 0 & 0 & -C_4 & 0 & 0 & 0 & -S_4 \\ 0 & -C_2 & 1 & 0 & 0 & -S_2 & 0 & 0 \\ -C_1 & 1 & 0 & 0 & -S_1 & 0 & 0 & 0 \\ 0 & 0 & -C_3 & 1 & 0 & 0 & -S_3 & 0 \end{pmatrix} . \begin{pmatrix} a_1 \\ a_2 \\ a_3 \\ a_4 \\ b_1 \\ b_2 \\ b_3 \\ b_4 \end{pmatrix} = 0 \tag{3.38}$$

where $S_i = \sin(\frac{\omega L_i}{c_u}),\ C_i = \cos(\frac{\omega L_i}{c_u}),\ i = 1, 2, 3, 4$. The longitudinal natural frequencies of the system are obtained by imposing the condition of singularity on the modal matrix in Eq. (3.38).

4. SYSTEM IDENTIFICATION

In order to implement model-based feedback controllers on the system, a good system model with accurate parameters is crucial. In the following sections, the complete experimental setup is described in detail followed by parameter estimation of the drive motor and pulleys, frequency response measurements of the cable-pulley system and servoamplifier

4.1 Experimental Setup

A schematic of the prototypical cable-pulley system is shown in Figure 4.1 and consists of the following major components: (i) Drive pulley setup, (ii) Load pulley setup, (iii) Monofilament cable loop. The drive and load pulleys are attached using set screws to 0.5inch diameter steel shafts that are mounted on ball bearings for transverse load support and smooth rotation. Transverse loads are forces acting perpendicular to the shaft. In the case of the cable-pulley system, most of these forces are due to cable tension. The drive pulley mounted on the steel shaft is connected to the motor shaft using a coupler with four clamping screws and keyways on both ends for additional shaft support. The drive motor is mounted on a sleeve-bearing carriage that can be tightened with a hand brake as shown in Figure 4.2. Hence the distance between the drive pulley and load pulley can be freely adjusted by sliding the carriage along the 8020 bar. The complete drive side of the setup is shown in Figure 4.3.

A single monofilament cable loop is used to connect the drive pulley to the load pulley. The load pulley shaft and ball bearings are mounted on pillow blocks that move freely on two linear shafts. As the cable is under positive tension, the load pulley side of the setup is pulled against a fixed compressive load cell (Loadstar Sensors). As a result, the load cell measures the combined tension of the upper and lower cable

spans from which individual cable tension can be calculated. The load side of the setup is shown in Figure 4.4.

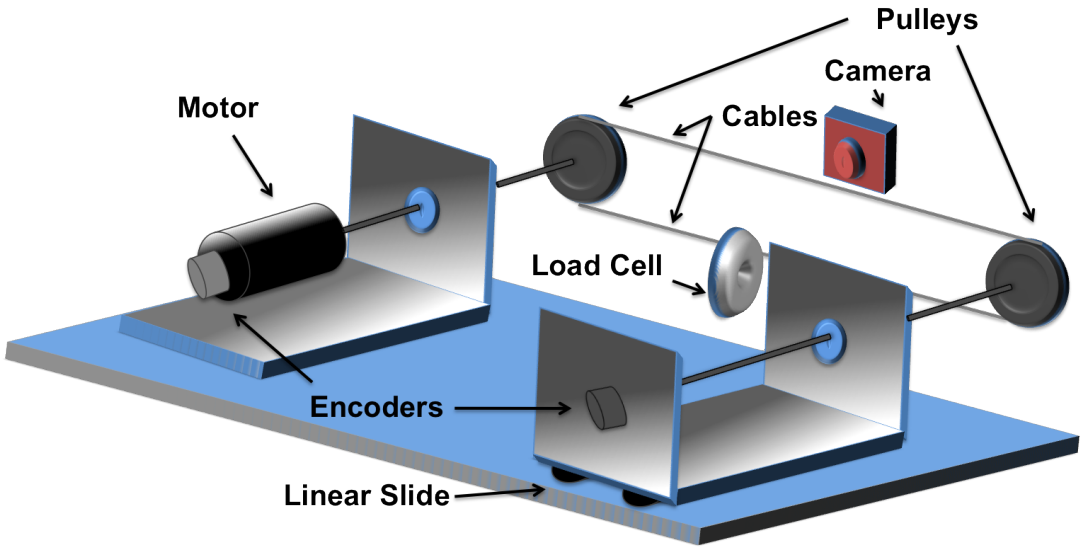

Figure 4.1. Experimental setup of cable-pulley system.

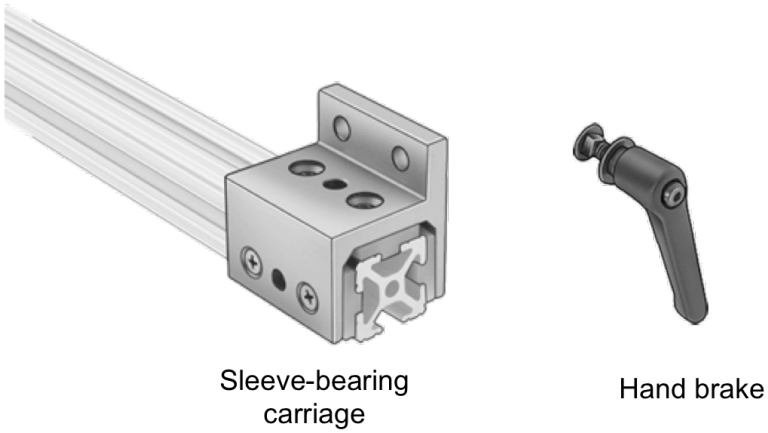

Figure 4.2. Sleeve-carriage mounted on 8020 bar and hand brake.

The complete cable-pulley setup is shown in Figure 4.5. A brushed motor (Maxon Motors) rated for 240W with a nominal speed of 5680RPM, a nominal voltage of 24V

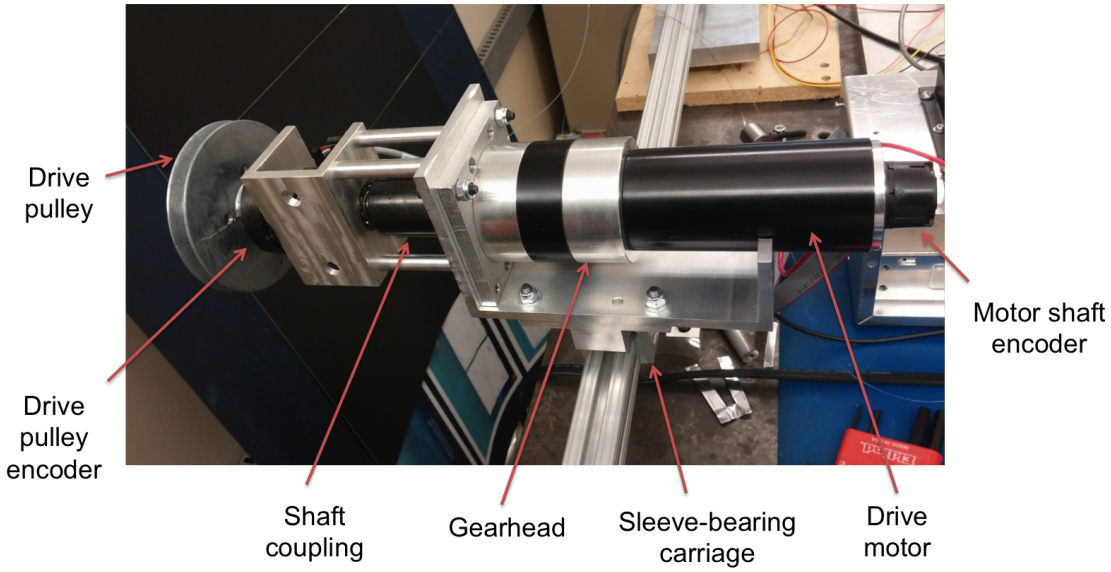

Figure 4.3. Drive pulley setup.

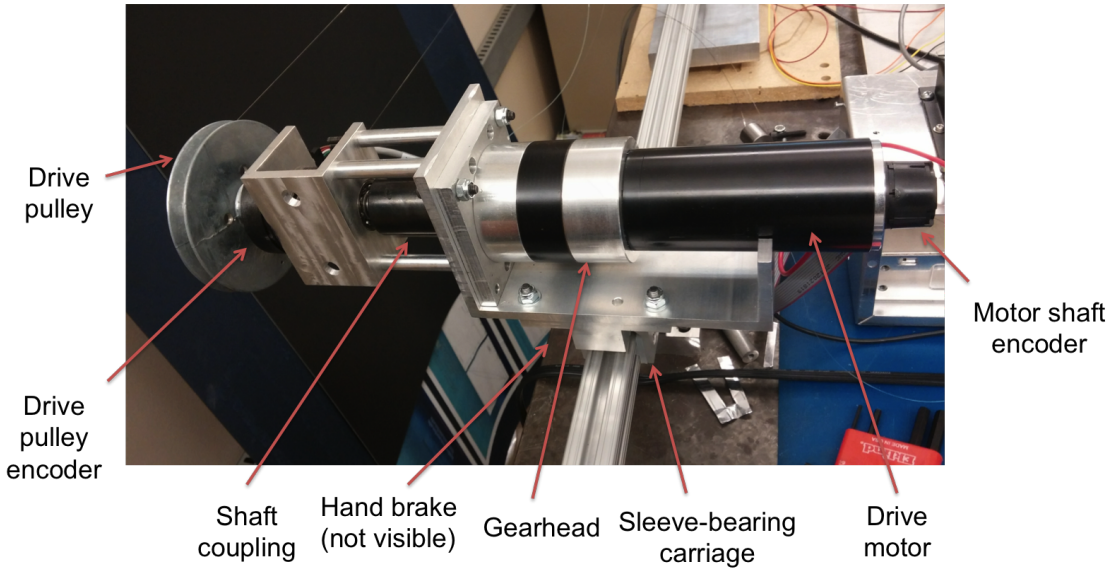

Figure 4.4. Load pulley setup.

and a nominal torque of 0.405Nm is used. It is connected to a planetary gearhead with a gear ratio of 5.2 resulting in a nominal torque of 2.1Nm and a nominal speed

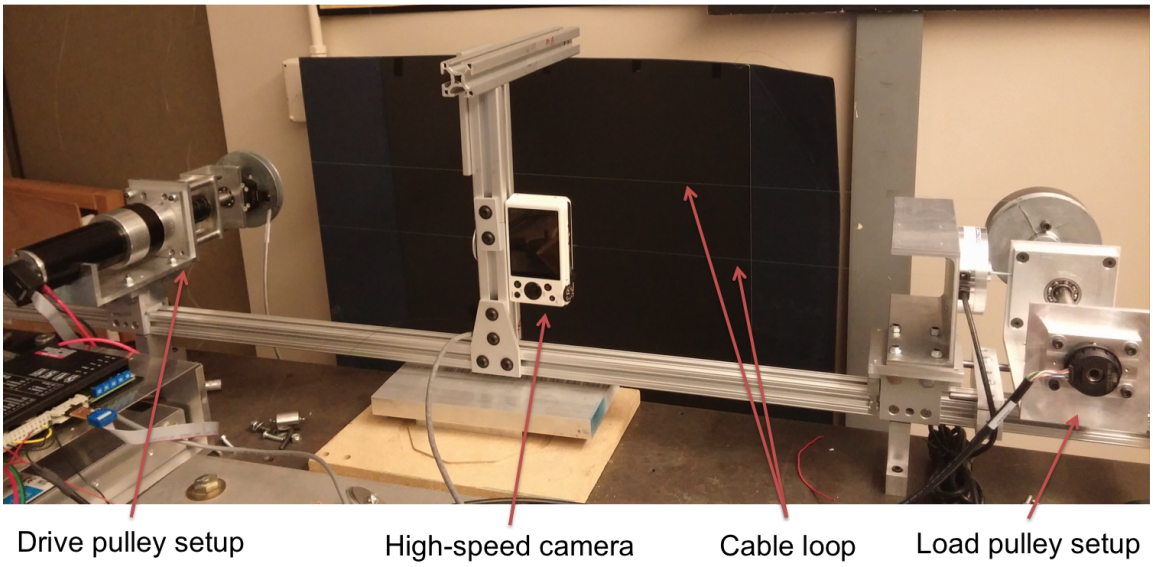

Figure 4.5. Complete cable-pulley setup.

of 1092RPM. The motor shaft is pre-assembled to be connected to an optical encoder with 500 counts per revolution. Due to the gearhead, the resulting encoder resolution is 2600 counts per revolution (CPR). More specifications of the drive motor, gear head and motor encoder can be found in Tables A.1-A.2. Two optical encoders (US Digital) with resolutions of 10000CPR each are mounted on the drive pulley and load pulley shafts. The entire system is controlled by dSpace DS1103 controller board and monitored by a host computer with a Pentium 4 processor.

A high-speed camera with a maximum speed of 480 frames/sec is mounted near the cable midpoint to capture cable motion. As the frame rate of the camera is increased from its lowest value, the resolution of each frame in any recorded video was reduced automatically. When used at the highest frame rate of 480 frames/sec, the video resolution was set to 224x160 pixels. In order to simplify the image processing needed to capture cable vibrations using the camera, the cable was spray-painted black and a small segment of the cable midpoint was painted white. The camera was then used to record videos of cable vibrations against a black background as shown in

Figure 4.5. Post-processing of the video frames is illustrated in Figure 4.6 where (a) is an original frame from the recorded video, (b) is the frame converted to greyscale and contains imperfections and (c) is the final frame after removal of unwanted pixels. The centroid of the white pixels in the final corrected frame is then calculated to track the motion of the cable midpoint.

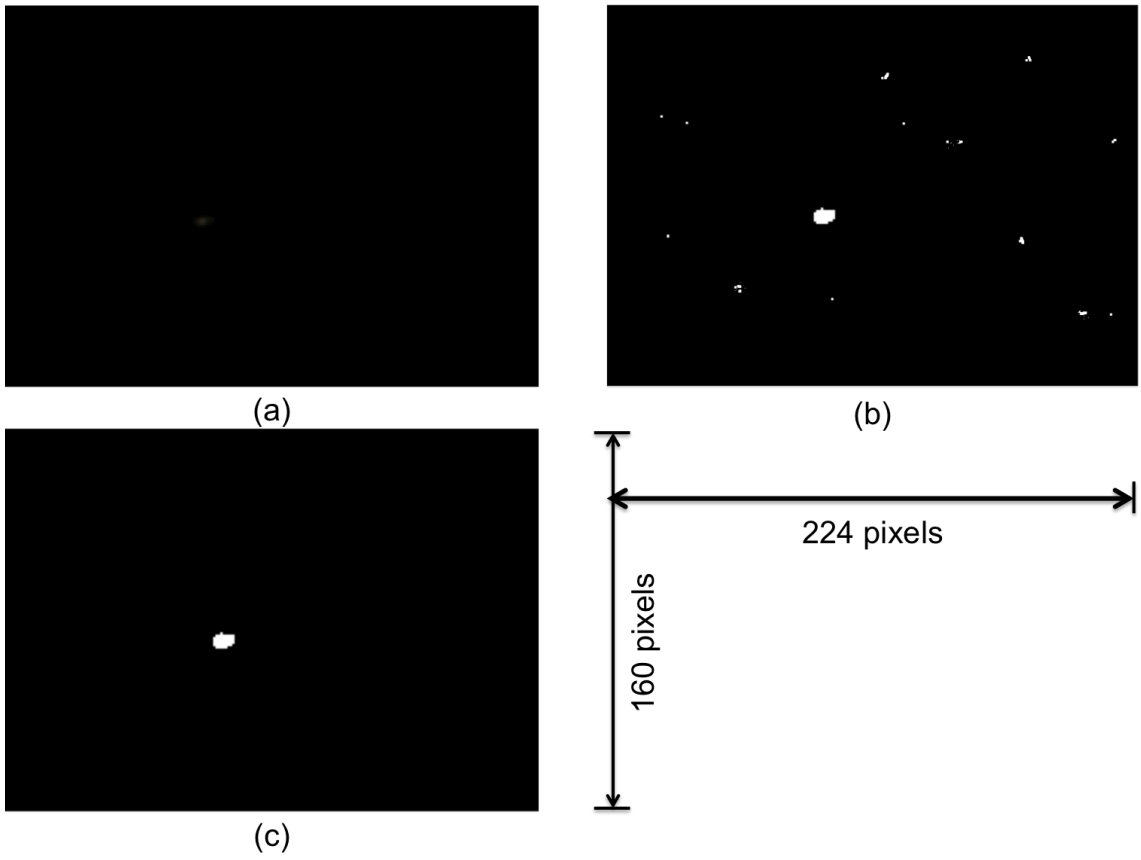

Figure 4.6. Processing of frames captured by the high-speed camera. (a) Original frame, (b) Frame in greyscale with errors, (c) Corrected frame.

4.2 Parameter Estimation using Linear Least Squares

Experiments were performed to estimate motor parameters such as inertia, damping and friction. The principle behind the least-square estimation is described below. Using a sampling rate of 1kHz, motor torque was calculated using current measurements and the torque constant from motor specs. To reduce measurement noise from the optical encoder, the angular position was filtered using a low-pass second-order filter. The filter transfer function is as follows:

$$H_f(s) = \frac{\omega_f^2}{s^2 + 2\zeta_f\omega_f s + \omega_f^2} \tag{4.1}$$

where ζ_f, ω_f are damping ratio and natural frequency of the filter, respectively. Choosing states $x_1 = \theta_f$ = filtered angular position and $x_2 = \dot{\theta}_f$ = filtered angular velocity, the following filter dynamics was used to obtain filtered angular position:

$$\begin{aligned} \dot{x}_1 &= x_2 \\ \dot{x}_2 &= -2\zeta_f\omega_f x_2 - \omega_f^2(x_1 - \theta(t)) \end{aligned} \tag{4.2}$$

where $\theta(t)$ is the measured angular position. When the equation of motion is written linearly in terms of the unknown parameters, a linear least-square solution can be obtained using measurements. This gives us the parametric solution that minimizes the sum of the squares of error with respect to all measurements. More information on this technique can be found in [83]. In the linear form, the equation of motion is written as:

$$y_m(t) = \phi(t)P \tag{4.3}$$

where $y_m(t)$ is a measured output, $\phi(t)$ is the regressor vector and P is the associated vector of unknown constant parameters. Applying the filter, the equation of motion can be rewritten as follows:

$$y_f(t) = \phi_f(t)P \tag{4.4}$$

In the Laplace domain,

$$y_f = H_f(s)y_m \tag{4.5a}$$

$$\phi_f = H_f(s)\phi \tag{4.5b}$$

Using measurements taken at discrete time steps $t_j = jT_s,\ j = 0, 1, 2...$ where T_s is the sampling time interval, gives the following equation of motion.

$$y_f(t_j) = \phi_f(t_j)P \tag{4.6}$$

Combining the measurements at multiple times gives vector Y_f and matrix Φ_f. Hence the vector of parameter estimates that minimizes error is obtained by solving:

$$\Phi_f^T Y_f = (\Phi_f^T \Phi_f)P \tag{4.7}$$

The least square solution is given by $\hat{P} = (\Phi_f^T \Phi_f)^{-1}\Phi_f^T Y_f$. The inverse of $\Phi_f^T \Phi_f$ exists if the measurements are sufficiently rich.

4.2.1 Motor and Drive Pulley Identification

The drive pulley was attached to the motor shaft using the coupling. The motor dynamics is given by,

$$J_1\ddot{\theta} + b_1\dot{\theta} + c_1 tanh(K\dot{\theta}) = \tau(t) + d + \tilde{d}(t) \tag{4.8}$$

where J_1, b_1, c_1 are the combined motor and drive pulley inertia, viscous and coulomb friction parameters, respectively. The hyperbolic tangent function with $K = 0.5$ was used to smoothly approximate the signum function such that numerical errors in angular velocity fall within the linear slope region. d is the nominal part of the lumped modeling error and $\tilde{d}(t)$ is the unknown time-varying part. τ is the measured motor torque. The above motor dynamics can be written in linear form as follows:

$$\begin{aligned} \tau(t) &= [\ddot{\theta}, \dot{\theta}, tanh(0.5\dot{\theta}), -1](t)P - \tilde{d}(t) \\ &= \phi(t)P - \tilde{d}(t) \end{aligned} \tag{4.9}$$

where parameter vector $P = [J_1, b_1, c_1, d]^T$. Applying the filter to the above equation, the dynamics can be rewritten as follows:

$$\begin{aligned}\tau_f(t) &= [\ddot{\theta}, \dot{\theta}, tanh(0.5\dot{\theta}), -1]_f(t)\hat{P} - \tilde{d}_f(t) \\ &= [\ddot{\theta}_f, \dot{\theta}_f, (tanh(0.5\dot{\theta}))_f, (-1)_f](t)\hat{P} - \tilde{d}_f(t) \\ &= \phi_f(t)\hat{P} - \tilde{d}_f(t) \end{aligned} \tag{4.10}$$

where $\hat{P}$ is the linear least-square estimate of the parameters and is obtained from the matrix form in Eq. (4.7).

In order to verify the accuracy of the estimated parameters, the predicted modeling error $\tilde{d}(t)$ is calculated using the true values of angular velocity ($\dot{\theta}$) and angular acceleration ($\ddot{\theta}$) used in Eq. (4.9). To obtain them, $\dot{\theta}$ and $\ddot{\theta}$ are first numerically calculated from position measurement (θ), using finite central differences. They are then processed using Matlab's $idealfilter$ function which applies an ideal low-pass filter using a given cut-off frequency. This is done to remove noise from encoder measurements as well as numerical differentiation thereby giving their best estimates. Since the filter is ideal and non-causal, no phase lag is introduced.

Experiment 1 using 3Hz+4Hz torques

The motor was excited using a sum of sinusoidal torques of 3Hz and 4Hz for about 70 seconds with an amplitude of 0.1V each. Encoder measurements were filtered using the causal filter with $\zeta_f = 1$ and $\omega_f = 2\pi(20)rad/s$. Figure 4.7 shows the unfiltered and filtered regressor functions plotted during the first second of collected data. An ideal filter with a cut-off frequency of 50Hz was used to obtain the best estimate of angular velocity and acceleration. Figure 4.8 shows the modeling error $\tilde{d}(t)$ calculated from Eq. (4.9) and is seen to be quite small comported to the applied torque.

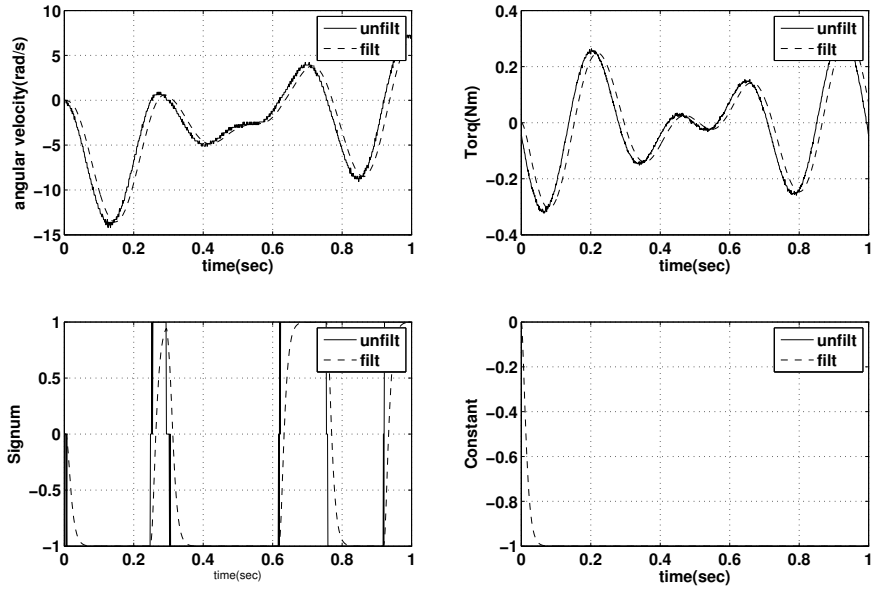

Figure 4.7. Comparison of unfiltered and filtered regressors.

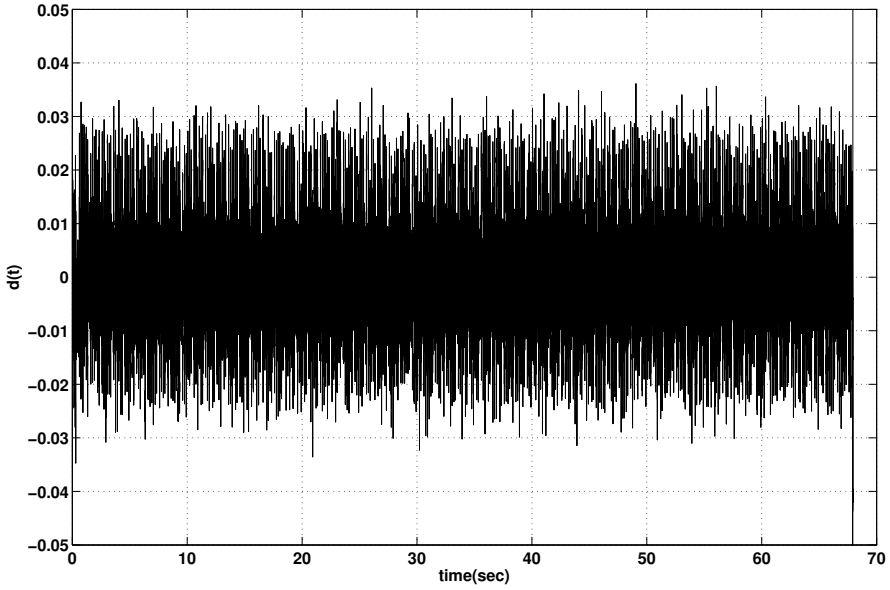

Figure 4.8. Modeling error $\tilde{d}(t)$.

Experiment 2 using 1Hz+5Hz torques

In the second experiment, the motor was excited using a sum of sinusoidal torques of 1Hz and 5Hz for about 70 seconds with an amplitude of 0.1V each. Figure 4.9 shows the unfiltered and filtered regressor functions plotted during the first few seconds of collected data. Figure 4.10 shows the modeling error $\tilde{d}(t)$.

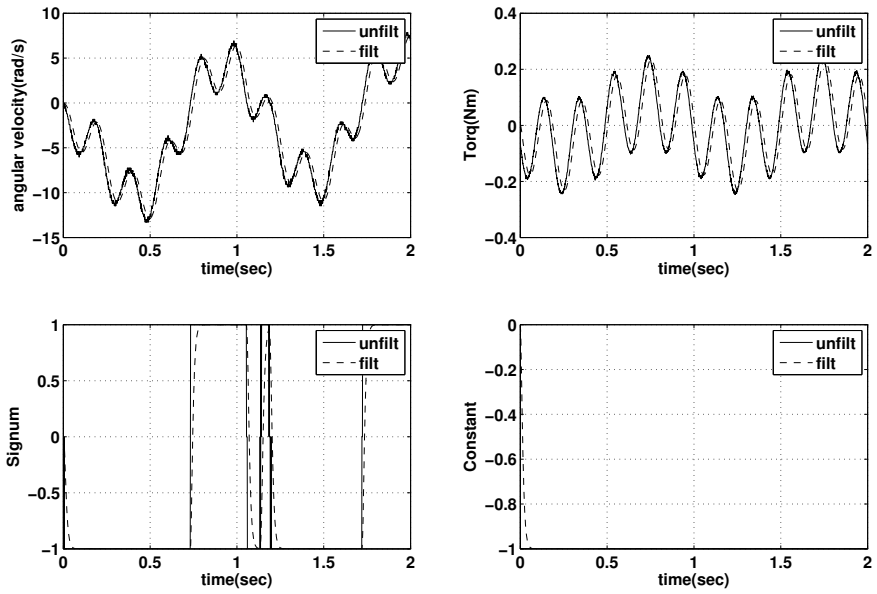

Figure 4.9. Comparison of unfiltered and filtered regressors.

Experiment 3 using 1Hz+3Hz+5Hz torques

In the third experiment, the motor was excited using a sum of sinusoidal torques of 1Hz, 3Hz and 5Hz for about 70 seconds with an amplitude of 0.1V each. Figure 4.11 shows the unfiltered and filtered regressor functions during the first two seconds of collected data. Figure 4.12 shows the modeling error.

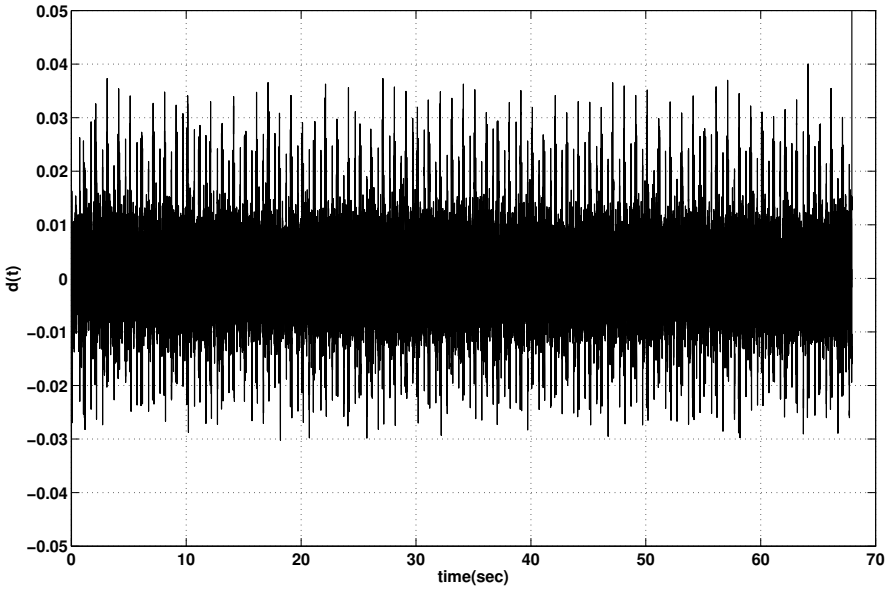

Figure 4.10. Modeling error $\tilde{d}(t)$.

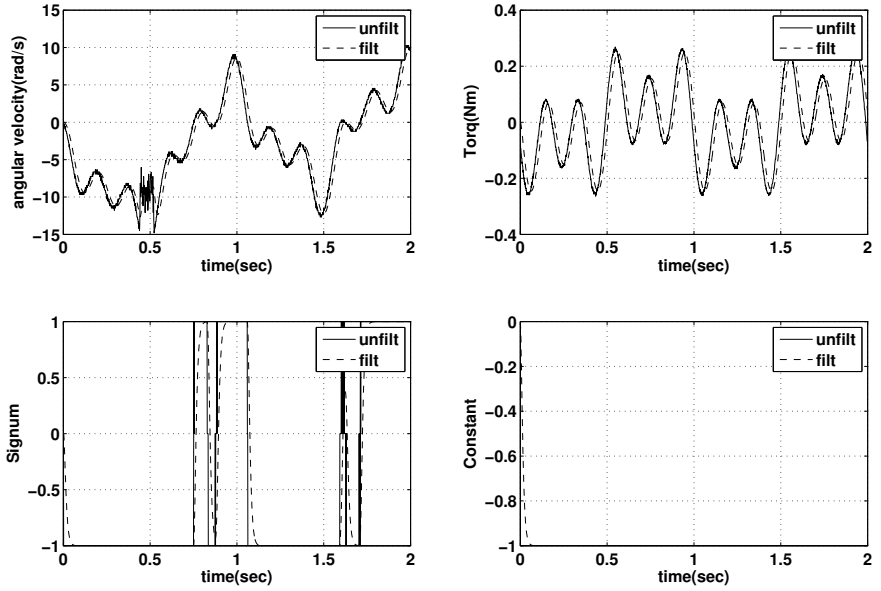

Figure 4.11. Comparison of unfiltered and filtered regressors.

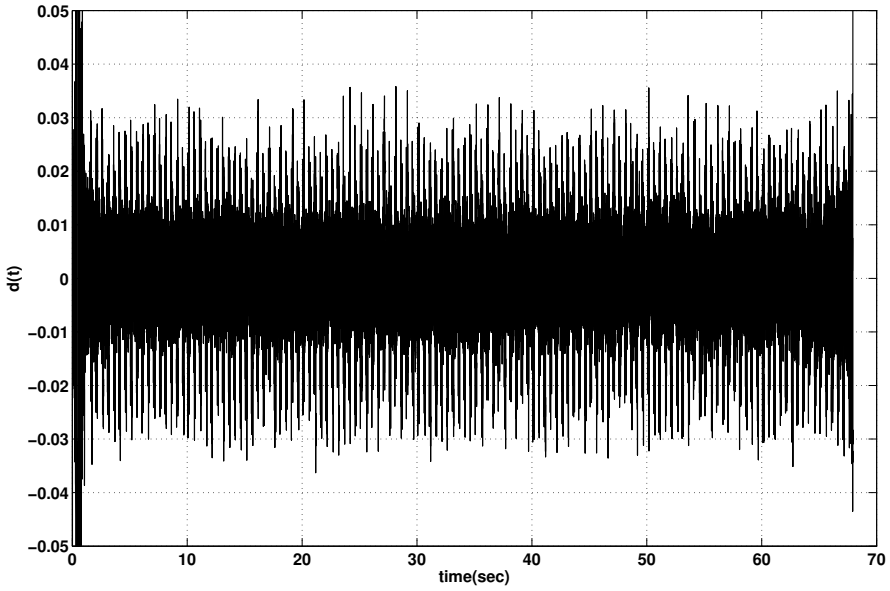

Figure 4.12. Modeling error $\tilde{d}(t)$.

4.2.2 Motor Identification

The drive pulley and shaft coupling were detached from the motor shaft. As a result, the dynamics is given by,

$$J_{11}\ddot{\theta} + b_1\dot{\theta} + c_1 tanh(0.5\dot{\theta}) = \tau(t) + d + \tilde{d}(t) \tag{4.11}$$

where J_{11} is the inertia of the motor only. The same notation is retained for damping and friction parameters since they are not expected to change significantly. The motor was excited using a sum of sinusoidal torques of 1Hz, 3Hz and 5Hz for about 55 seconds with an amplitude of 0.05V, 0.05V and 0.1V respectively. Figure 4.13 shows the unfiltered and filtered regressor functions during the first two seconds of collected data. Figure 4.14 shows the modeling error.

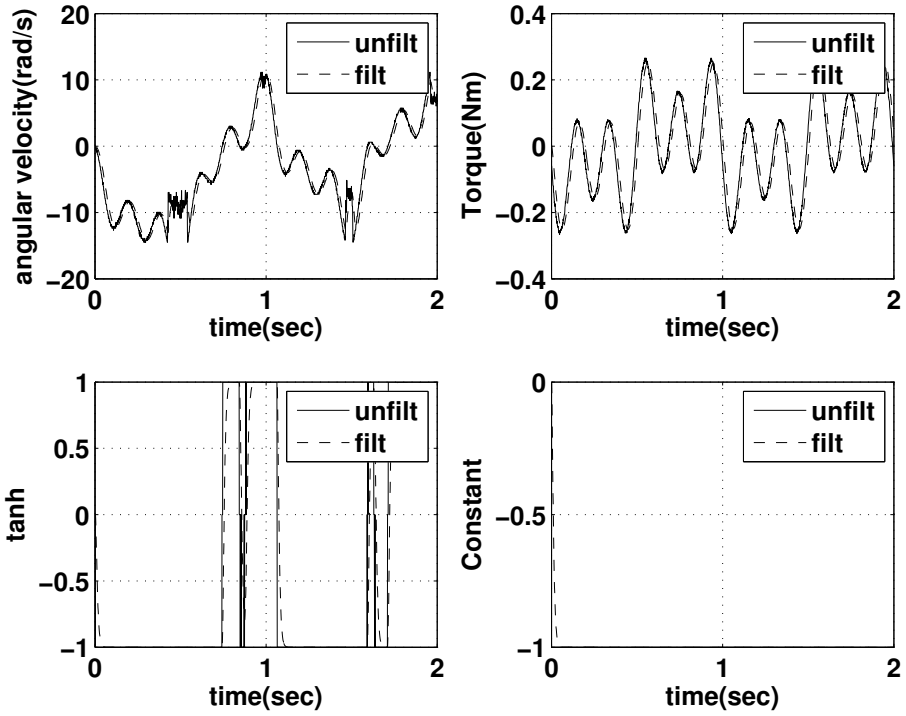

Figure 4.13. Comparison of unfiltered and filtered regressors.

4.2.3 Motor and Load Pulley Identification

The load pulley was attached to the motor shaft using the coupling. Hence the dynamics is given by,

$$(J_{11} + J_2)\ddot{\theta} + b_1\dot{\theta} + c_1 tanh(0.5\dot{\theta}) = \tau(t) + d + \tilde{d}(t) \tag{4.12}$$

where J_{11} is the motor inertia and J_2 is the load pulley inertia. The motor was excited using a sum of sinusoidal torques of 1Hz, 3Hz and 5Hz for about 55 seconds with amplitudes of 0.05V, 0.05V and 0.1V. Figure 4.15 shows the unfiltered and filtered regressor functions magnified during the first two seconds of collected data. Figure 4.16 shows the modeling error.

The estimated parameter values from all experiments performed are shown in Table 4.1. It can be seen that damping and friction coefficient estimates are fairly consis-

Table 4.1. Linear least-square parameter estimates.

Motor only				
Torque	J_{11} (kgm^2)	b_1 (Nms)	c_1 (Nm)	d (Nm)
1Hz+3Hz+5Hz	0.0011	0.00216	0.024	-0.0057
Motor and drive pulley				
Torque	$J_{11} + J_{12}$ (kgm^2)	b_1 (Nms)	c_1 (Nm)	d (Nm)
1Hz+3Hz+5Hz	0.001742	0.0031	0.0376	-0.0006
Motor and load pulley				
Torque	$J_{11} + J_2$ (kgm^2)	b_1 (Nms)	c_1 (Nm)	d (Nm)
1Hz+3Hz+5Hz	0.00345	0.005	0.045	-0.0008

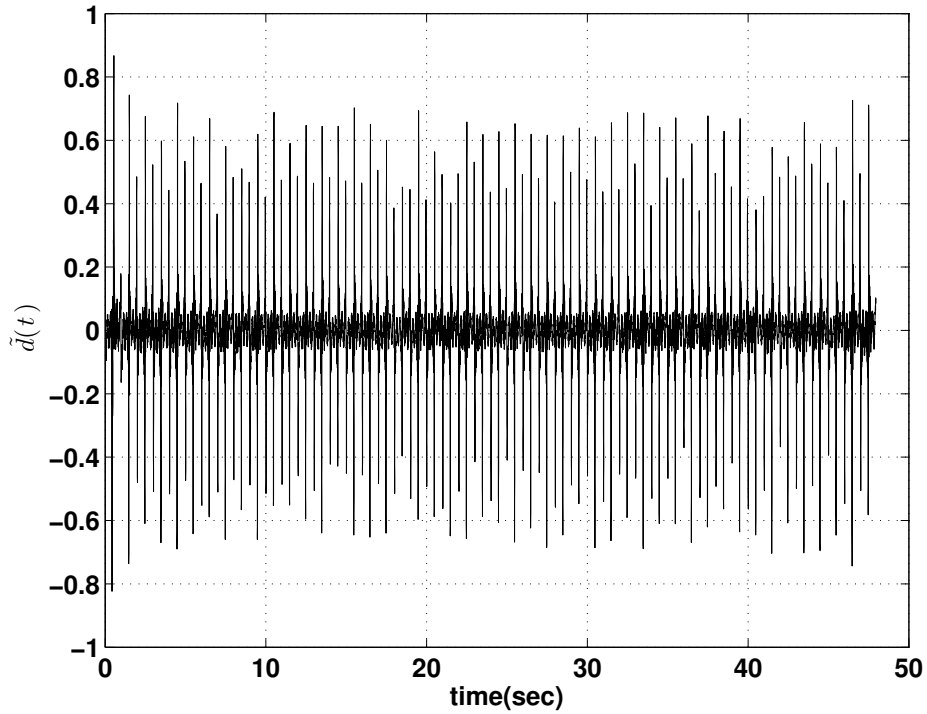

Figure 4.14. Modeling error $\tilde{d}(t)$.

tent with only a small increase with increasing inertia. This is most likely due to a higher turning resistance exhibited by the ball bearings supporting the shaft, as more transverse load acts on it. Using the estimated inertias in Table 4.1, J_{11}, J_{12} and J_2 are calculated and shown in Table 4.2.

Table 4.2. Inertias estimated offline.

$J_1(kgm^2)$	$J_{11}(kgm^2)$	$J_{12}(kgm^2)$	$J_2(kgm^2)$
0.001742	0.0011	0.000642	0.00235

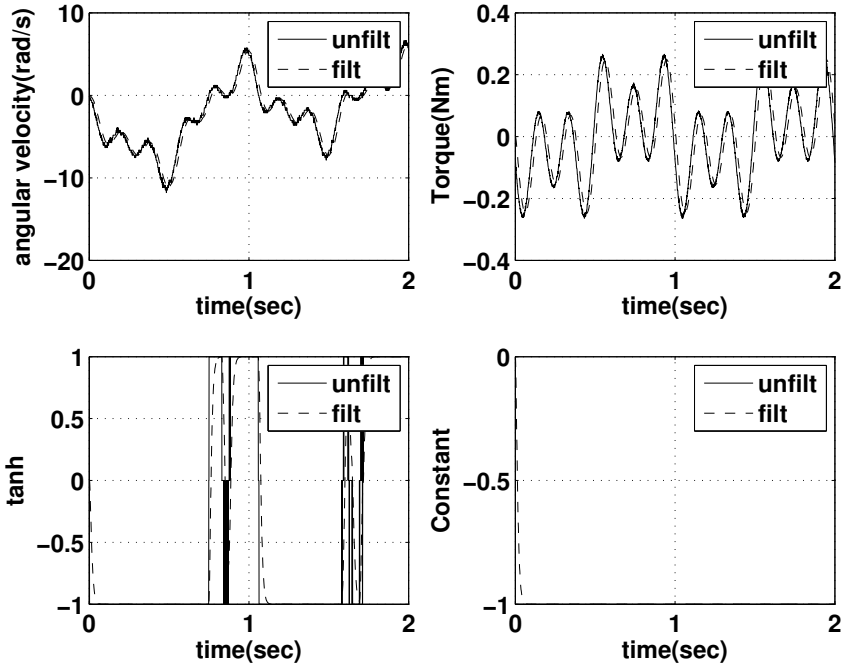

Figure 4.15. Comparison of unfiltered and filtered regressors.

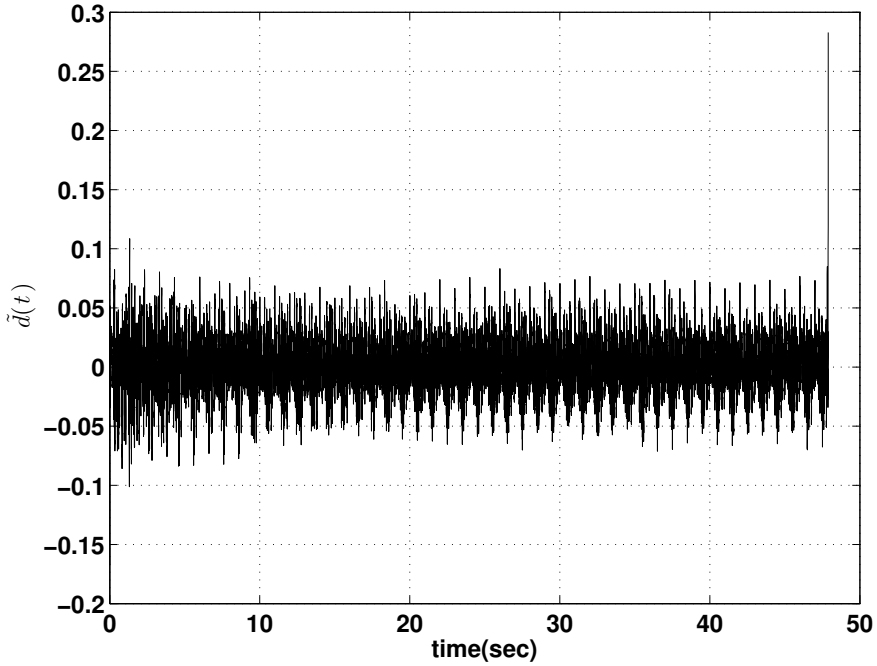

Figure 4.16. Modeling error $\tilde{d}(t)$.

4.3 Validation using Frequency Response

In this section, results from the frequency response of the cable-pulley system are presented to validate the estimated parameters of the system. The motor is excited using a sum of sine torques and its angular response is measured. The torque signals are generated using Matlab's *idinput* function, which allows a choice of the frequency interval, number of sine waves and overall amplitude using the following command.

$$[u,\ \text{freq}] = \text{idinput(N,'sine', } [w_{min}, w_{max}],\ [u_{min}, u_{max}],\ [\text{no. of sines, no. of trials}]) \tag{4.13}$$

where

$$\begin{aligned} u &= \text{signal generated} \\ \text{freq} &= \text{frequencies generated} \\ \text{N} &= \text{number of data points in } u \\ w_{min}, w_{max} &= \text{minimum and maximum frequencies as fractions of Nyquist frequency} \\ u_{min}, u_{max} &= \text{minimum and maximum amplitudes of signal generated} \\ \text{no. of trials} &= \text{number of trials tried to get the lowest amplitude signal} \end{aligned}$$

Based on the Matlab command in Eq. (4.13), the following torque containing 1000 sine waves from 1-500Hz was generated using a sampling frequency of 5kHz. The maximum allowed voltage range for the signal was $[-1, 1]$V.

$$[\text{u, freq}] = \text{idinput(N,'sine', [1/2500, 500/2500], [-1, 1], [1000,10])} \tag{4.14}$$

The motor shaft angle was measured using the optical encoder and angular velocity was numerically calculated to obtain the output. Matlab's $tfestimate$ function was used to estimate the transfer function from input to output as shown below.

$$[\text{Txy,F}] = \text{tfestimate(x,y,window,noverlap,nfft,}f_s) \tag{4.15}$$

where

x,y =input and output signals, respectively

window =window function to split x and y into sections

overlap =no. of samples to overlap windows

nfft =FFT length that determines frequencies for estimation of power spectral density, default value is maximum of 256 or power of 2 > length of x or y

f_s =sampling frequency

The effects of coulomb friction and constant offset were subtracted from the measured torque to obtain the input. Data was collected for about 8 seconds and the last 5 seconds of collected data was used to generate the input and output. Using the command in Eq. (4.15), a hanning window of 1 second and an overlap of 0.2 seconds, the transfer function (Txy) from input to output was obtained.

4.3.1 Motor Response

The motor governing equation is given by,

$$J_{11}\ddot{\theta}_{11} = \tau - b_1\dot{\theta}_{11} - c_1 S_f(\dot{\theta}_{11}) + d_1 \tag{4.16}$$

where θ_{11} is the motor shaft encoder measurement. Hence the transfer function from torque to motor angular velocity is obtained as follows:

$$\frac{\dot{\theta}_{11}}{\tau_c}(s) = \frac{1}{J_{11}s + b_1} \tag{4.17}$$

where $\tau_c = \tau - c_1 S_f(\dot{\theta}_{11}) + d_1$ is the drive motor torque compensated for coulomb friction and constant offset. Figure 4.17 shows the experimental frequency response of the motor only. The theoretical frequency response is simulated using the estimated parameters in Table 4.1 and the transfer function derived above. A good agreement is seen.

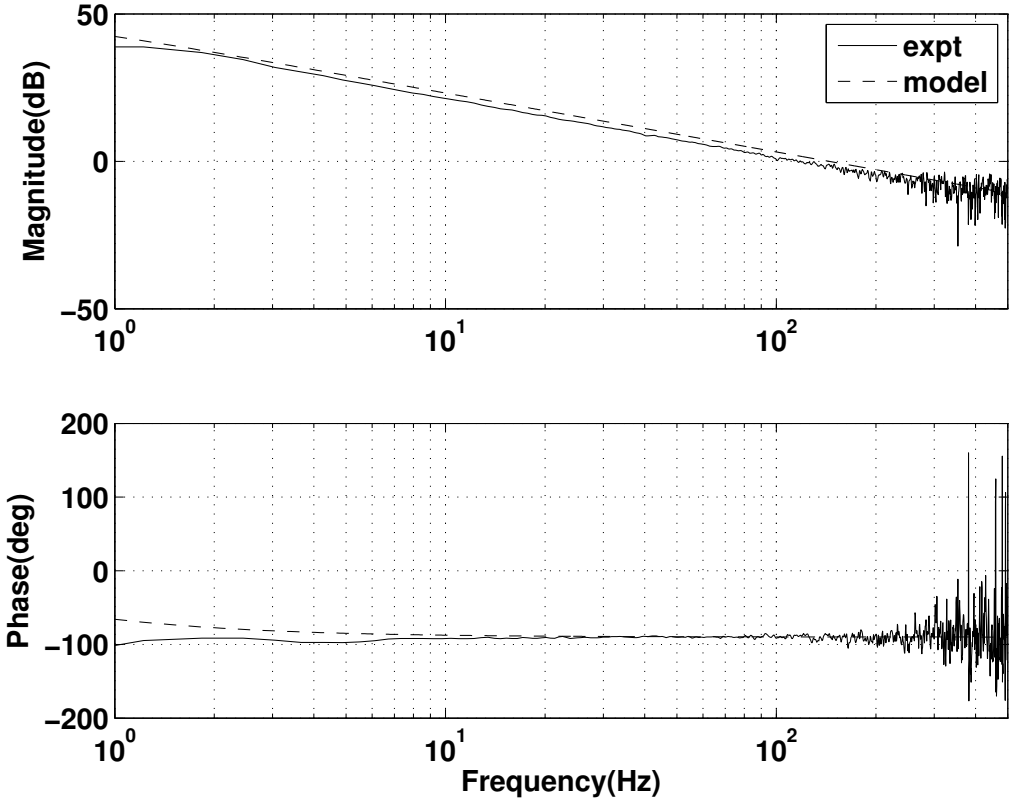

Figure 4.17. Motor frequency response.

4.3.2 Motor and Drive Pulley Response

Figure 4.19 shows the experimental frequency response of the motor coupled with the drive pulley. A mild resonance and anti-resonance pair is observed near 100Hz indicating that the motor-drive pulley coupling is not rigid. The theoretical frequency response is simulated using the estimated parameters in Table 4.1 and the transfer function derived below. In order to capture the flexible mode of the motor-drive pulley coupling, a spring damper model is used to approximate the coupling as shown in Figure 4.18.

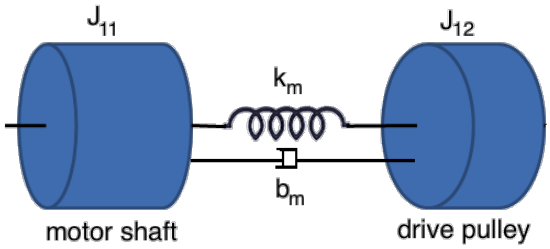

Figure 4.18. Motor-drive pulley coupling model.

The governing equations are given by,

$$J_{11}\ddot{\theta}_{11} = \tau - b_1\dot{\theta}_{11} - c_1 S_f(\dot{\theta}_{11}) + d_1 + k_m(\theta_{12} - \theta_{11}) - b_m(\dot{\theta}_{11} - \dot{\theta}_{12}) \tag{4.18a}$$

$$J_{12}\ddot{\theta}_{12} = k_m(\theta_{11} - \theta_{12}) - b_m(\dot{\theta}_{12} - \dot{\theta}_{11}) \tag{4.18b}$$

where θ_{11}, θ_{12} are motor shaft and drive pulley angular positions, respectively, as shown in Figure 4.18. Hence the transfer function from torque to motor shaft angular velocity is obtained as follows:

$$\begin{aligned}\frac{\dot{\theta}_{11}}{\tau_c}(s) &= \frac{(J_{12}s^2 + b_m s + k_m)s}{(J_{11}s^2 + (b_1 + b_m)s + k_m)(J_{12}s^2 + b_m s + k_m) - (k_m + b_m s)^2} \\ &= \frac{\frac{1}{J_{11}}s^2 + \frac{b_m}{J_{11}J_{12}}s + \frac{k_m}{J_{11}J_{12}}}{s^3 + b_m\left(\frac{1}{J_{11}} + \frac{1}{J_{12}}\right)s^2 + \left(\frac{k_m}{J_{11}} + \frac{k_m}{J_{12}} + \frac{b_1 b_m}{J_{11}J_{12}}\right)s + \frac{b_1 k_m}{J_{11}J_{12}}}\end{aligned} \tag{4.19}$$

Parameters $b_m = 0.075, k_m = 135$ were chosen to closely match the flexible mode in the experimental frequency response.

4.4 Current Amplifier Characteristics

As mentioned earlier, the system is controlled using a DS1103 dSpace controller board. Figure 4.20 shows a block diagram of the closed-loop system. The drive motor is operated in current control mode and receives its signal from the servoamplifier. When a required drive torque is computed, it is sent to the servoamplifier in the form of a voltage command from the dSpace controller board.

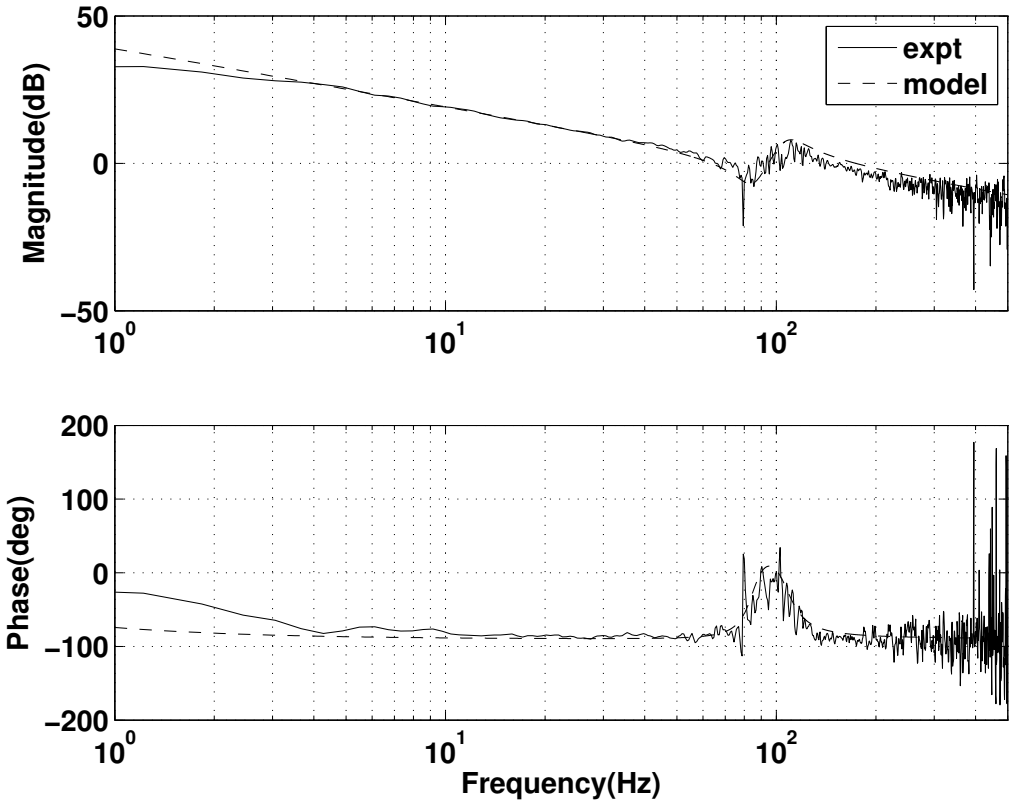

Figure 4.19. Motor-drive pulley frequency response.

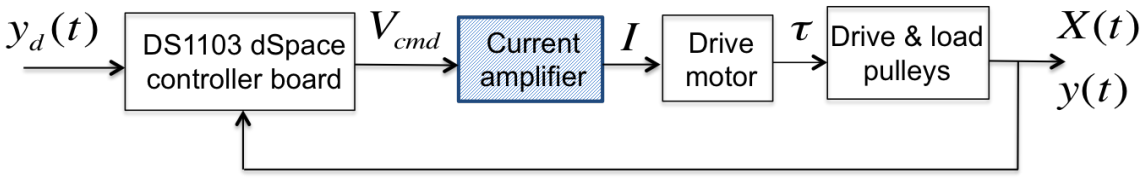

Figure 4.20. Block diagram of closed-loop system.

In order to calculate the voltage command for a known current or torque, the characteristics of the servoamplifier were measured using a frequency response experiment where a sum-of-sines voltage command was generated and the motor torque was

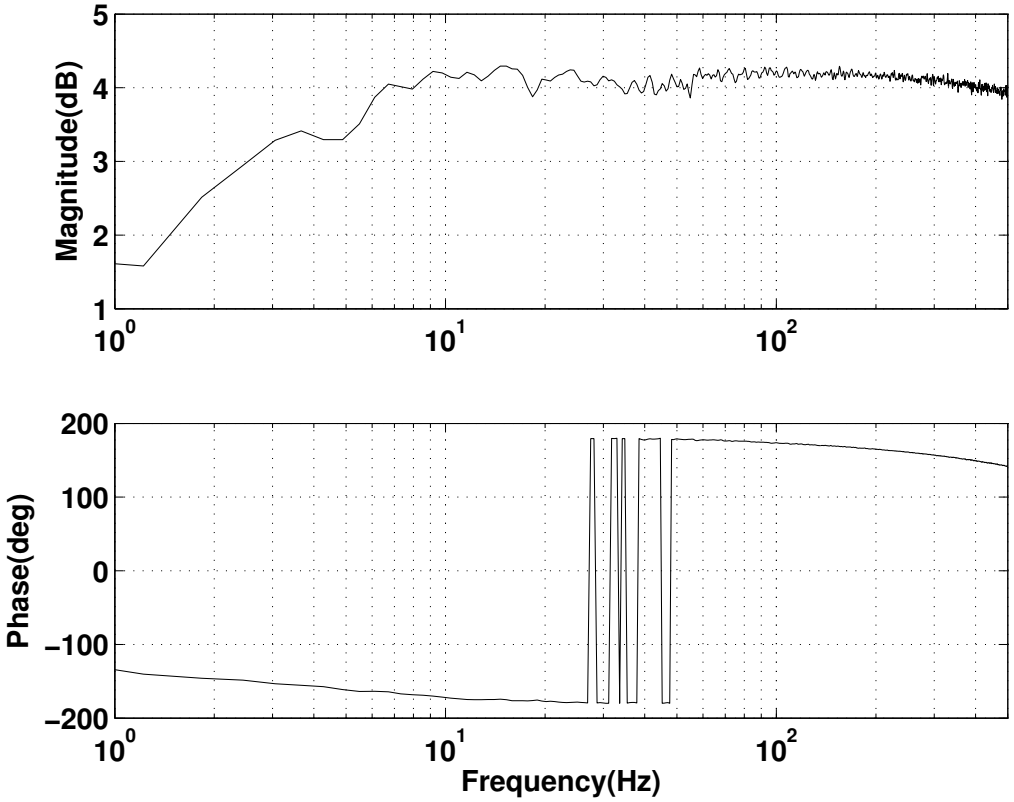

Figure 4.21. Frequency response of current amplifier $\frac{\tau}{V_{cmd}}$(s).

calculated from measured motor current and the torque constant in manufacturer specifications. The results are shown in Figure 4.21, which shows that the relationship between dSpace voltage command and motor current is essentially a constant gain of about 4.2dB. Hence the dSpace voltage command for a given motor torque is calculated as follows:

$$\begin{aligned} 4.2 =& 20 \log_{10} \left(\frac{\tau}{V_{cmd}} \right) \\ \frac{\tau}{V_{cmd}} =& 10^{\frac{4.2}{20}} = 1.6218 \\ V_{cmd} =& 0.6166\ \tau \end{aligned} \tag{4.20}$$

5. AUTOPARAMETRIC RESONANCE

The excitation of oscillations in an oscillatory system through the periodic variation of one of the system's oscillation parameters is known as parametric resonance. When a mechanical system consists of two or more coupled vibrating components, the vibration of one of the component subsystems may destabilize the motion of the other [36]. This destabilization effect is called autoparametric resonance. A classical example of such an autoparametric system is the elastic pendulum which consists of a spring fixed at one end and a mass at the other, as shown in Figure 5.1. Hence the spring may swing like a pendulum and oscillate at the same time. An interesting phenomenon occurs when the ratio of linear frequencies in the longitudinal and transverse directions is 2:1. When that happens, if we start with oscillation of the spring in the near vertical direction, this motion is unstable and energy is gradually transferred to the swinging motion and back [10], [37].

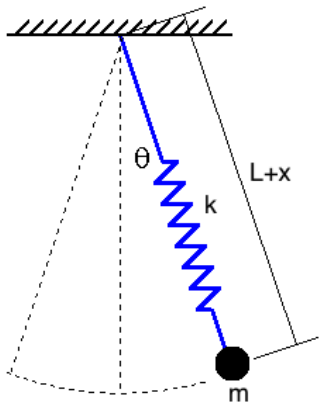

Figure 5.1. Spring pendulum.

In the case of motion transmission using flexible cables, the phenomenon of autoparametric or internal resonance requires careful consideration for the purposes of

stability as well as positioning accuracy. Cable vibrations generally occur in the longitudinal and mutually perpendicular transverse directions and are coupled nonlinearly. As in the case of the elastic pendulum, the condition for auto parametric resonance in cables is as follows:

$$\frac{\text{Fundamental longitudinal frequency}}{\text{Fundamental transverse frequency}} = 2 \tag{5.1}$$

As a result, solutions to the cable vibrations when written in the form of their fundamental modes are as follows:

$$u(x,t) = U(x)\cos 2\omega t \tag{5.2a}$$

$$v(x,t) = V(x)\sin \omega t \tag{5.2b}$$

$$w(x,t) = W(x)\sin \omega t \tag{5.2c}$$

where ω is the transverse mode frequency. Substituting the above equations in Eq. (2.21) for nonlinear tension, we get

$$\begin{aligned} T(x,t) &= T_0 + EA(1+\epsilon_0)(U'\cos 2\omega t + \frac{1}{4}(V'^2(1-\cos 2\omega t) + W'^2(1-\cos 2\omega t))) \\ &= T_0 + EA(1+\epsilon_0)(\frac{V'^2+W'^2}{4}) + EA(1+\epsilon_0)(U' - \frac{V'^2+W'^2}{4})\cos 2\omega t \end{aligned} \tag{5.3}$$

Therefore, if the cable-pulley system satisfies the condition in Eq. (5.1) where the fundamental longitudinal mode is twice the frequency of the fundamental transverse mode, we see that cable tension varies periodically at twice the transverse mode frequency. As a result, the behavior studied by Lord Rayleigh ([31], [32]) is intrinsic to cable vibrations where periodic variation of tension can be caused naturally by the vibration mode of the cable. For a cable fixed at both ends, as mentioned earlier, there is generally minimal coupling between longitudinal and transverse natural resonances due to the large gap between their fundamental frequencies. However, in the case of a cable-pulley system it has been shown that the system's fundamental longitudinal frequency may be greatly reduced due to the coupling between cables and high-inertia components such as the pulleys. Hence it becomes possible for longitudinal resonances to be strongly coupled with transverse resonances. In the following section, the design

conditions that lead to strong coupling between longitudinal and transverse vibrations in the cable-pulley system are explored.

5.1 Parametric Analysis

In order to predict when auto-parametric resonance occurs in the cable-pulley system, we take a closer look at the characteristic equation obtained from the determinant of the modal matrix in Eq. (3.13), which implicitly relates the fundamental longitudinal frequency of the system with all the physical parameters of the cable and pulleys. It is important to note that the fundamental transverse cable vibration frequency in the cable-pulley system is still given by Eq. (3.14b) as $f_{transverse} = \frac{c_w}{2L}$. Defining $\gamma = \frac{f_{transverse}}{\omega_{long}/2\pi} = \frac{\pi c_w}{\omega_{long} L}$ as the ratio of fundamental transverse and longitudinal frequencies, we get the following modified characteristic equation.

$$\frac{\pi c_w}{\gamma c_u}\chi_2 = \frac{\frac{-\pi c_w}{\gamma c_u}\chi_1 \cos(\frac{\pi c_w}{\gamma c_u}) - \sin(\frac{\pi c_w}{\gamma c_u})}{\frac{-\pi c_w}{\gamma c_u}\chi_1 \sin(\frac{\pi c_w}{\gamma c_u}) + \cos(\frac{\pi c_w}{\gamma c_u})} \tag{5.4}$$

where $\chi_1 = \frac{J_1}{2\rho r_1^2 L}$, $\chi_2 = \frac{J_2}{2\rho r_2^2 L}$ are essentially ratios of mass of each pulley to total cable mass. Each surface in Figure 5.2 represents the variation of transverse-to-longitudinal fundamental frequency ratio (γ) with pulley-to-cable mass ratios for different equilibrium cable tension (T_0). The plane parallel to the $\chi_1\chi_2$ plane represents a constant frequency ratio of $\gamma = \frac{1}{2}$ and hence its intersection with the surfaces gives a family of curves shown in Figure 5.3 that correspond to autoparametric resonance in cable-pulley systems. Since χ_1 and χ_2 are non-dimensional and depend only on physical properties and parameters of the cable and pulleys used, they may be used to represent different cable-pulley systems used in a variety of applications. For e.g., robotic hands, elevators and serpentine belt drive systems typically have lower pulley-to-cable mass ratios and higher cable tension. This analysis provides some insight into the choice of design parameters and their effects on natural frequencies and internal resonance, as cable-driven systems become more common in motion transmission applications.

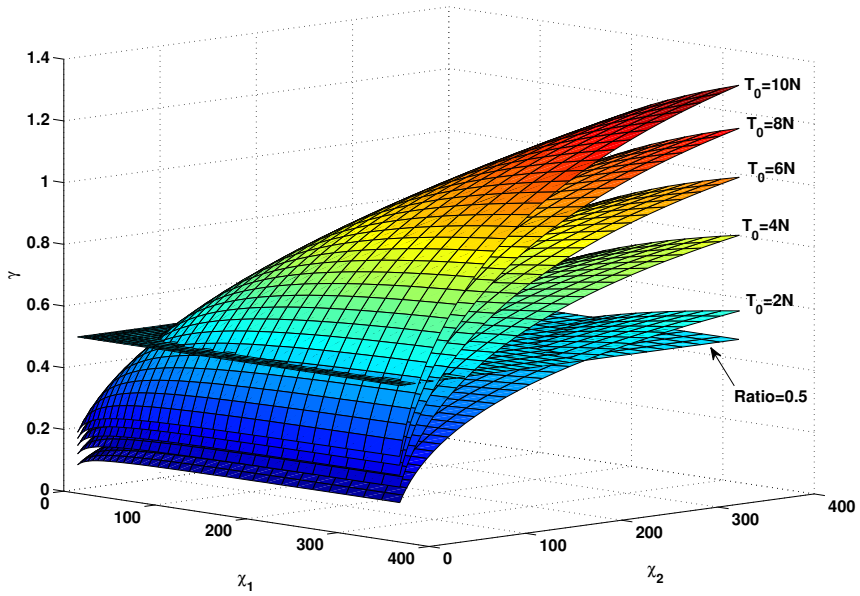

Figure 5.2. Variation of frequency ratio (γ) with mass ratios (χ_1 and χ_2) for different equilibrium tensions (T_0).

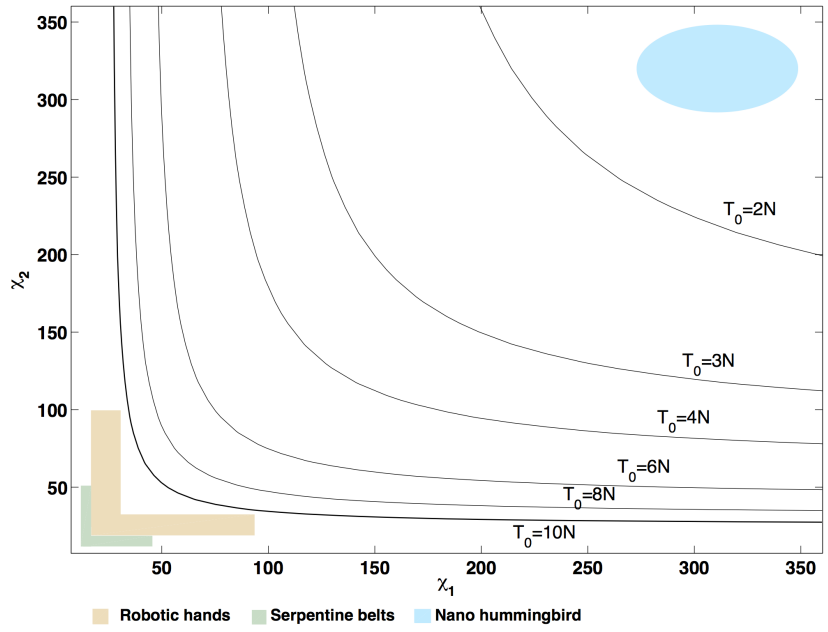

Figure 5.3. Contours of autoparametric resonance in a cable-pulley system.

5.2 Forced Response

Using the parameters of configuration 2 in Table 3.1 and the condition in Eq. (5.1), forced vibrations of the cable-pulley system were numerically simulated and verified experimentally. Only cable tension was changed to satisfy Eq. (5.1) and study the phenomenon of autoparametric resonance. The cable-pulley system was subject to an external oscillatory torque through the drive motor at the system's natural longitudinal frequency of 81.6Hz. Both simulation and experimental results are presented here.

5.2.1 Numerical Results

The numerical scheme discussed in Eqs. (2.32)-(2.39) was used to simulate the cable-pulley system. Zero initial conditions were used for pulley and cable velocities and pulley angle while a triangular profile was used for cable displacement. An external oscillatory torque $\tau = A \sin \omega t$ was added to the drive pulley dynamics, where A is the amplitude of the torque and ω is its angular frequency. Figure 5.4 shows oscillations of the load pulley and transverse vibrations of the cable span midpoint ($w_1(t, x = \frac{L_e}{2})$) during autoparametric resonance. A strong coupling between the rotational mode of the load pulley and transverse mode of the cable can be seen along with an exchange of energy as seen from the vibration amplitudes.

5.2.2 Experimental Results

As shown in the experimental setup in Figure 4.1, load pulley oscillations and cable tension are both measured using an optical encoder and compressive load cell in real time. A high-speed camera is installed at the cable midpoint and captures longitudinal and transverse cable vibrations at 400 frames/sec. The external torque is applied through the drive motor at the longitudinal natural frequency of 81.6Hz as cable tension is slowly increased from near zero. Figure 5.5 shows measured transverse ca-

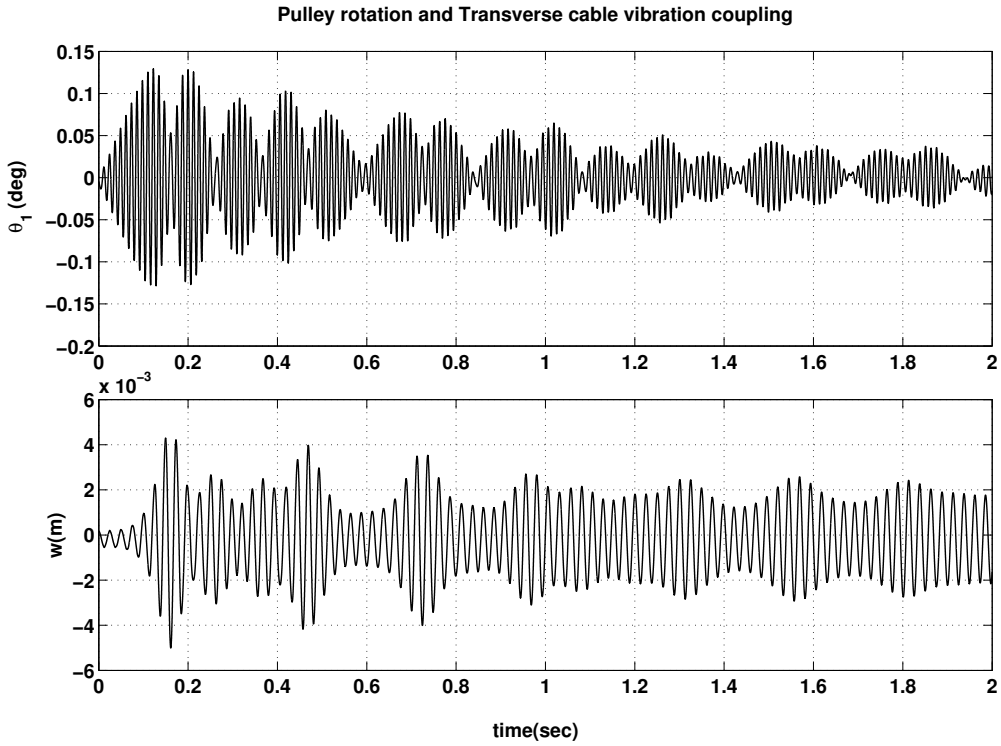

Figure 5.4. Simulated forced autoparametric resonance of pulley oscillations (top) and transverse cable midpoint vibrations (bottom).

ble midpoint vibrations as cable tension is slowly increased. Changing cable tension changes the frequency ratio (γ) by changing the cable's fundamental transverse frequency, while the fundamental longitudinal frequency remains relatively constant. As a result, the system is slowly moved from a detuned state to a tuned state where the frequency ratio condition in Eq. (5.1) is satisfied. The sudden increase in transverse cable vibrations is due to the onset of autoparametric resonance as γ approaches 0.5. Figure 5.6 shows experimentally recorded oscillations of the pulley and transverse vibrations of the cable midpoint during autoparametric resonance. Strong coupling between the rotational and transverse modes can be seen clearly leading to a growth of both vibration amplitudes. A kind of beats phenomenon is seen where energy is exchanged between the two modes.

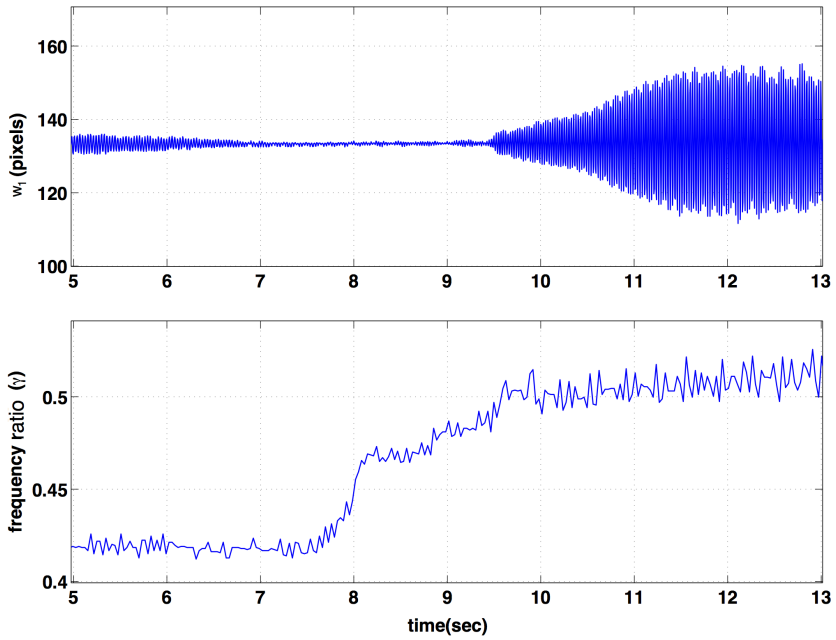

Figure 5.5. Response of transverse cable midpoint vibrations with changing γ.

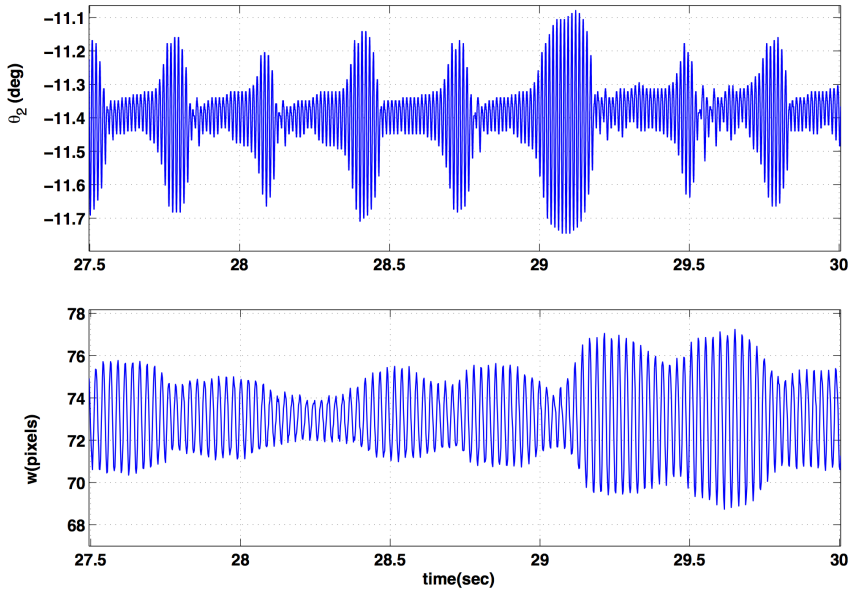

Figure 5.6. Experimentally recorded forced auto-parametric resonance of pulley oscillations (top) and transverse cable midpoint vibrations (bottom).

5.3 Free Response Experimental Results

The free response of the cable-pulley system in configuration 2 shown in Table 3.1 is studied during autoparametric resonance. Both cable spans were plucked at their midpoints. Load pulley oscillations were recorded using the optical encoder while the upper cable midpoint vibrations in the w_1 direction were captured using the high-speed camera at 400 frames/sec. Figure 5.7 shows the recorded transverse cable midpoint vibrations and pulley oscillations. Coupling between them can be seen over the first second where the amplitude of pulley oscillations increases at the same time the transverse cable vibrations reach their minimum and vice versa. The vibrations die out due to cable damping after the first second.

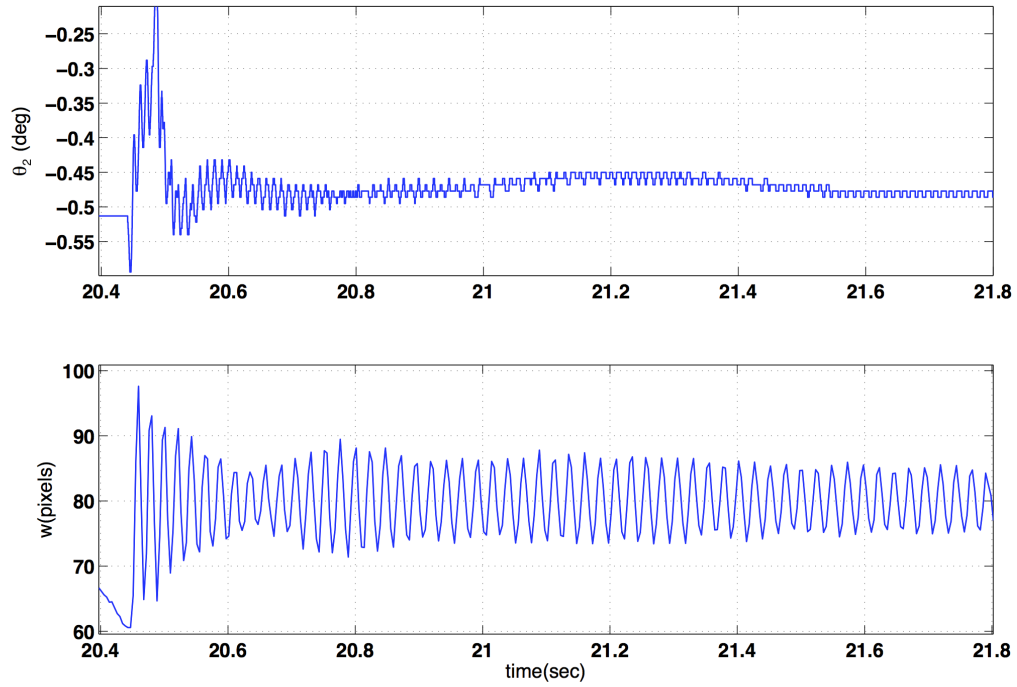

Figure 5.7. Experimentally recorded free oscillations of pulley (top) and transverse vibrations of cable midpoint (bottom) during autoparametric resonance.

6. CONTROL DESIGN

6.1 Trajectory Design

In this section, a 9^{th} order polynomial is used to design a pulse trajectory that rotates the load pulley back and forth between two angles. The trajectory is chosen to be feasible in terms of available motor speed and acceleration and smooth up to 4^{th} order to avoid jerk motions during the start and end of the motion. The rise portion of the trajectory is defined as follows:

$$y_{d1}(t) = \sum_{j=0}^{9} a_j t^j \tag{6.1}$$

Applying the following initial conditions,

$$y_{d1}(0) = 0 \tag{6.2a}$$

$$\dot{y}_{d1}(0) = 0 \tag{6.2b}$$

$$\ddot{y}_{d1}(0) = 0 \tag{6.2c}$$

$$\dddot{y}_{d1}(0) = 0 \tag{6.2d}$$

$$\ddddot{y}_{d1}(0) = 0 \tag{6.2e}$$

leads to $a_0 = a_1 = a_2 = a_3 = a_4 = 0$. Defining t_f to be the time taken to reach a final desired angle θ_f, we apply the following end conditions:

$$y_{d1}(t_f) = \theta_f = a_5 t_f^5 + a_6 t_f^6 + a_7 t_f^7 + a_8 t_f^8 + a_9 t f^9 \tag{6.3a}$$

$$\dot{y}_{d1}(t_f) = 0 = 5a_5 t_f^4 + 6a_6 t_f^5 + 7a_7 t_f^6 + 8a_8 t_f^7 + 9a_9 t_f^8 \tag{6.3b}$$

$$\ddot{y}_{d1}(t_f) = 0 = 20a_5 t_f^3 + 30a_6 t_f^4 + 42a_7 t_f^5 + 56a_8 t_f^6 + 72a_9 t_f^7 \tag{6.3c}$$

$$\dddot{y}_{d1}(t_f) = 0 = 60a_5 t_f^2 + 120a_6 t_f^3 + 210a_7 t_f^4 + 336a_8 t_f^5 + 504a_9 t_f^6 \tag{6.3d}$$

$$\ddddot{y}_{d1}(t_f) = 0 = 120a_5 t_f + 360a_6 t_f^2 + 840a_7 t_f^3 + 1680a_8 t_f^4 + 3024a_9 t_f^5 \tag{6.3e}$$

The above linear set of equations can be solved to obtain $a_j,\ j = 5, ...9$ for a given θ_f and t_f. By adjusting t_f, the trajectory can be made faster or slower keeping in mind the available control effort. The reverse trajectory to return to zero angle is defined by,

$$y_{d2}(t) = \sum_{j=0}^{9} b_j t^j \tag{6.4}$$

Using the following initial conditions,

$$y_{d2}(0) = \theta_f \tag{6.5a}$$

$$\dot{y}_{d2}(0) = 0 \tag{6.5b}$$

$$\ddot{y}_{d2}(0) = 0 \tag{6.5c}$$

$$\dddot{y}_{d2}(0) = 0 \tag{6.5d}$$

$$\ddddot{y}_{d2}(0) = 0 \tag{6.5e}$$

we get $b_0 = \theta_f, b_1 = b_2 = b_3 = b_4 = 0$. Hence,

$$y_{d2}(t) = \theta_f + \sum_{j=5}^{9} b_j t^j \tag{6.6}$$

Applying the following end conditions,

$$y_{d2}(t_f) = 0 = \theta_f + b_5 t_f^5 + b_6 t_f^6 + b_7 t_f^7 + b_8 t_f^8 + b_9 t_f^9 \tag{6.7a}$$

$$\dot{y}_{d2}(t_f) = 0 = 5b_5 t_f^4 + 6b_6 t_f^5 + 7b_7 t_f^6 + 8b_8 t_f^7 + 9b_9 t_f^8 \tag{6.7b}$$

$$\ddot{y}_{d2}(t_f) = 0 = 20b_5 t_f^3 + 30b_6 t_f^4 + 42b_7 t_f^5 + 56b_8 t_f^6 + 72b_9 t_f^7 \tag{6.7c}$$

$$\dddot{y}_{d2}(t_f) = 0 = 60b_5 t_f^2 + 120b_6 t_f^3 + 210b_7 t_f^4 + 336b_8 t_f^5 + 504b_9 t_f^6 \tag{6.7d}$$

$$\ddddot{y}_{d2}(t_f) = 0 = 120b_5 t_f + 360b_6 t_f^2 + 840b_7 t_f^3 + 1680b_8 t_f^4 + 3024b_9 t_f^5 \tag{6.7e}$$

Hence the reverse trajectory can be obtained by solving the above linear set of equations. A single pulse can then be obtained by combining y_{d1} and y_{d2} as follows:

$$y_d(t) = \begin{cases} y_{d1}(t) & \text{for } 0 < t < t_f \\ y_{d2}(t - t_f - \Delta t) & \text{for } t_f + \Delta t < t < 2t_f + \Delta t \end{cases} \tag{6.8}$$

where Δt is a time span for which the load pulley is stationary between forward and revere trajectories. The resulting pulse is shown in Figure 6.1. In the following section, the design and performance of control techniques applied to the cable-pulley system are examined.

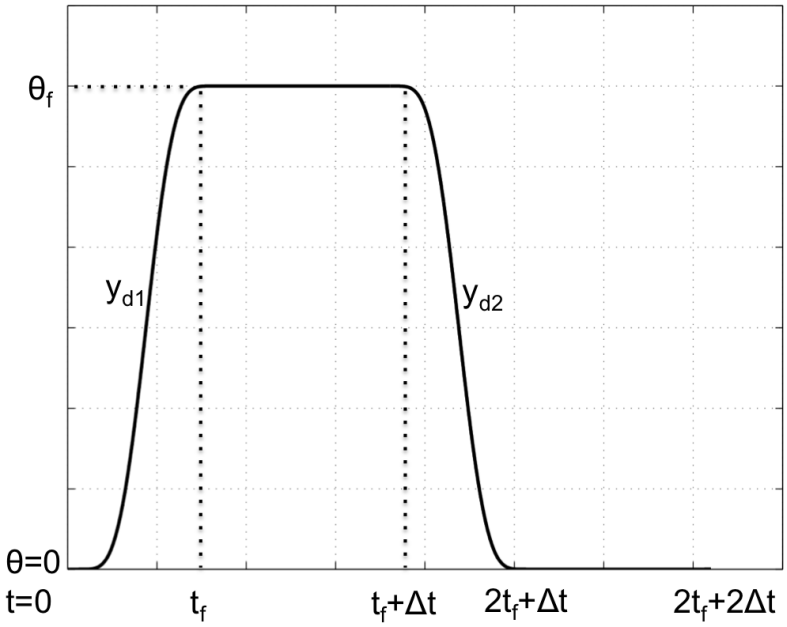

Figure 6.1. Single pulse using 9^{th} order polynomial.

6.2 Reduced-Order System Models

In this section, reduced-order models of the cable-pulley system are presented in order to simply the control design process used for position tracking. Since it has been shown through modal analysis and frequency response of the overall system that the flexible modes are due to the fundamental longitudinal mode of the cable and the flexible motor-drive pulley joint, four possible models of the system are discussed.

6.2.1 Model 1: Rigid Motor Joint and Rigid Cable

The simplest model where both motor joint and cables are assumed to be rigid, is presented. The load pulley angle is constrained to be equal to the drive pulley angle and motor shaft angle, i.e. $\theta_2 = \theta_1$. No distinction is made between the three angles and the different inertias (J_{11}, J_{12}, J_2) are combined into one. Using Figure 6.2 as reference, the dynamics of the system is as follows:

$$\begin{aligned}(J_1 + J_2)\ddot{\theta}_1 =& \tau - b_1\dot{\theta}_1 - c_1 S(\dot{\theta}_1) + d(t) \\ =& \tau - b_1\dot{\theta}_1 - c_1 S(\dot{\theta}_1) + d_0 + \tilde{d}(t)\end{aligned} \tag{6.9}$$

6.2.2 Model 2: Flexible Motor Joint and Rigid Cable

In this model, the motor joint flexibility is modeled and the cables are assumed to be rigid as is done commonly in literature. Hence the load pulley angle is constrained to be equal to the drive pulley angle, i.e. $\theta_2 = \theta_{12}$. Load pulley inertia (J_2) and drive pulley inertias (J_{12}) are combined into one. Based on the variables defined in Figure 6.4, the dynamics of the system is defined as follows:

$$J_{11}\ddot{\theta}_{11} = \tau - b_1\dot{\theta}_{11} - c_1 S(\dot{\theta}_{11}) + d_0 + \tilde{d}(t) + k_m(\theta_{12} - \theta_{11}) - b_m(\dot{\theta}_{11} - \dot{\theta}_{12}) \tag{6.10a}$$

$$(J_2 + J_{12})\ddot{\theta}_{12} = k_m(\theta_{11} - \theta_{12}) - b_m(\dot{\theta}_{12} - \dot{\theta}_{11}) \tag{6.10b}$$

6.2.3 Model 3: Rigid Motor Joint and Flexible Cable

Based on modal analysis of the system and experimental verification, it was shown that the fundamental longitudinal frequency of the cable-pulley system is greatly reduced, due to coupling between the flexible cables and high-inertia components i.e., the two pulleys. The normalized fundamental mode shapes of the upper and lower cable spans calculated as solutions to the eigenvalue problem and shown earlier in

Figures 3.3 and 3.4 are consistent with an axial spring-like behavior of the cables. These results strongly suggest the validity of an axial-spring damper approximation of the cables. It has also been shown that there is a large frequency gap between the fundamental mode of the cable-pulley system and the next higher mode. Hence, a lumped parameter model of the cable-pulley system is presented where only the rigid body mode and fundamental longitudinal vibration mode of the system are considered. The cables are replaced by spring-dampers with spring constant k and damping coefficient b_c while the motor-drive pulley joint is assumed to be rigid. A schematic of the system considered is shown in Figure 6.2. In the dynamic equations of the system, without loss of generality, load pulley damping and friction are neglected since they were found to be negligible in the load pulley setup unlike the drive pulley setup.

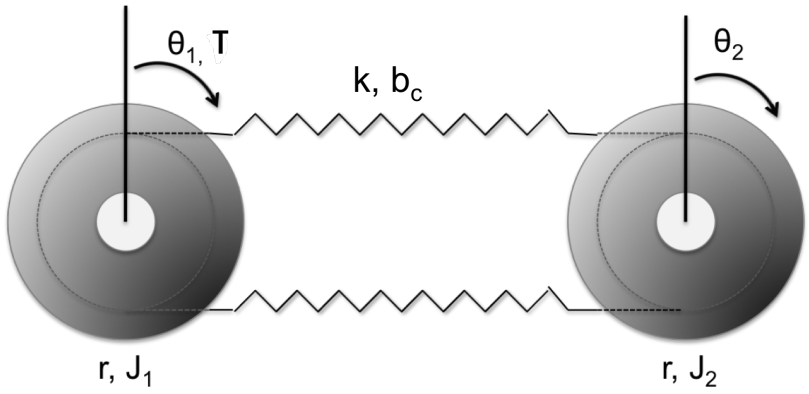

Figure 6.2. Cable-pulley system with cables approximated by axial spring-dampers.

The dynamic equations of the setup in Figure 6.2 are as follows:

$$\begin{aligned} J_1\ddot{\theta}_1 =& \tau - 2kr(r\theta_1 - r\theta_2) - b_1\dot{\theta}_1 - c_1 S(\dot{\theta}_1) - 2b_c r(\dot{\theta}_1 - \dot{\theta}_2) + d(t) \\ =& \tau - 2kr^2(\theta_1 - \theta_2) - b_1\dot{\theta}_1 - c_1 S(\dot{\theta}_1) - 2b_c r(\dot{\theta}_1 - \dot{\theta}_2) + d_0 + \tilde{d}(t) \qquad (6.11a) \\ J_2\ddot{\theta}_2 =& 2kr(r\theta_1 - r\theta_2) - 2b_c r(\dot{\theta}_2 - \dot{\theta}_1) \qquad (6.11b) \end{aligned}$$

where r is the radius of both pulleys and τ is the control torque from the drive motor. b_1, c_1 are coefficients of viscous and coulomb friction respectively of the drive motor

shaft and $S(\bullet)$ is the usual signum function. $d(t)$ is the lumped error from modeling inaccuracies and uncertainties such as disturbances and neglected higher modes. d_0 is the nominal constant part and $\tilde{d}(t)$ is the time varying part of $d(t)$. Based on the dynamics in Eq. (6.11), the following transfer function can be obtained.

$$\frac{\dot{\theta}_1}{\tau_c}(s) = \frac{\frac{1}{J_1}\left(s^2 + \frac{2b_c r}{J_2}s + \frac{2kr^2}{J_2}\right)}{s^3 + \left(\frac{b_1+2b_c r}{J_1} + \frac{2b_c r}{J_2}\right)s^2 + \left(\frac{2kr^2}{J_1} + \frac{2kr^2}{J_2} + \frac{2b_1 b_c r}{J_1 J_2}\right)s + \frac{2kb_1 r^2}{J_1 J_2}} \tag{6.12}$$

where $\tau_c(s)$ is the Laplace transform of $\tau_c = \tau - c_1 S(\dot{\theta}_1) + d_0$, the net driving torque after coulomb friction and offset compensation.

Results from experiments on the systems's frequency response are shown in Figure 6.3, which compares the experimental and theoretical frequency responses of the system from τ_c to motor angular velocity. The physical parameters of the system are listed in Table 6.1. The lowest natural frequency is seen to be around 7Hz and is caused by the spring-like behavior of the cable spans, leading to clearly visible resonance and anti-resonance modes. A higher-order flexible mode can also be seen around 120Hz. This is caused by the motor-drive pulley coupling and not a higher-order cable mode, based on the larger frequency gap in the system's longitudinal modes. The theoretical frequency response in Figure 6.3 is obtained from the transfer function in Eq. (6.12). Spring constant (k) and damping coefficient (b_c) values were chosen to match experimental observation.

6.2.4 Model 4: Flexible Motor Joint and Flexible Cable

A lumped parameter model of the cable-pulley system is presented where the flexibility of the motor-drive pulley joint is included along with cable flexibility. A schematic representation of the system is shown in Figure 6.4. $\theta_{11}, \theta_{12}, \theta_2$ are the angular rotations of the motor shaft, drive pulley and load pulley, respectively. J_{11}, J_{12}, J_2 are their corresponding rotational inertias.

Table 6.1. Physical parameters of cable-pulley system.

	Configuration 3
Cable material	nylon
J_1	0.001742 kgm^2
J_{11}	0.0011 kgm^2
J_{12}	0.000642 kgm^2
J_2	0.00235 kgm^2
r_1	4 cm
r_2	4 cm
E	3 Gpa
A	1.46×10^{-7} m^2
ρ	1.68×10^{-4} kg/m
L	1 m
T_0	7 N

The dynamics of the 3-mass-spring-damper system in Figure 6.4 is as follows:

$$J_{11}\ddot{\theta}_{11} = \tau - b_1\dot{\theta}_{11} - c_1 S(\dot{\theta}_{11}) + d_0 + \tilde{d}(t) + k_m(\theta_{12} - \theta_{11}) - b_m(\dot{\theta}_{11} - \dot{\theta}_{12}) \quad (6.13a)$$

$$J_{12}\ddot{\theta}_{12} = k_m(\theta_{11} - \theta_{12}) + 2kr^2(\theta_2 - \theta_{12}) - 2b_c r(\dot{\theta}_{12} - \dot{\theta}_2) - b_m(\dot{\theta}_{12} - \dot{\theta}_{11}) \quad (6.13b)$$

$$J_2\ddot{\theta}_2 = 2kr^2(\theta_{12} - \theta_2) - 2b_c r(\dot{\theta}_2 - \dot{\theta}_{12}) \quad (6.13c)$$

where k_m, b_m are spring constant and damping coefficient, respectively, of the motor-drive pulley joint. As in the case of Eq. (6.12), the transfer function from motor torque to motor shaft angular velocity is obtained as follows:

$$G_1 = \frac{\theta_{12}}{\theta_{11}}(s) = \frac{\frac{b_m}{J_{12}}(s + \frac{b_m}{k_m})(s^2 + \frac{2b_c r}{J_2}s + \frac{2kr^2}{J_2})}{s^4 + (\frac{2b_c r}{J_2} + \frac{b_m}{J_{12}} + \frac{2b_c r}{J_{12}})s^3 + (\frac{2kr^2}{J_2} + \frac{2b_c b_m r}{J_{12}J_2} + \frac{2kr^2}{J_{12}})s^2 + \frac{2kr^2 b_m}{J_{12}J_2}s}$$

$$\frac{\dot{\theta}_{11}}{\tau_c}(s) = \frac{\frac{s}{J_{11}}}{s^2 + \frac{b_1 + b_m}{J_{11}}s + \frac{k_m}{J_{11}} - G_1 b_m(s + \frac{k_m}{b_m})} \quad (6.14)$$

The theoretical frequency response from Eq. (6.14) can also be seen in Figure 6.3. k_m, b_m values are again chosen to match experimental observation. The spring con-

Table 6.2. Spring-damper coefficients from reduced-order model.

$k(N/m)$	$b_c(Ns/rad)$	$k_m(Nm/rad)$	$b_m(Nms/rad)$
850	0.18	135	0.075

stant and damping coefficient values are listed in Table 6.2. The results in Figure 6.3 further validate the spring-damper approximation of the cable spans and the motor joint.

In the following sections, adaptive robust controllers are designed based on the above four models of the cable-pulley system. Output position tracking performance is discussed in each case based on the fidelity of the model and its ability to capture key flexible modes.

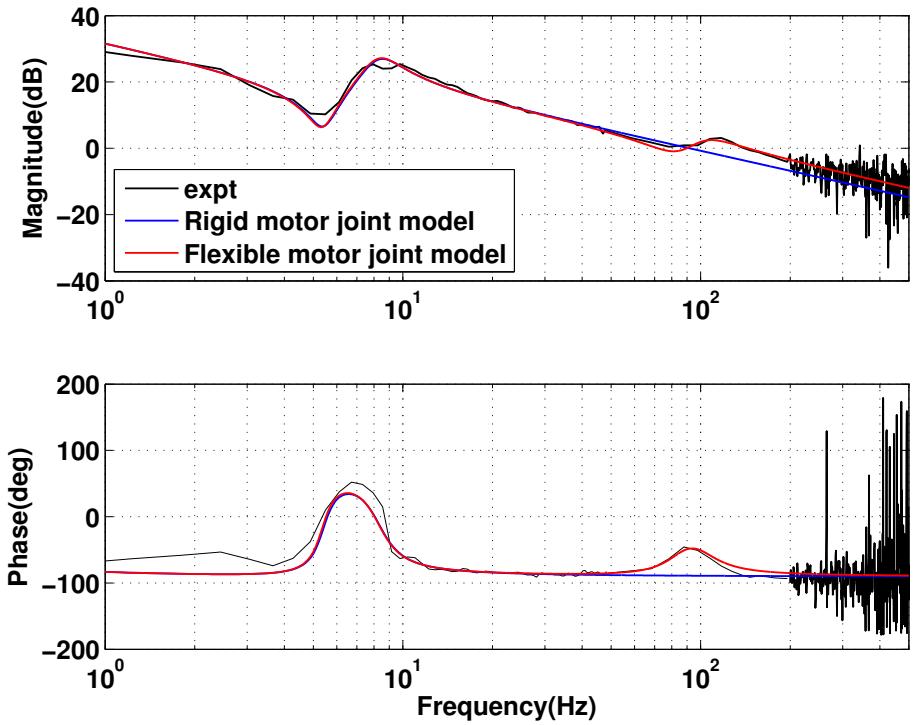

Figure 6.3. Frequency response from τ_c to motor shaft angular velocity.

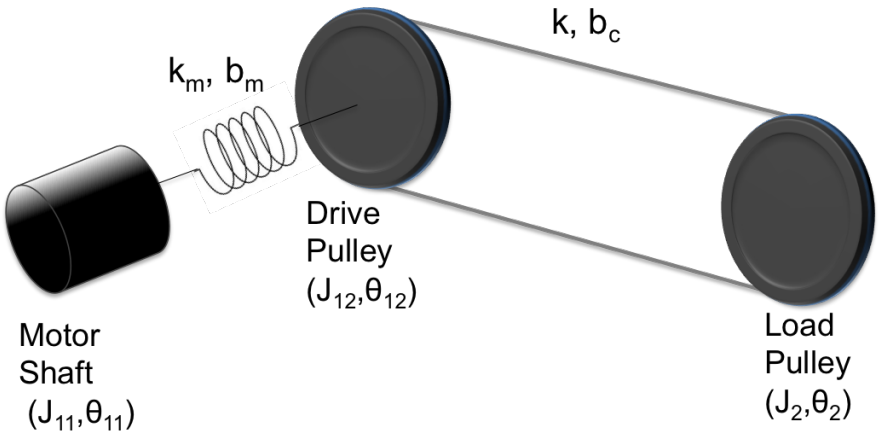

Figure 6.4. Cable-pulley system with flexible motor joint.

6.3 DARC with Matched Uncertainty: Model 1

Based on the dynamics in Eq. (6.9), the following state variables are defined:

$$x_1 = \theta_1$$
$$x_2 = \dot{\theta}_1$$

The system dynamics can be expressed as,

$$\dot{x}_1 = x_2 \tag{6.15a}$$
$$p_2\dot{x}_2 = u - p_3 x_2 - p_4 S_f(x_2) + p_5 + \tilde{d}(t) \tag{6.15b}$$
$$y = x_1 \tag{6.15c}$$

where $p_2 = J_1 + J_2, p_3 = b_1, p_4 = c_1, p_5 = d_0$ are constant model parameters that need to be estimated. $S_f(\bullet) = tanh(0.5\bullet)$ is a smooth approximation to the signum function and $u = \tau$ is the control input/drive torque.

The following nomenclature is used from here on. At any give time t, $\hat{p}_i$ denotes the estimate of p_i and $\tilde{p}_i$ denotes the estimation error of p_i given by $\tilde{p}_i = \hat{p}_i - p_i$. $p_{i,max}$ and $p_{i,min}$ represent the maximum and minimum values of p_i, respectively. Based on practical knowledge of the system, the following assumptions are made about parametric uncertainties and uncertain nonlinearities.

Assumption 1 : The unknown parameter vector p lies within a known bounded convex set Ω_p. Without loss of generality, it is assumed that $p_{i,min} \leq p_i \leq p_{i,max}$ where $p_{i,min}$ and $p_{i,max}$ are known constants.

Assumption 2 : The uncertain nonlinearity is bounded, i.e., $\tilde{d}(t) \in \Omega_d = d : |d| \leq \delta$, where $\delta(t)$ is a known bounded function.

Let $y_d(t)$ be the reference angular trajectory, assumed to be bounded with bounded derivatives up to at least fourth order. Our control objective is to synthesize a control input $u(t)$ such that the output $y = \theta_1(t)$ tracks $y_d(t)$ as closely as possible. The following error variables are defined:

$$z_1 = x_1 - y_d \tag{6.16a}$$

$$z_2 = \dot{z}_1 = x_2 - \dot{y}_d \tag{6.16b}$$

A sliding surface is defined as follows:

$$\sigma(s) = (s + \lambda) z_1(s) \tag{6.17}$$

Hence,

$$\sigma = \dot{z}_1 + \lambda z_1 = z_2 + \lambda z_1 \tag{6.18}$$

Taking the derivative of σ and using Eq. (6.15),

$$\begin{aligned} p_2 \dot{\sigma} =& p_2 \dot{z}_2 + p_2 \lambda z_2 \\ =& p_2 \dot{x}_2 - p_2 (\ddot{y}_d - \lambda z_2) \\ =& u - p_3 x_2 - p_4 S_f(x_2) + p_5 + \tilde{d}(t) - p_2 z_{eq} \\ =& u + \varphi^T p + \tilde{d}(t) \end{aligned} \tag{6.19}$$

where $z_{eq} = \ddot{y}_d - \lambda z_2$ and $\varphi^T = [-z_{eq},\ -x_2,\ -S_f(x_2),\ 1]$ and $p = [p_2,\ p_3,\ p_4,\ p_5]^T$. Hence the control law u is designed as follows.

$$u = u_a + u_{s1} + u_{s2}$$

$$u_a = -\varphi^T \hat{p} \tag{6.20a}$$

$$u_{s1} = -k_\sigma \sigma \tag{6.20b}$$

$$u_{s2} = -k_{\sigma s} \sigma \tag{6.20c}$$

where k_σ is a positive feedback gain and $k_{\sigma s}$ is a positive nonlinear gain chosen large enough such that the following two conditions are satisfied:

$$Condition\ 1: \ \sigma(u_{s2} - \varphi^T \tilde{p} + \tilde{d}(t)) \leq \epsilon \tag{6.21a}$$

$$Condition\ 2: \ \sigma u_{s2} \leq 0 \tag{6.21b}$$

Condition 1 ensures that u_{s2} can attenuate uncertainties due to parametric uncertainty and uncertain nonlinearity to a constant $\epsilon > 0$ specified by the designer. Condition 2 guarantees that u_{s2} is dissipative in nature so as to not interfere with the functioning of the adaptation and to guarantee asymptotic tracking in the presence of parametric uncertainty alone. An example for choice of u_{s2} is as follows:

$$u_{s2} = -\frac{\sigma}{4\epsilon}[\|p_{max} - p_{min}\|^2 \|\varphi\|^2 + \delta^2] \tag{6.22}$$

With $K_\sigma = k_\sigma + k_{\sigma s}$, the controller results in the following sliding surface error dynamics,

$$\mu\dot{\sigma} + K_\sigma \sigma = -\varphi^T \tilde{p} + \tilde{d}(t) \tag{6.23}$$

where $\mu = p_2$.

6.3.1 Discontinuous Projection Type Adaptation Law

A key element of DARC design is to use practical *a priori* knowledge of estimated parameters to construct the projection type adaption law for a controlled learning process. The following projection mapping is used to always keep parameter estimates within the known bounded set Ω_p.

$$Proj_{p_i}(\bullet_i) = \begin{cases} 0 & \text{if } \hat{p}_i = p_{i,max} \text{ and } \bullet_i > 0 \\ 0 & \text{if } \hat{p}_i = p_{i,min} \text{ and } \bullet_i < 0 \\ \bullet_i & \text{otherwise} \end{cases} \tag{6.24}$$

The above parameter projection leads to the following desirable properties:

$P1$. The parameter estimates are always within the known bounded set Ω_p, i.e., $\hat{p}(t) \in \Omega_p,\ \forall t$. If $\hat{p}_i(0) \in \Omega_p$,

$$p_{i,min} \leq \hat{p}_i(t) \leq p_{i,max}, \quad i = 2, ..., 5,\ \forall t \tag{6.25}$$

$P2$. For any adaptation function τ and positive definite adaptation gain matrix Γ,

$$\tilde{p}^T(\Gamma^{-1} Proj_p(\Gamma\tau) - \tau) \leq 0 \tag{6.26}$$

6.3.2 Performance of DARC

Theorem : Based on Assumptions 1 and 2, using the DARC control law defined in Eq. (6.20) and the rate limited adaptation law structure in Eq. (6.24), all signals in the closed-loop system are bounded and the following conditions hold:

(A) The output tracking error has a guaranteed transient performance and a guaranteed final tracking accuracy. Furthermore, the non-negative function $V = \frac{\mu}{2}\sigma^2$ is bounded above by

$$V \leq e^{-\lambda t} V(0) + \frac{\epsilon}{\lambda}(1 - e^{-\lambda t}) \tag{6.27}$$

where $\lambda = \frac{2k_\sigma}{\mu}$.

(B) In the presence of parametric uncertainties alone (i.e. $\tilde{d} = 0$), the designed control law ensures asymptotic tracking, i.e. $z_1 \to 0$ as $t \to \infty$.

Proof of (A): Differentiating V and using Eq. (6.23),

$$\begin{aligned} \dot{V} =& \sigma\mu\dot{\sigma} \\ =& \sigma(u_{s2} - \varphi^T\tilde{p} + \tilde{d} - k_\sigma\sigma) \\ =& -k_\sigma\sigma^2 + \sigma(u_{s2} - \varphi^T\tilde{p} + \tilde{d}) \end{aligned} \tag{6.28}$$

Applying Condition 1 from Eq. (6.21a),

$$\begin{aligned} \dot{V} \leq& -k_\sigma\sigma^2 + \epsilon \\ =& -\lambda V + \epsilon \end{aligned} \tag{6.29}$$

where $\lambda = \frac{2k_\sigma}{\mu}$.

Proof of (B): We define a function with a slight modification to the previous one as follows:

$$\begin{aligned} V_n =& V + \frac{1}{2}\tilde{p}^T\Gamma^{-1}\tilde{p} \\ \dot{V}_n =& -k_\sigma\sigma^2 + \sigma u_{s2} + \tilde{p}^T(\Gamma^{-1}\dot{\hat{p}} - \varphi\sigma) \end{aligned} \tag{6.30}$$

Using the parameter update law $\dot{\hat{p}} = Proj_p(\Gamma\varphi\sigma)$, Property 2 of the projection law in Eq. (6.26) and Condition 2 in Eq. (6.21b),

$$\begin{aligned} \dot{V}_n &\leq -k_\sigma\sigma^2 + \tilde{p}^T(\Gamma^{-1}Proj_p(\Gamma\varphi\sigma) - \varphi\sigma) \\ &\leq -k_\sigma\sigma^2 \end{aligned} \tag{6.31}$$

Hence σ is bounded. From Eq. (6.23), it can be checked that $\dot{\sigma}$ is bounded and continuous. Using Barbalat's Lemma, we obtain $\sigma \to 0$ as $t \to \infty$ or $z_1 \to 0$ as $t \to \infty$.

6.3.3 Adaptation Gain Tuning

Consider the σ dynamics in (6.23),

$$\dot{\sigma} + \frac{K_\sigma}{\mu}\sigma = -\frac{1}{\mu}(\varphi^T\tilde{p} - \tilde{d}(t)) \tag{6.32}$$

The parameter update law given by $\dot{\hat{p}} = \Gamma\varphi\sigma$ results in,

$$\begin{aligned} \hat{p}(t) =& \hat{p}(0) + \int_0^t \Gamma\varphi\sigma d\tau \\ \approx& \hat{p}(0) + \Gamma\varphi_d\int_0^t \sigma d\tau \end{aligned} \tag{6.33}$$

Substituting the above in Eq. (6.32),

$$\begin{aligned} \dot{\sigma} + k_m\sigma =& -\frac{1}{\mu}\left(\varphi^T(\hat{p}(0) - p) + \varphi^T\int_0^t \Gamma\varphi\sigma d\tau - \tilde{d}(t)\right) \\ \dot{\sigma} + k_m\sigma + \frac{\varphi_d^T\Gamma\varphi_d}{\mu}\int_0^t \sigma d\tau =& -\frac{1}{\mu}(\varphi^T\tilde{p}(0) - \tilde{d}(t)) \end{aligned} \tag{6.34}$$

Eq. (6.34) represents the second-order dynamics of σ where $k_m = \frac{K_\sigma}{\mu}$ and the assumption $\varphi(x) \approx \varphi_d(t) = \varphi(x_d(t))$ has been made. This is because for a large k_m the σ dynamics is fast, σ is normally small and $x \approx x_d$ in ARC. Since a very small Γ makes the parameter adaptation response too slow to be useful and a large Γ can lead to a very lightly damped second-order system with excess oscillating transient response, Γ is chosen as follows:

$$\frac{\varphi_d^T \Gamma \varphi_d}{\mu} = \omega_d^2 = \frac{k_m^2}{4\zeta_d^2} \tag{6.35}$$

Γ is chosen as,

$$\Gamma = \gamma W_p^2, \quad W_p = \ diag(p_{max} - p_{min}) \tag{6.36}$$

where

$$\gamma = \frac{k_m^2}{4\zeta_d^2 s_{\bar{p}}}, \quad s_{\bar{p}} = sup\left(\frac{\varphi_d^T W_p^2 \varphi_d}{\mu}\right) \tag{6.37}$$

6.3.4 Experimental Results

Figure 6.5 shows the load pulley output under the DARC law defined in Eq. (6.20). The vibrations in the output can be seen at different values of closed-loop bandwidth, λ. The frequency spectrum of the output in Figure 6.6 shows that the frequency of vibrations is the same as the dominant mode of the cable-pulley system caused by cable flexibility, confirming the need to model this mode of the system. As λ is increased, the higher-order flexible mode of the system due to the motor joint is also excited. This is evident from the drive pulley angle seen in Figure 6.7 and its frequency spectrum in Figure 6.8. These results are consistent with ignoring both flexible modes in the system model, which leads to their excitement as the closed-loop bandwidth is increased.

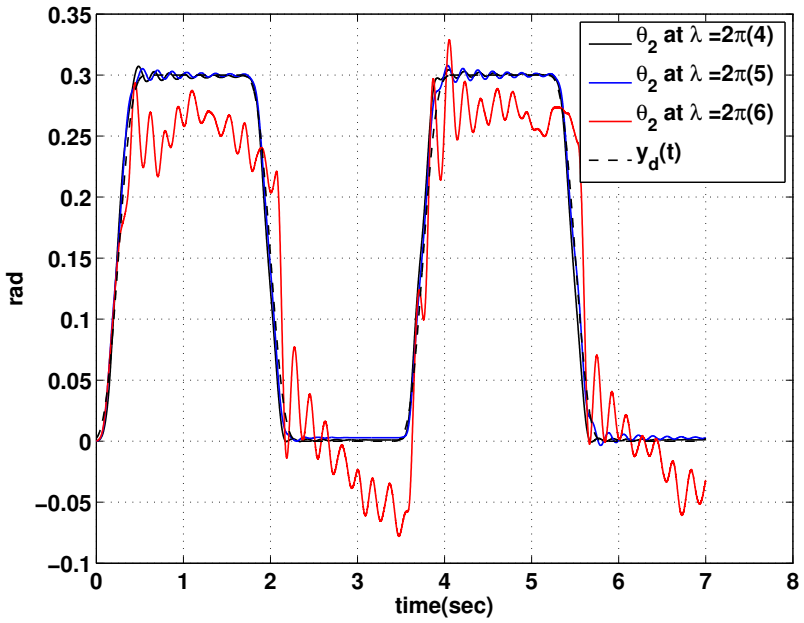

Figure 6.5. Load pulley output under assumptions of rigid cable and rigid motor joint.

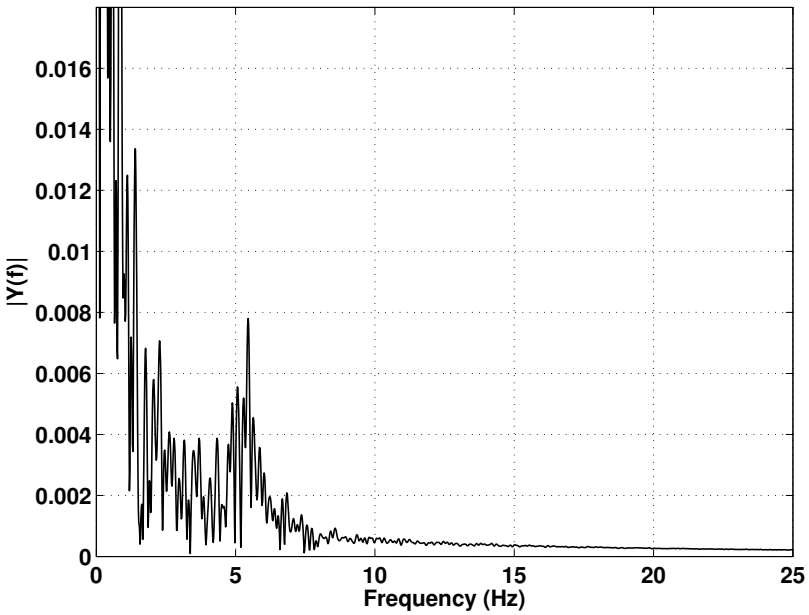

Figure 6.6. Frequency spectrum of load pulley output under rigid cable and motor joint assumption.

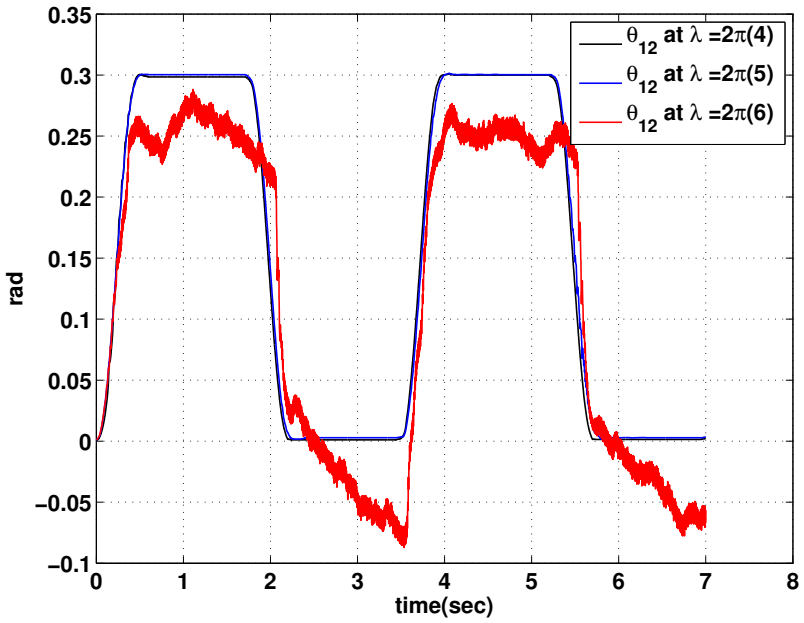

Figure 6.7. Drive pulley output under assumptions of rigid cable and rigid motor joint.

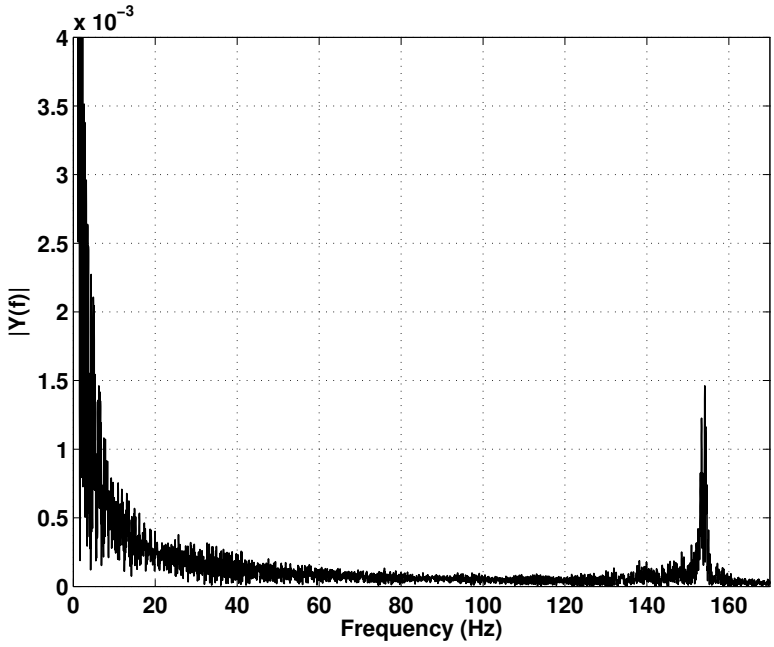

Figure 6.8. Frequency spectrum of load pulley output under rigid cable and motor joint assumption.

6.4 DARC with Matched Uncertainty: Model 2

Based on the dynamics in Eq. (6.10), the following states are defined:

$$\begin{aligned} x_1 &= \theta_2 = \theta_{12} \\ x_2 &= \dot{\theta}_2 = \dot{\theta}_{12} \\ x_3 &= \theta_{11} - \theta_{12} \\ x_4 &= \dot{\theta}_{11} - \dot{\theta}_{12} \end{aligned} \tag{6.38}$$

The system dynamics can be rewritten as follows:

$$\dot{x}_1 = x_2 \tag{6.39a}$$

$$\dot{x}_2 = \frac{k_m}{J_2 + J_{12}} x_3 = \beta x_3 = \bar{x}_3 \tag{6.39b}$$

$$\dot{\bar{x}}_3 = \beta x_4 = \bar{x}_4 \tag{6.39c}$$

$$\begin{aligned} \frac{J_{11}}{\beta}\dot{\bar{x}}_4 &= u - b_1(x_2 + x_4) - c_1 S_f(x_2 + x_4) + d_0 + \tilde{d}(t) - (p_2 + \frac{k_m}{\beta})\bar{x}_3 \\ \frac{p_2}{\beta}\dot{\bar{x}}_4 &= u - p_3(x_2 + x_4) - p_4 S_f(x_2 + x_4) + p_5 + \tilde{d}(t) - (p_2 + \frac{k_m}{\beta})\bar{x}_3 \end{aligned} \tag{6.39d}$$

$$y = x_1 \tag{6.39e}$$

where $\beta = \frac{k_m}{J_2 + J_{12}},\ \bar{x}_i = \beta x_i,\ i = 3, ..6.\ p_2 = J_{11},\ p_3 = b_1,\ p_4 = c_1,\ p_5 = d_0$. Let $y_d(t)$ be the reference angular trajectory, assumed to be bounded with bounded derivatives up to at least sixth order. Our control objective is to synthesize a control input $u(t)$ such that the output $y = \theta_2(t)$ tracks $y_d(t)$ as closely as possible. The following error variables are defined:

$$z_1 = x_1 - y_d \tag{6.40a}$$

$$z_2 = \dot{z}_1 = x_2 - y_d^{(1)} \tag{6.40b}$$

$$z_3 = \dot{z}_2 = \dot{x}_2 - y_d^{(2)} = \bar{x}_3 - y_d^{(2)} \tag{6.40c}$$

$$z_4 = \dot{z}_3 = \dot{\bar{x}}_3 - y_d^{(3)} = \bar{x}_4 - y_d^{(3)} \tag{6.40d}$$

where $y_d^{(i)}$ is the i^{th} time derivative of $y_d(t)$. The sliding surface is defined as follows:

$$\begin{aligned}\sigma(s) &= (s+\lambda)^3 z_1(s) \\ &= z_4 + 3z_3\lambda + 3z_2\lambda^2 + z_1\lambda^3 \end{aligned} \tag{6.41}$$

Differentiating σ and using Eq. (6.39),

$$\begin{aligned}\frac{p_2}{\beta}\dot{\sigma} =& \frac{p_2}{\beta}(\dot{z}_4 + 3z_4\lambda + 3z_3\lambda^2 + z_2\lambda^3) \\ =& \frac{p_2}{\beta}\dot{\bar{x}}_4 - \frac{p_2}{\beta}(y_d^{(4)} - 3z_4\lambda - 3z_3\lambda^2 - z_2\lambda^3) \\ =& u - p_3(x_2+x_4) - p_4 S_f(x_2+x_4) + p_5 + \tilde{d}(t) - (p_2 + \frac{k_m}{\beta})\bar{x}_3 - p_2\frac{z_{eq}}{\beta} \\ =& u - \frac{k_m}{\beta}\bar{x}_3 + \varphi^T p + \tilde{d}(t) \end{aligned} \tag{6.42}$$

where $z_{eq} = y_d^{(4)} - 3z_4\lambda - 3z_3\lambda^2 - z_2\lambda^3$ and $\varphi^T = [-\bar{x}_3 - \frac{z_{eq}}{\beta},\ -(x_2+x_4),\ -S_f(x_2+x_4),\ 1]$ and $p = [p_2,\ p_3,\ p_4,\ p_5]^T$. Hence the controller is designed as follows:

$$u = u_a + u_{s1} + u_{s2}$$

$$u_a = \frac{k_m}{\beta}\bar{x}_3 - \varphi^T\hat{p} \tag{6.43a}$$

$$u_{s1} = -k_\sigma\sigma \tag{6.43b}$$

$$u_{s2} = -k_{\sigma s}\sigma \tag{6.43c}$$

where k_σ is a positive feedback gain and $k_{\sigma s}$ is a positive nonlinear gain chosen large enough such that the following two conditions are satisfied:

$$Condition\ 1:\ \sigma(u_{s2} - \varphi^T\tilde{p} + \tilde{d}) \leq \epsilon \tag{6.44a}$$

$$Condition\ 2:\ \sigma u_{s2} \leq 0 \tag{6.44b}$$

With $K_\sigma = k_\sigma + k_{\sigma s}$, the controller results in the following sliding surface error dynamics,

$$\mu\dot{\sigma} + K_\sigma\sigma = -\varphi^T\tilde{p} + \tilde{d}(t) \tag{6.45}$$

where $\mu = \frac{J_{11}}{\beta}$. Proof of stability and tracking performance is the same as derived earlier in Model 1.

6.4.1 Experimental Results

Figure 6.9 shows the load pulley output under the DARC law defined in Eq. (6.43) using $\lambda = 2\pi(22)$. The frequency spectrum of the output in Figure 6.10 shows that the frequency of vibrations seen is the same as the dominant mode of the cable-pulley system caused by cable flexibility. In contrast with results from the previous model, the motor-joint vibration mode is not excited. However, even when the flexibility of the motor joint is modeled and cable flexibility is neglected, as is done commonly in literature, vibrations occur as closed-loop bandwidth is increased leading to deterioration of output tracking performance. These results further confirm the need to model the flexible mode of the system caused by cable flexibility.

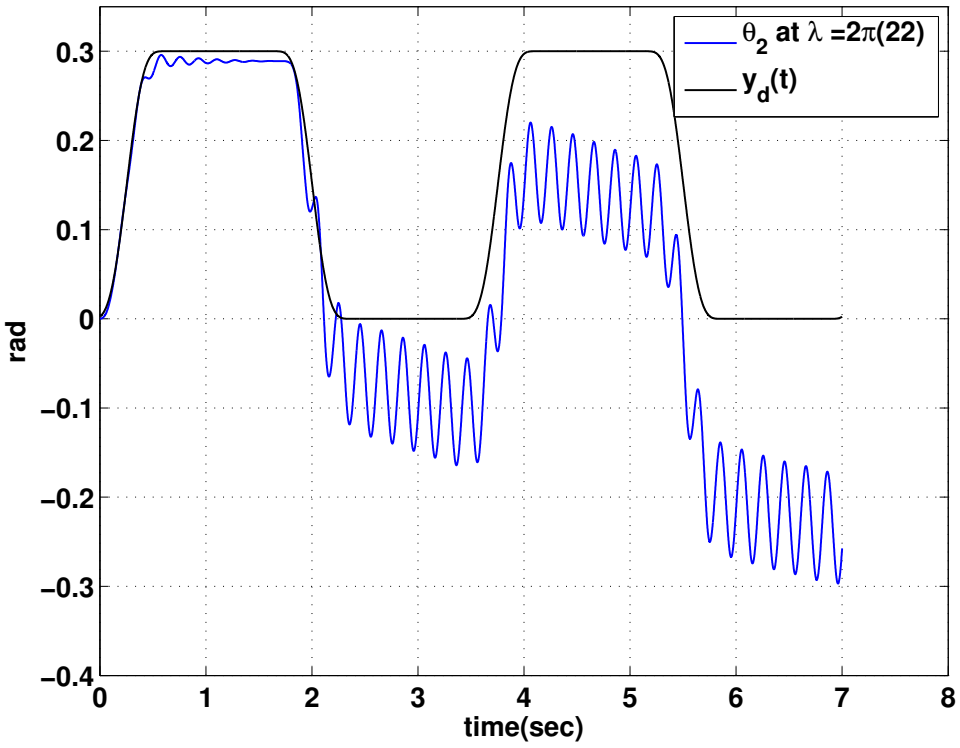

Figure 6.9. Load pulley output under assumptions of rigid cable and flexible motor joint.

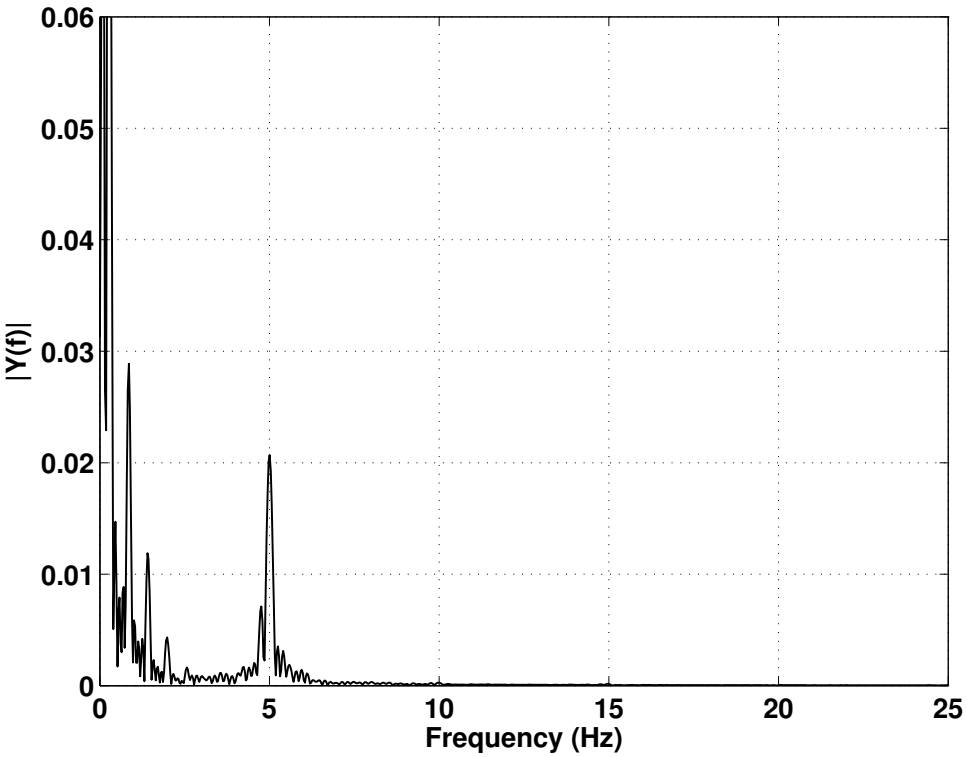

Figure 6.10. Frequency spectrum of load pulley output under rigid cable and flexible motor joint assumption.

6.5 DARC with Matched Uncertainty: Model 3

Based on the reduced system-order system dynamics in Eq. (6.11), the following state variables are defined:

$$\begin{aligned} x_1 &= \theta_2 \\ x_2 &= \dot{\theta}_2 \\ x_3 &= \theta_1 - \theta_2 \\ x_4 &= \dot{\theta}_1 - \dot{\theta}_2 \end{aligned} \tag{6.46}$$

The system dynamics in Eq. (6.11) can be expressed as,

$$\dot{x}_1 = x_2 \tag{6.47a}$$

$$\dot{x}_2 = \beta x_3 = \bar{x}_3 \tag{6.47b}$$

$$\dot{\bar{x}}_3 = \beta x_4 = \bar{x}_4 \tag{6.47c}$$

$$\frac{p_2}{\beta}\dot{\bar{x}}_4 = u - (J_2 + p_2)\bar{x}_3 - p_3(x_4 + x_2) - p_4 S_f(x_4 + x_2) + p_5 + \tilde{d}(t) \tag{6.47d}$$

$$y = x_1 \tag{6.47e}$$

where $\beta = \frac{2kr^2}{J_2} > 0$ is assumed known from offline measurement of the system's fundamental natural frequency and load inertia. $\bar{x}_i = \beta x_i,\ i = 3, 4.$ $p_2 = J_1, p_3 = b_1, p_4 = c_1, p_5 = d_0$ are constant model parameters that need to be estimated. $S_f(\bullet) = tanh(0.5\bullet)$ is a smooth approximation to the signum function and $u = \tau$ is the control input/drive torque.

Let $y_d(t)$ be the reference angular trajectory, assumed to be bounded with bounded derivatives up to at least fourth order. Our control objective is to synthesize a control input $u(t)$ such that the output $y = \theta_2(t)$ tracks $y_d(t)$ as closely as possible. The following error variables are defined:

$$z_1 = x_1 - y_d \tag{6.48a}$$

$$z_2 = \dot{z}_1 = x_2 - \dot{y}_d \tag{6.48b}$$

$$z_3 = \dot{z}_2 = \ddot{z}_1 = \bar{x}_3 - \ddot{y}_d \tag{6.48c}$$

$$z_4 = \dot{z}_3 = \dddot{z}_1 = \dot{\bar{x}}_3 - \dddot{y}_d = \bar{x}_4 - \dddot{y}_d \tag{6.48d}$$

A sliding surface is defined as follows:

$$\sigma(s) = (s + \lambda)^3 z_1(s) \tag{6.49}$$

Hence,

$$\begin{aligned} \sigma &= \dddot{z}_1 + 3\lambda\ddot{z}_1 + 3\lambda^2\dot{z}_1 + \lambda^3 z_1 \\ &= z_4 + 3\lambda z_3 + 3\lambda^2 z_2 + \lambda^3 z_1 \end{aligned} \tag{6.50}$$

Taking the derivative of σ and using Eq. (6.47),

$$\begin{aligned} p_2\dot{\sigma} =& p_2\dot{z}_4 + p_2(3\lambda z_4 + 3\lambda^2 z_3 + \lambda^3 z_2) \\ =& p_2\dot{\bar{x}}_4 - p_2(\dddot{y}_d - 3\lambda z_4 - 3\lambda^2 z_3 - \lambda^3 z_2) \\ =& \beta(u - (J_2 + p_2)\bar{x}_3 - p_3(x_4 + x_2) - p_4 S_f(x_4 + x_2) + p_5 + \tilde{d}) - p_2 z_{eq} \end{aligned} \tag{6.51}$$

where $z_{eq} = \ddot{y}_d - 3\lambda z_4 - 3\lambda^2 z_3 - \lambda^3 z_2$. Dividing by β and rearranging,

$$\begin{aligned} \frac{p_2}{\beta}\dot{\sigma} =& u - J_2\bar{x}_3 - p_2(\bar{x}_3 + \frac{z_{eq}}{\beta}) - p_3(x_4 + x_2) - p_4 S_f(x_4 + x_2) + p_5 + \tilde{d} \\ =& u - J_2\bar{x}_3 + \varphi^T p + \tilde{d} \end{aligned} \tag{6.52}$$

where $\varphi^T = [-\bar{x}_3 - \frac{z_{eq}}{\beta},\ -(x_4 + x_2),\ -S_f(x_4 + x_2),\ 1]$ and $p = [p_2,\ p_3,\ p_4,\ p_5]^T$. Hence the control law u is designed as follows,

$$u = u_a + u_{s1} + u_{s2}$$

$$u_a = J_2\bar{x}_3 - \varphi^T\hat{p} \tag{6.53a}$$

$$u_{s1} = -k_\sigma\sigma \tag{6.53b}$$

$$u_{s2} = -k_{\sigma s}\sigma \tag{6.53c}$$

where k_σ is a positive feedback gain and $k_{\sigma s}$ is a positive nonlinear gain chosen large enough such that the following two conditions are satisfied:

$$Condition\ 1:\ \sigma(u_{s2} - \varphi^T\tilde{p} + \tilde{d}) \leq \epsilon \tag{6.54a}$$

$$Condition\ 2:\ \sigma u_{s2} \leq 0 \tag{6.54b}$$

Condition 1 ensures that u_{s2} can attenuate uncertainties due to parametric uncertainty and uncertain nonlinearity to a constant $\epsilon > 0$ specified by the designer. Condition 2 guarantees that u_{s2} is dissipative in nature so as to not interfere with the functioning of the adaptation and to guarantee asymptotic tracking in the presence of parametric uncertainty alone. An example for choice of u_{s2} is as follows:

$$u_{s2} = -\frac{\sigma}{4\epsilon}[\|p_{max} - p_{min}\|^2\|\varphi\|^2 + \delta^2] \tag{6.55}$$

With $K_\sigma = k_\sigma + k_{\sigma s}$, the controller results in the following sliding surface error dynamics,

$$\mu\dot{\sigma} + K_\sigma\sigma = -\varphi^T\tilde{p} + \tilde{d}(t) \tag{6.56}$$

where $\mu = \frac{p_2}{\beta}$. Proof of stability and tracking performance is the same as derived earlier in Model 1.

6.5.1 Experimental Results

The upper and lower bounds on p_2 to p_5 were chosen as $[0.00185,\ 0.0033,\ 0.04,\ 0.01]$ and $[0.00165,\ 0.0029,\ 0.035,\ -0.01]$, respectively. $k_{\sigma s}$ was chosen to be large enough to satisfy Condition 1 in Eq. (6.54a). $\lambda = 2\pi(11)$ and $K_\sigma = 2\pi(13)\frac{J_1}{\beta}$ were chosen to obtain maximum tracking accuracy without exciting the unmodeled higher-order flexible mode of the motor joint. Figure 6.11 compares the desired trajectory to be tracked with the system output under the proposed controller. The tracking error is shown in Figure 6.12 where a tracking accuracy of 0.17deg was achieved, which is about five times the encoder resolution. Most of the tracking error originates from the unmodeled higher-order mode of the motor. Figure 6.13 shows the sliding surface value and Figure 6.14 shows the measured motor torque, which is below the maximum achievable value of 2.1Nm due to the chosen closed-loop poles. Online parameter estimates are shown in Figures 6.15 and 6.16. In each of these figures, the horizontal red lines indicate nominal parameter values from offline experiments. Although the online parameter estimates do not necessarily converge to their nominal values, they change to help reduce tracking error. They are also bounded due to the discontinuous projection law, thereby preserving robust performance of the controller.

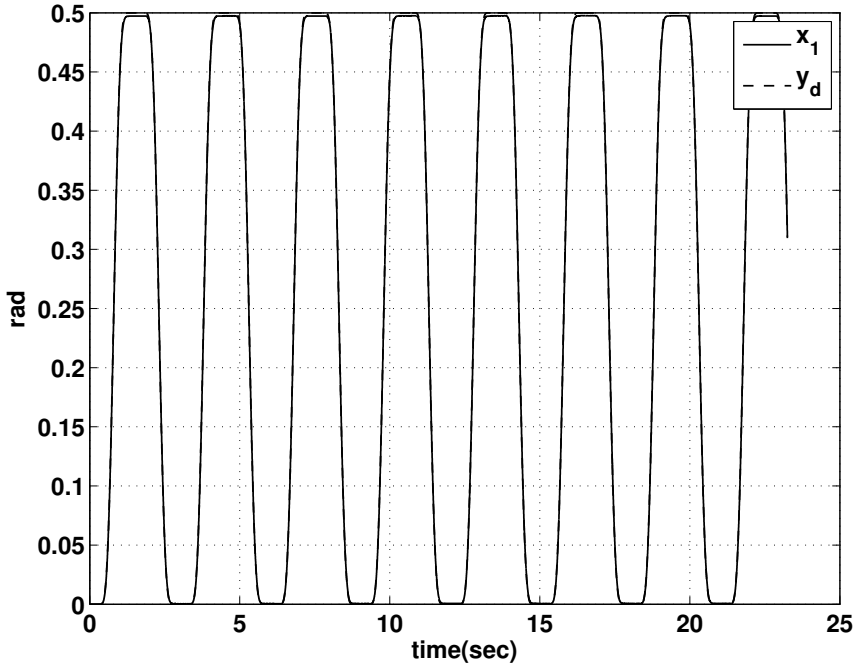

Figure 6.11. Desired trajectory (y_d) and output (x_1).

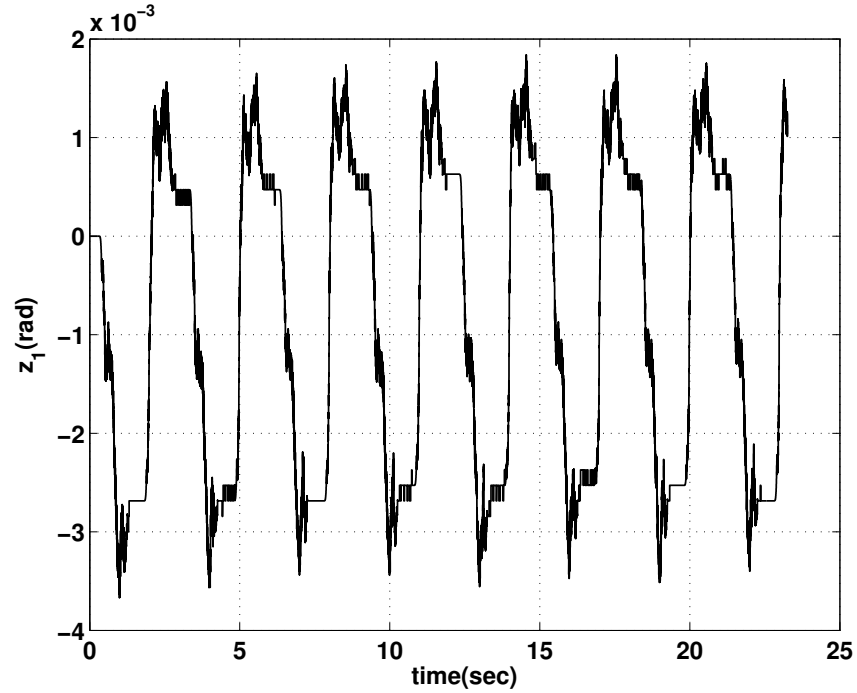

Figure 6.12. Output tracking error.

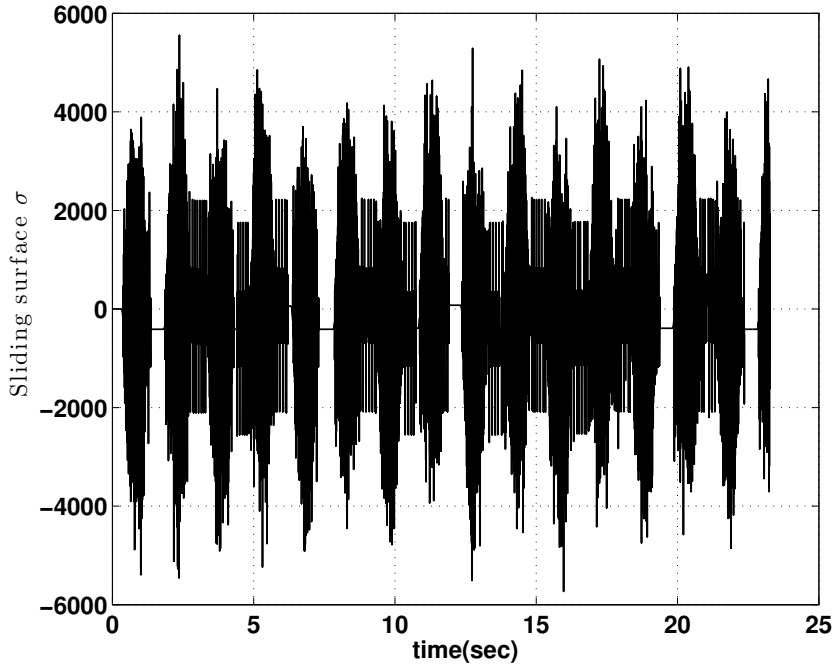

Figure 6.13. Sliding surface σ.

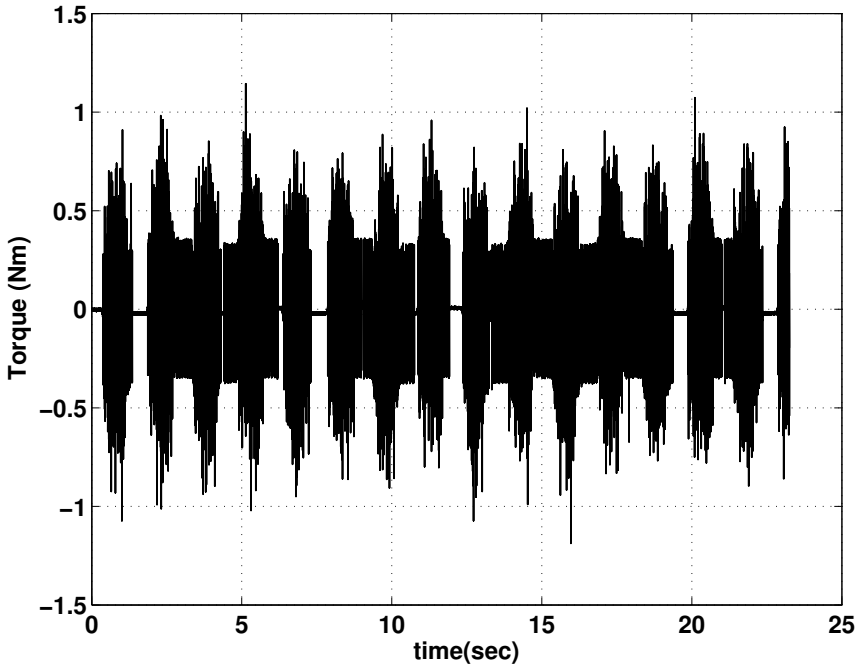

Figure 6.14. Control torque.

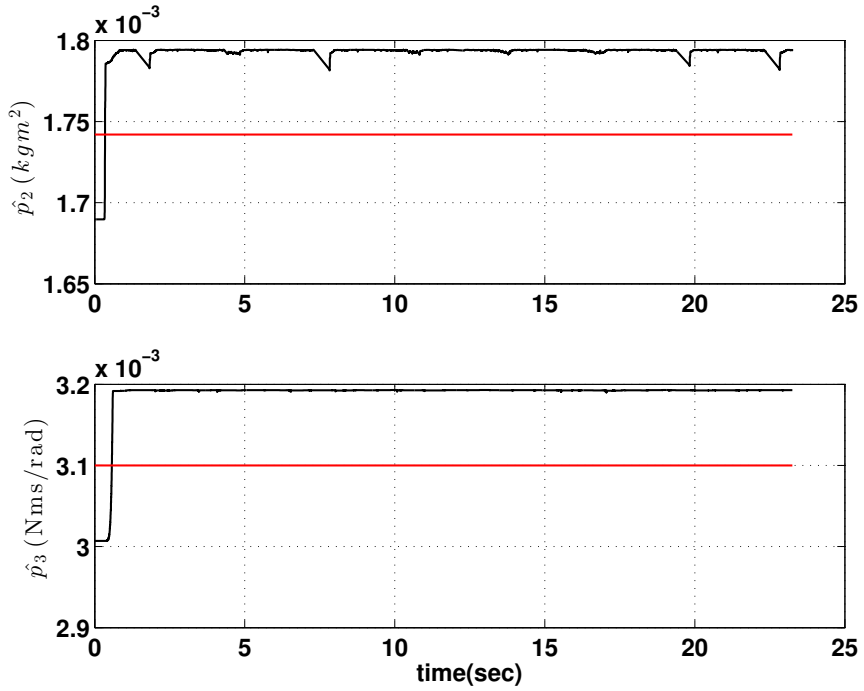

Figure 6.15. Parameter estimates $\hat{p}_2$ and $\hat{p}_3$.

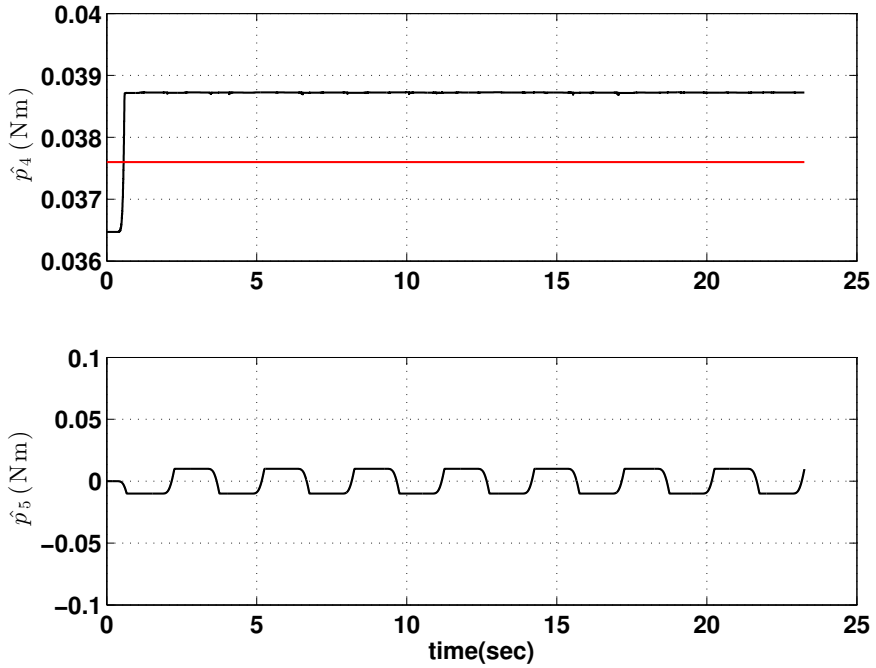

Figure 6.16. Parameter estimates $\hat{p}_4$ and $\hat{p}_5$.

6.6 DARC with Matched Uncertainty: Model 4

Based on the reduced-order system dynamics in Eq. (6.13), the following states are defined:

$$\begin{aligned} x_1 &= \theta_2 \\ x_2 &= \dot{\theta}_2 \\ x_3 &= \theta_{12} - \theta_2 \\ x_4 &= \dot{\theta}_{12} - \dot{\theta}_2 \\ x_5 &= \theta_{11} - \theta_{12} \\ x_6 &= \dot{\theta}_{11} - \dot{\theta}_{12} \end{aligned} \tag{6.57}$$

The system dynamics in Eq. (6.13) can be rewritten as follows:

$$\dot{x}_1 = x_2 \tag{6.58a}$$

$$\dot{x}_2 = \frac{2kr^2}{J_2} x_3 = \beta x_3 = \bar{x}_3 \tag{6.58b}$$

$$\dot{\bar{x}}_3 = \beta x_4 = \bar{x}_4 \tag{6.58c}$$

$$\dot{\bar{x}}_4 = -2kr^2 \left(\frac{1}{J_{12}} + \frac{1}{J_2} \right) \bar{x}_3 + \frac{k_m}{J_{12}} \bar{x}_5 \tag{6.58d}$$

$$\dot{\bar{x}}_5 = \beta x_6 = \bar{x}_6 \tag{6.58e}$$

$$\begin{aligned} \frac{J_{11}}{\beta} \dot{\bar{x}}_6 =& u - b_1(x_2 + x_4 + x_6) - c_1 S_f(x_2 + x_4 + x_6) + d_0 + \tilde{d}(t) \\ &+ 2kr^2 \frac{J_{11}}{J_{12}} x_3 - k_m \left(1 + \frac{J_{11}}{J_{12}} \right) x_5 \\ =& u - p_3(x_2 + x_4 + x_6) - p_4 S_f(x_2 + x_4 + x_6) + p_5 + \tilde{d}(t) \\ &- \frac{k_m}{\beta} \bar{x}_5 + p_2 \left(\frac{J_2}{J_{12}} \bar{x}_3 - \frac{k_m}{\beta J_{12}} \bar{x}_5 \right) \end{aligned} \tag{6.58f}$$

where $\beta = \frac{2kr^2}{J_2}$, $\bar{x}_i = \beta x_i$, $i = 3, ..6$. $p_2 = J_{11}$, $p_3 = b_1$, $p_4 = c_1$, $p_5 = d_0$. Let $y_d(t)$ be the reference angular trajectory, assumed to be bounded with bounded derivatives up to at least sixth order. Our control objective is to synthesize a control input $u(t)$ such that the output $y = \theta_2(t)$ tracks $y_d(t)$ as closely as possible.

The following error variables are defined:

$$z_1 = x_1 - y_d \tag{6.59a}$$

$$z_2 = \dot{z}_1 = x_2 - y_d^{(1)} \tag{6.59b}$$

$$z_3 = \dot{z}_2 = \dot{x}_2 - y_d^{(2)} = \bar{x}_3 - y_d^{(2)} \tag{6.59c}$$

$$z_4 = \dot{z}_3 = \dot{\bar{x}}_3 - y_d^{(3)} = \bar{x}_4 - y_d^{(3)} \tag{6.59d}$$

$$z_5 = \dot{z}_4 = \dot{\bar{x}}_4 - y_d^{(4)} = -2kr^2\left(\frac{1}{J_{12}} + \frac{1}{J_2}\right)\bar{x}_3 + \frac{k_m}{J_{12}}\bar{x}_5 - y_d^{(4)} \tag{6.59e}$$

$$\begin{aligned} z_6 =& \dot{z}_5 = -2kr^2\left(\frac{1}{J_{12}} + \frac{1}{J_2}\right)\dot{\bar{x}}_3 + \frac{k_m}{J_{12}}\dot{\bar{x}}_5 - y_d^{(5)} \\ =& -2kr^2\left(\frac{1}{J_{12}} + \frac{1}{J_2}\right)\bar{x}_4 + \frac{k_m}{J_{12}}\bar{x}_6 - y_d^{(5)} \end{aligned} \tag{6.59f}$$

where $y_d^{(i)}$ is the i^{th} time derivative of $y_d(t)$. The sliding surface is defined as follows:

$$\begin{aligned} \sigma(s) &= (s+\lambda)^5 z_1(s) \\ &= z_6 + 5z_5\lambda + 10z_4\lambda^2 + 10z_3\lambda^3 + 5z_2\lambda^4 + \lambda^5 z_1 \end{aligned} \tag{6.60}$$

Differentiating σ and using Eq. (6.58),

$$\begin{aligned} \frac{J_{11}}{\beta}\dot{\sigma} =& \frac{J_{11}}{\beta}(\dot{z}_6 + 5z_6\lambda + 10z_5\lambda^2 + 10z_4\lambda^3 + 5z_3\lambda^4 + \lambda^5 z_2) \\ =& \frac{J_{11}}{\beta}\left(-2kr^2(\frac{1}{J_{12}} + \frac{1}{J_2})\dot{\bar{x}}_4 + \frac{k_m}{J_{12}}\dot{\bar{x}}_6\right) - \frac{J_{11}}{\beta}z_{eq} \\ =& -J_{11}\left(1 + \frac{J_2}{J_{12}}\right)\dot{\bar{x}}_4 + \frac{k_m}{J_{12}}\frac{J_{11}}{\beta}\dot{\bar{x}}_6 - \frac{J_{11}}{\beta}z_{eq} \end{aligned} \tag{6.61}$$

where $z_{eq} = y_d^{(6)} - 5z_6\lambda - 10z_5\lambda^2 - 10z_4\lambda^3 - 5z_3\lambda^4 - \lambda^5 z_2$. Rearranging,

$$\begin{aligned} \frac{J_{11}J_{12}}{\beta k_m}\dot{\sigma} =& \frac{J_{11}}{\beta}\dot{\bar{x}}_6 - J_{11}\frac{J_{12}}{k_m}\left((1 + \frac{J_2}{J_{12}})\dot{\bar{x}}_4 + \frac{z_{eq}}{\beta}\right) \\ &= u - p_3(x_2 + x_4 + x_6) - p_4 S_f(x_2 + x_4 + x_6) + p_5 + \tilde{d}(t) \\ &- \frac{k_m}{\beta}\bar{x}_5 + p_2\left(\frac{J_2}{J_{12}}\bar{x}_3 - \frac{k_m}{\beta J_{12}}\bar{x}_5\right) - p_2\frac{J_{12}}{k_m}\left((1 + \frac{J_2}{J_{12}})\dot{\bar{x}}_4 + \frac{z_{eq}}{\beta}\right) \\ &= u - \frac{k_m}{\beta}\bar{x}_5 + \varphi^T p + \tilde{d}(t) \end{aligned} \tag{6.62}$$

where $\varphi^T = [-\varphi_2,\ -(x_2 + x_4 + x_6),\ -S_f(x_2 + x_4 + x_6),\ 1]$ and $p = [p_2,\ p_3,\ p_4,\ p_5]^T$. φ_2 is given by,

$$\varphi_2 = \frac{J_{12}}{k_m}\left((1 + \frac{J_2}{J_{12}})\dot{\bar{x}}_4 + \frac{z_{eq}}{\beta}\right) - \left(\frac{J_2}{J_{12}}\bar{x}_3 - \frac{k_m}{\beta J_{12}}\bar{x}_5\right)$$

Hence the controller is designed as follows:

$$u = u_a + u_{s1} + u_{s2}$$

$$u_a = \frac{k_m}{\beta}\bar{x}_5 - \varphi^T\hat{p} \tag{6.63a}$$

$$u_{s1} = -k_\sigma\sigma \tag{6.63b}$$

$$u_{s2} = -k_{\sigma s}\sigma \tag{6.63c}$$

where k_σ is a positive feedback gain and $k_{\sigma s}$ is a positive nonlinear gain chosen large enough such that the following two conditions are satisfied:

$$Condition\ 1:\ \sigma(u_{s2} - \varphi^T\tilde{p} + \tilde{d}) \leq \epsilon \tag{6.64a}$$

$$Condition\ 2:\ \sigma u_{s2} \leq 0 \tag{6.64b}$$

With $K_\sigma = k_\sigma + k_{\sigma s}$, the controller results in the following sliding surface error dynamics,

$$\mu\dot{\sigma} + K_\sigma\sigma = -\varphi^T\tilde{p} + \tilde{d}(t) \tag{6.65}$$

where $\mu = \frac{J_{11}J_{12}}{\beta k_m}$.

6.6.1 Experimental Results

The upper and lower bounds on p_2 to p_5 were chosen as $[0.0013,\ 0.0033,\ 0.04,\ 0.01]$ and $[0.009,\ 0.0029,\ 0.035,\ -0.01]$, respectively. $\lambda = 2\pi(23)$ and $K_\sigma = 2\pi(25)\frac{J_{11}J_{12}}{\beta k_m}$ were chosen. Figure 6.17 compares the desired trajectory to be tracked with the system output under the proposed controller. The tracking error is shown in Figure 6.18 where a tracking accuracy of 0.055deg was achieved, which is less than twice the encoder resolution. Figure 6.19 shows the sliding surface value and Figure 6.20 shows the measured motor torque, which is below the maximum achievable value of 2Nm. Online parameter estimates are shown in Figures 6.21 and 6.22.

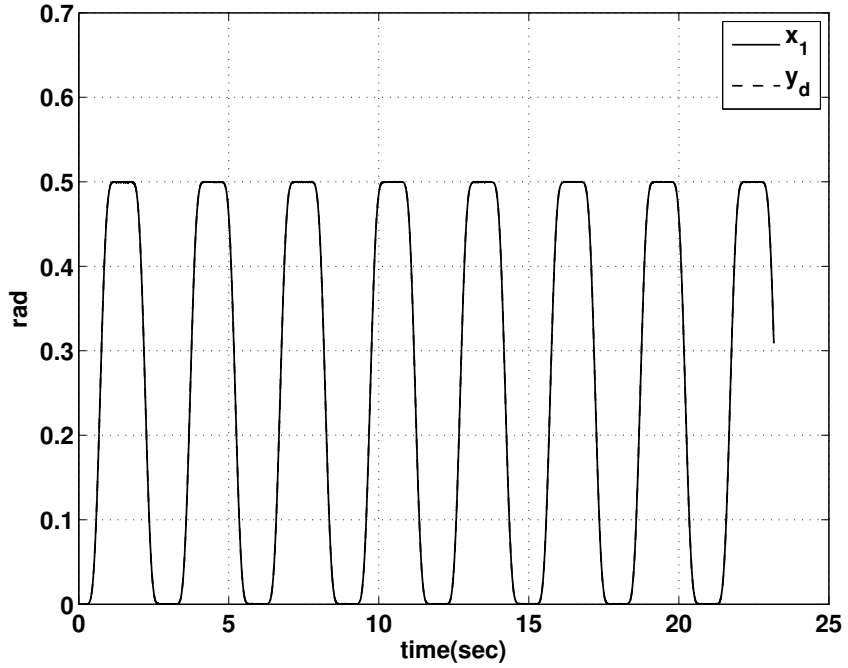

Figure 6.17. Desired trajectory (y_d) and output (x_1).

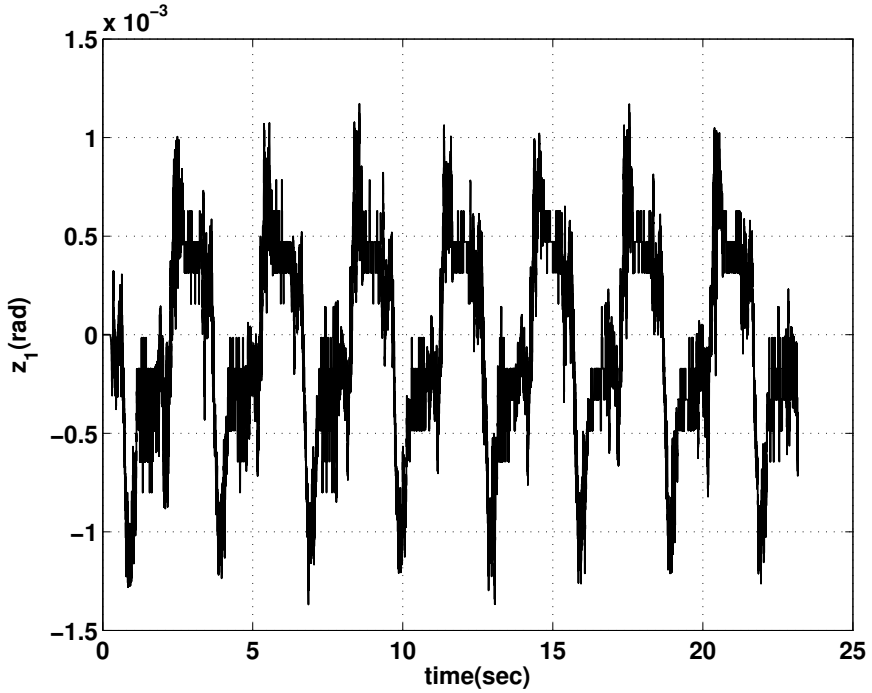

Figure 6.18. Output tracking error.

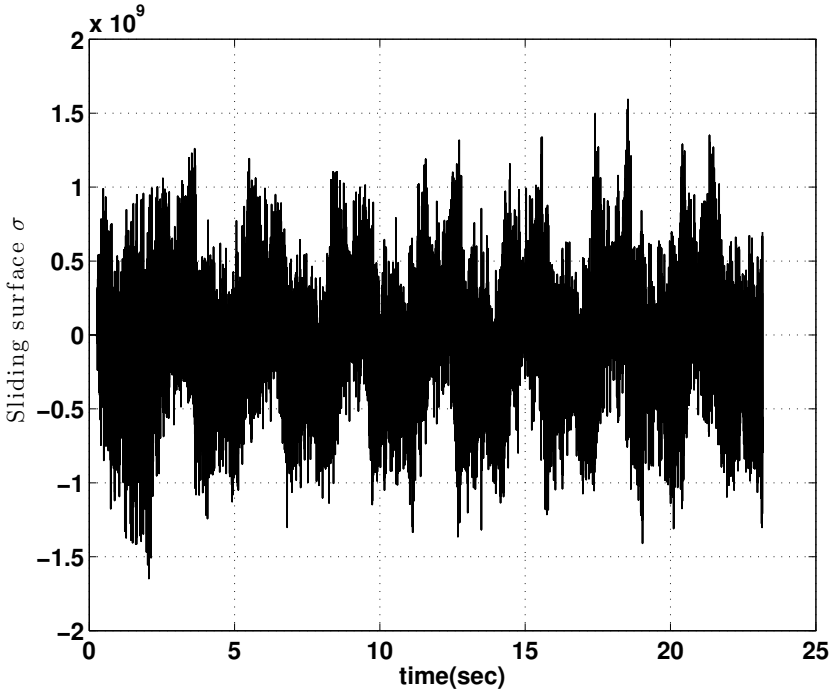

Figure 6.19. Sliding surface σ.

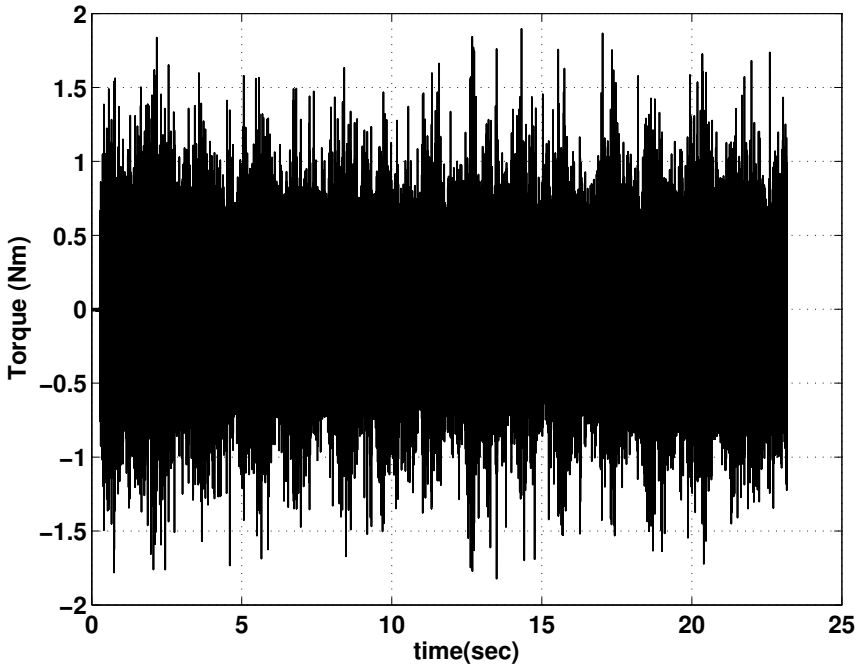

Figure 6.20. Control torque.

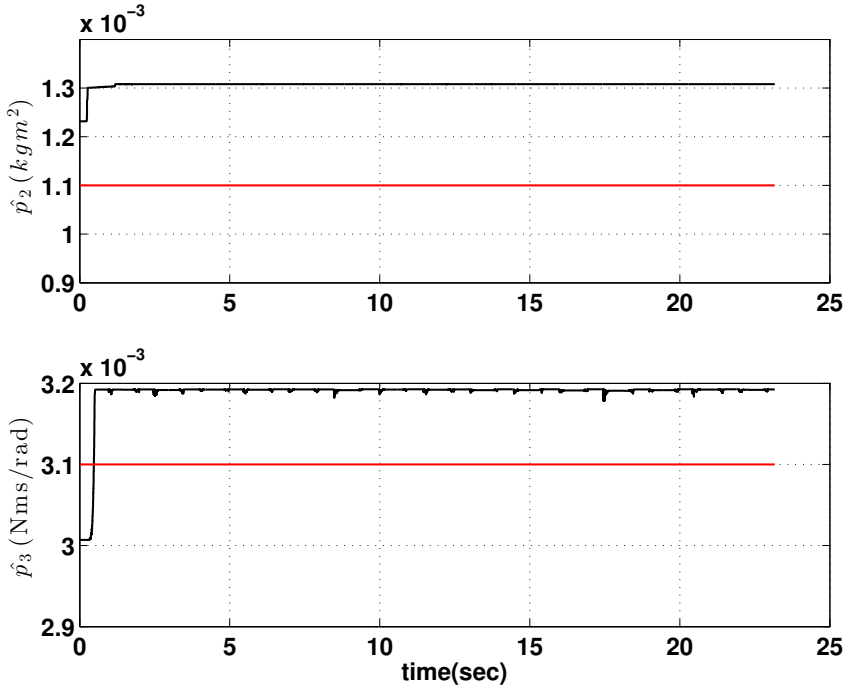

Figure 6.21. Parameter estimates $\hat{p}_2$ and $\hat{p}_3$.

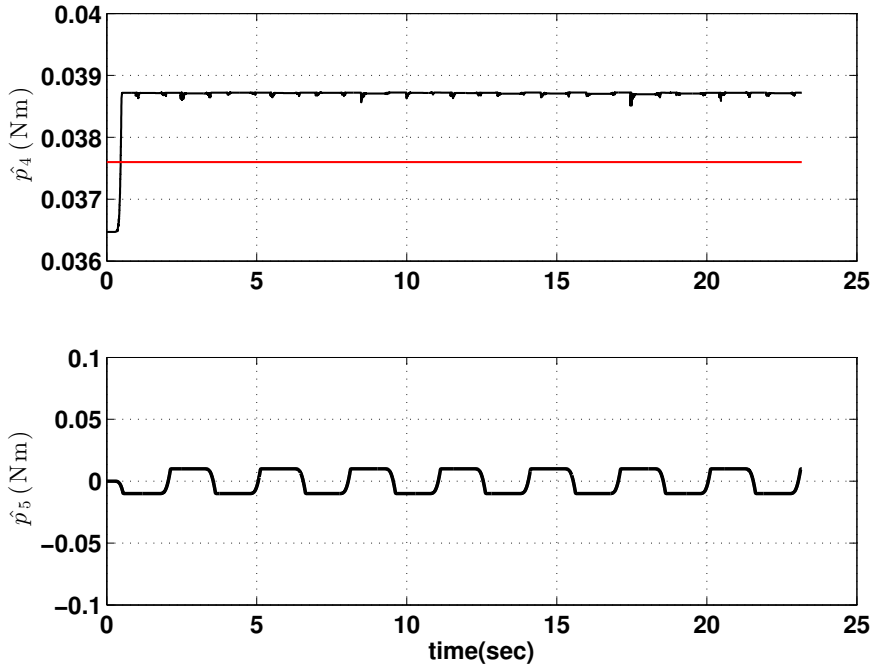

Figure 6.22. Parameter estimates $\hat{p}_4$ and $\hat{p}_5$.

6.7 Backstepping DARC with Unmatched Uncertainty: Model 1

Based on the system in Figure 6.2, the pulley dynamics can be written as follows.

$$J_1\ddot{\theta}_1 = u - 2kr(r\theta_1 - r\theta_2) - b_1\dot{\theta}_1 - c_1 S_f(\dot{\theta}_1) + d_1 + \tilde{d}_1(t) \tag{6.66}$$

$$J_2\ddot{\theta}_2 = 2kr(r\theta_1 - r\theta_2) + d_2 + \tilde{d}_2(t) \tag{6.67}$$

where $u = \tau$ is the control torque from the motor, b_1, c_1 are constant parameters that represent coefficients of viscous damping and coulomb friction, respectively, of the motor. d_1, d_2 represent the constant parts of modeling uncertainty and $\tilde{d}_1(t), \tilde{d}_2(t)$ represent the time-varying parts. $S_f(\bullet) = tanh(0.5\bullet)$ is a smooth approximation to the signum function. Using the following transformed state variables,

$$\begin{aligned} x_1 &= \theta_2 \\ x_2 &= \dot{\theta}_2 \\ x_3 &= \theta_1 - \theta_2 \\ x_4 &= \dot{\theta}_1 - \dot{\theta}_2 \end{aligned} \tag{6.68}$$

the state dynamics can be rewritten as follows:

$$\dot{x}_1 = x_2 \tag{6.69a}$$

$$\begin{aligned} \dot{x}_2 =& \frac{2kr^2}{J_2}x_3 + p_2 + \tilde{d}_2(t) = \frac{\beta}{\beta_n}\beta_n x_3 + p_2 + \tilde{d}_2(t) \\ =& p_1\bar{x}_3 + p_2 + \tilde{d}_2(t) \end{aligned} \tag{6.69b}$$

$$\dot{\bar{x}}_3 = \beta_n x_4 = \bar{x}_4 \tag{6.69c}$$

$$\begin{aligned} J_1\dot{\bar{x}}_4 =& \beta_n(u - 2kr^2x_3 - J_1p_1\bar{x}_3 - b_1(x_4 + x_2) - c_1S_f(x_4 + x_2) + d_1 \\ & - J_1p_2 + \tilde{d}_1(t) - J_1\tilde{d}_2(t)) \end{aligned}$$

$$\dot{\bar{x}}_4 = \beta_n p_7 u - p_3\bar{x}_3 - p_4(x_4 + x_2) - p_5 S_f(x_4 + x_2) + p_6 + \tilde{d}(t) \tag{6.69d}$$

$$y = x_1 \tag{6.69e}$$

where $u = \tau$ is the drive motor torque. $\beta = \frac{2kr^2}{J_2}$ and its nominal value is β_n. $\bar{x}_i = \beta_n x_i,\ i = 3, 4.$ $p_1 = \frac{\beta}{\beta_n},\ p_2 = \frac{d_2}{J_2},\ p_3 = (\frac{2kr^2}{\beta_n} + J_1p_1)\frac{\beta_n}{J_1},\ p_4 = b_1\frac{\beta_n}{J_1},\ p_5 =$

$c_1\frac{\beta_n}{J_1}$, $p_6 = (d_1 - J_1 p_2)\frac{\beta_n}{J_1}$, $p_7 = \frac{1}{J_1}$, are constant model parameters that need to be estimated. In the formulation above, unmatched uncertainties are considered, i.e., some uncertainty exists in the coefficient of the control input. This is a direct consequence of assuming uncertainties in the load pulley dynamics unlike previous models with only matched uncertainties where load inertia was assumed known and no modeling uncertainties were assumed in the load pulley dynamics. The output tracking error is given by,

$$z_1 = y - y_d = x_1 - y_d \tag{6.70}$$

Differentiating z_1,

$$\begin{aligned} \dot{z}_1 &= \dot{x}_1 - \dot{y}_d = x_2 - \dot{y}_d \\ &= z_2 + \alpha_1 - \dot{y}_d \end{aligned} \tag{6.71}$$

where $z_2 = x_2 - \alpha_1$ has been defined. The virtual control input α_1 is designed as $\alpha_1 = \dot{y}_d - k_1 z_1$, leading to the following error dynamics:

$$\dot{z}_1 + k_1 z_1 = z_2 \tag{6.72}$$

where k_1 is a positive gain to be chosen. Setting a Lyapunov candidate for z_1 and differentiating,

$$\begin{aligned} V_1 =& \frac{z_1^2}{2} \\ \dot{V}_1 =& z_1 \dot{z}_1 = z_1 z_2 - k_1 z_1^2 \end{aligned} \tag{6.73}$$

$\dot{\alpha}_1$ is defined as follows:

$$\dot{\alpha}_1 = \frac{\partial \alpha_1}{\partial t} + \frac{\partial \alpha_1}{\partial x_1} x_2 = \ddot{y}_d - k_1 x_2 + k_1 \dot{y}_d \tag{6.74}$$

Differentiating z_2,

$$\begin{aligned} \dot{z}_2 =& \dot{x}_2 - \dot{\alpha}_1 = p_1 \bar{x}_3 + p_2 + \tilde{d}_2(t) - \dot{\alpha}_1 \\ =& p_1 z_3 + p_1 \alpha_2 + p_2 + \tilde{d}_2(t) - \dot{\alpha}_1 \end{aligned} \tag{6.75}$$

where $z_3 = \bar{x}_3 - \alpha_2$ has been defined. The virtual control input α_2 is designed as,

$$\alpha_2 = \alpha_{2a} + \alpha_{2s} = \alpha_{2a} + \alpha_{2g} + \alpha_{2r} \tag{6.76a}$$

$$\alpha_{2a} = \frac{\dot{\alpha}_1 - \hat{p}_2}{\hat{p}_1} = \frac{\ddot{y}_d - k_1 x_2 + k_1 \dot{y}_d - \hat{p}_2}{\hat{p}_1} \tag{6.76b}$$

$$\alpha_{2g} = -\frac{k_{2g2} z_2}{\hat{p}_1} - \frac{k_{2g1} z_1}{\hat{p}_1} \tag{6.76c}$$

$$\alpha_{2r} = -\frac{k_{2r} z_2}{\hat{p}_1} = -k_{2r} \frac{(x_2 - \dot{y}_d + k_1 x_1 - k_1 y_d)}{\hat{p}_1} \tag{6.76d}$$

where k_{2g1}, k_{2g2} are positive feedback gains and k_{2r} is a positive nonlinear feedback gain chosen such that the following conditions hold:

$$z_2(\alpha_{2r} - \phi_2^T \tilde{p} + \tilde{d}_2(t)) \leq \epsilon_2 \tag{6.77a}$$

$$z_2 \alpha_{2r} \leq 0 \tag{6.77b}$$

where $\phi_2^T = [\frac{\dot{\alpha}_1 - \hat{p}_2 - k_{2s} z_2}{\hat{p}_1},\ 1,\ 0,\ 0,\ 0,\ 0,\ 0]$, $\tilde{p} = [\tilde{p}_1,\ \tilde{p}_2,\ \tilde{p}_3,\ \tilde{p}_4,\ \tilde{p}_5,\ \tilde{p}_6,\ \tilde{p}_7]^T$ and $k_{2s} = k_{2g1} + k_{2g2} + k_{2r}$. ϵ_2 is a positive constant chosen by the designer. This leads to the following z_2 error dynamics:

$$\begin{aligned}
\dot{z}_2 =& p_1 z_3 + \frac{p_1}{\hat{p}_1}(\dot{\alpha}_1 - \hat{p}_2 + \alpha_{2s}) + p_2 - \dot{\alpha}_1 + \tilde{d}_2(t) \\
=& p_1 z_3 + \frac{\hat{p}_1 - \tilde{p}_1}{\hat{p}_1}(\dot{\alpha}_1 - \hat{p}_2 + \alpha_{2s}) + p_2 - \dot{\alpha}_1 + \tilde{d}_2(t) \\
=& p_1 z_3 - \frac{\tilde{p}_1}{\hat{p}_1}(\dot{\alpha}_1 - \hat{p}_2 + \alpha_{2s}) - \tilde{p}_2 - k_{2g2} z_2 - k_{2g1} z_1 + \tilde{d}_2(t) + \alpha_{2r} \\
=& p_1 z_3 - k_{2g2} z_2 - k_{2g1} z_1 + \alpha_{2r} - \phi_2^T \tilde{p} + \tilde{d}_2(t)
\end{aligned} \tag{6.78}$$

Defining the second Lyapunov function and differentiating,

$$\begin{aligned}
V_2 =& V_1 + \frac{z_2^2}{2} \\
\dot{V}_2 =& \dot{V}_1 + z_2 \dot{z}_2 \\
=& z_1 z_2 - k_1 z_1^2 + p_1 z_2 z_3 - k_{2g2} z_2^2 - k_{2g1} z_1 z_2 + z_2(\alpha_{2r} - \phi_2^T \tilde{p} + \tilde{d}_2(t))
\end{aligned} \tag{6.79}$$

Differentiating z_3,

$$\begin{aligned}\dot{z}_3 =&\dot{\bar{x}}_3 - \dot{\alpha}_2 = \bar{x}_4 - \dot{\alpha}_2\\ =&z_4 + \alpha_3 - \dot{\alpha}_2\\ =&z_4 + \alpha_3 - \left(\frac{\partial \alpha_2}{\partial t} + \frac{\partial \alpha_1}{\partial x_1}x_2 + \frac{\partial \alpha_2}{\partial x_2}\dot{x}_2 + \frac{\partial \alpha_2}{\partial \hat{p}}\dot{\hat{p}}\right)\end{aligned} \tag{6.80}$$

where $\frac{\partial \alpha_2}{\partial \hat{p}}\dot{\hat{p}} = \frac{\partial \alpha_2}{\partial \hat{p}_1}\dot{\hat{p}_1} + \frac{\partial \alpha_2}{\partial \hat{p}_2}\dot{\hat{p}_2}$ and $z_4 = \bar{x}_4 - \alpha_3$ has been defined. The following derivatives are obtained:

$$\frac{\partial \alpha_2}{\partial t} = \frac{\dddot{y}_d + k_1\ddot{y}_d - (k_{2g2} + k_{2r})(-\ddot{y}_d - k_1\dot{y}_d)}{\hat{p}_1} + \frac{k_{2g1}\dot{y}_d}{\hat{p}_1} \tag{6.81a}$$

$$\frac{\partial \alpha_2}{\partial x_1} = -\frac{(k_{2g2} + k_{2r})k_1}{\hat{p}_1} - \frac{k_{2g1}}{\hat{p}_1} \tag{6.81b}$$

$$\frac{\partial \alpha_2}{\partial x_2} = \frac{-k_1 - k_{2g2} - k_{2r}}{\hat{p}_1} \tag{6.81c}$$

The virtual control α_3 is designed as follows:

$$\alpha_3 = \alpha_{3a} + \alpha_{3s} = \alpha_{3a} + \alpha_{3g} + \alpha_{3r} \tag{6.82a}$$

$$\alpha_{3a} = \frac{\partial \alpha_2}{\partial t} + \frac{\partial \alpha_2}{\partial x_1}x_2 + \frac{\partial \alpha_2}{\partial x_2}\hat{\dot{x}}_2 \tag{6.82b}$$

$$\alpha_{3g} = -k_{3g3}z_3 - k_{3g2}z_2 \tag{6.82c}$$

$$\alpha_{3r} = -k_{3r}z_3 \tag{6.82d}$$

where $\hat{\dot{x}}_2 = \dot{x}_2|_{p=\hat{p}} = \hat{p}_1\bar{x}_3 + \hat{p}_2$. k_{3g3}, k_{3g2} are positive feedback gains and k_{3r} is a positive nonlinear feedback gain chosen such that the following conditions hold:

$$z_3(\alpha_{3r} - \phi_3^T\tilde{p} + \tilde{d}_3(t)) \leq \epsilon_3 \tag{6.83a}$$

$$z_3\alpha_{3r} \leq 0 \tag{6.83b}$$

where

$$\phi_3^T = \frac{\partial \alpha_2}{\partial x_2}[-\bar{x}_3,\ -1,\ 0,\ 0,\ 0,\ 0,\ 0] \tag{6.84a}$$

$$\tilde{d}_3(t) = -\frac{\partial \alpha_2}{\partial x_2}\tilde{d}_2(t) \tag{6.84b}$$

and ϵ_3 is chosen by the designer. This results in the following z_3 error dynamics,

$$\begin{aligned}
\dot{z}_3 =& z_4 + \frac{\partial \alpha_2}{\partial x_2}(\hat{\dot{x}_2} - \dot{x}_2) - \frac{\partial \alpha_2}{\partial \hat{p}}\dot{\hat{p}} - k_{3g3}z_3 - k_{3g2}z_2 + \alpha_{3r} \\
=& z_4 + \frac{\partial \alpha_2}{\partial x_2}(\hat{p}_1\bar{x}_3 + \hat{p}_2 - p_1\bar{x}_3 - p_2 - \tilde{d}_2(t)) - \frac{\partial \alpha_2}{\partial \hat{p}}\dot{\hat{p}} - k_{3g3}z_3 - k_{3g2}z_2 + \alpha_{3r} \\
=& z_4 - \frac{\partial \alpha_2}{\partial x_2}(-\tilde{p}_1\bar{x}_3 - \tilde{p}_2 + \tilde{d}_2(t)) - \frac{\partial \alpha_2}{\partial \hat{p}}\dot{\hat{p}} - k_{3g3}z_3 - k_{3g2}z_2 + \alpha_{3r} \\
=& z_4 + \alpha_{3r} - \phi_3^T\tilde{p} + \tilde{d}_3(t) - \frac{\partial \alpha_2}{\partial \hat{p}}\dot{\hat{p}} - k_{3g3}z_3 - k_{3g2}z_2
\end{aligned} \tag{6.85}$$

Defining the third Lyapunov function and differentiating,

$$\begin{aligned}
V_3 =& V_2 + \frac{z_3^2}{2} \\
\dot{V}_3 =& \dot{V}_2 + z_3\dot{z}_3 \\
=& z_1z_2 - k_1z_1^2 + p_1z_2z_3 - k_{2g2}z_2^2 - k_{2g1}z_1z_2 + z_2(\alpha_{2r} - \phi_2^T\tilde{p} + \tilde{d}_2(t) \qquad (6.86) \\
&+ z_3z_4 + z_3(\alpha_{3r} - \phi_3^T\tilde{p} + \tilde{d}_3(t)) - z_3\frac{\partial \alpha_2}{\partial \hat{p}}\dot{\hat{p}} - k_{3g3}z_3^2 - k_{3g2}z_2z_3 \qquad (6.87)
\end{aligned}$$

Differentiating z_4,

$$\begin{aligned}
\dot{z}_4 =& \dot{\bar{x}}_4 - \dot{\alpha}_3 \\
=& \beta_n p_7 u - p_3\bar{x}_3 - p_4(x_4 + x_2) - p_5S_f(x_4 + x_2) + p_6 + \tilde{d}(t) - \frac{\partial \alpha_3}{\partial \hat{p}}\dot{\hat{p}} \\
&- \left(\frac{\partial \alpha_3}{\partial t} + \frac{\partial \alpha_3}{\partial x_1}x_2 + \frac{\partial \alpha_3}{\partial x_2}\dot{x}_2 + \frac{\partial \alpha_3}{\partial \bar{x}_3}\bar{x}_4\right)
\end{aligned} \tag{6.88}$$

where $\frac{\partial \alpha_3}{\partial \hat{p}}\dot{\hat{p}} = \frac{\partial \alpha_3}{\partial \hat{p}_1}\dot{\hat{p}}_1 + \frac{\partial \alpha_3}{\partial \hat{p}_2}\dot{\hat{p}}_2$. The following derivatives are obtained as,

$$\frac{\partial \alpha_3}{\partial t} = \frac{\dddot{y}_d + k_1\ddot{y}_d - (k_{2g2} + k_{2r})(-\ddot{y}_d - k_1\dot{y}_d)}{\hat{p}_1} \tag{6.89a}$$

$$+ \frac{k_{2g1}\dot{y}_d}{\hat{p}_1} + (k_{3g3} + k_{3r})\frac{\partial \alpha_2}{\partial t} + k_{3g2}\frac{\partial \alpha_1}{\partial t} \tag{6.89b}$$

$$\frac{\partial \alpha_3}{\partial x_1} = (k_{3g3} + k_{3r})\frac{\partial \alpha_2}{\partial x_1} + k_{3g2}\frac{\partial \alpha_1}{\partial x_1} \tag{6.89c}$$

$$\frac{\partial \alpha_3}{\partial x_2} = -\frac{(k_{2g2} + k_{2r})k_1}{\hat{p}_1} + (k_{3g3} + k_{3r})\frac{\partial \alpha_2}{\partial x_2} \tag{6.89d}$$

$$\frac{\partial \alpha_3}{\partial \bar{x}_3} = -k_1 - k_{2g2} - k_{2r} - k_{3g3} - k_{3r} \tag{6.89e}$$

Hence control $u = \alpha_4$ is designed as follows:

$$\begin{aligned}
\alpha_4 =& \alpha_{4a} + \alpha_{4s} = \alpha_{4a} + \alpha_{4g} + \alpha_{4r} \\
\alpha_{4a} =& \Bigg[\hat{p}_3 \bar{x}_3 + \hat{p}_4 (x_4 + x_2) + \hat{p}_5 S_f(x_4 + x_2) - \hat{p}_6 \\
& + \left(\frac{\partial \alpha_3}{\partial t} + \frac{\partial \alpha_3}{\partial x_1} x_2 + \frac{\partial \alpha_3}{\partial x_2} \hat{\dot{x}}_2 + \frac{\partial \alpha_3}{\partial \bar{x}_3} \bar{x}_4 \right) \Bigg] \frac{1}{\beta_n \hat{p}_7} \qquad (6.90a) \\
\alpha_{4g} =& \frac{-k_{4g4} z_4 - k_{4g3} z_3 - k_{4g2} z_2}{\beta_n \hat{p}_7} \qquad (6.90b) \\
\alpha_{4r} =& -\frac{k_{4r} z_4}{\beta_n \hat{p}_7} \qquad (6.90c)
\end{aligned}$$

$k_{4g4}, k_{4g3}, k_{4g2}$ are positive feedback gains and k_{4r} is a positive nonlinear feedback gain chosen such that the following conditions hold:

$$\begin{aligned}
z_4(\alpha_{4r} - \phi_4^T \tilde{p} + \tilde{d}_4(t)) \leq & \epsilon_4 \qquad (6.91a) \\
z_4 \alpha_{4r} \leq & 0 \qquad (6.91b)
\end{aligned}$$

where $\phi_4, \tilde{d}_4(t)$ are defined later and ϵ_4 is chosen by the designer. The controller results in the following z_4 error dynamics,

$$\begin{aligned}
\dot{z}_4 =& \tilde{p}_3 \bar{x}_3 + \tilde{p}_4 (x_4 + x_2) + \tilde{p}_5 S_f(x_4 + x_2) - \tilde{p}_6 - \tilde{p}_7 \beta_n \alpha_4 + \tilde{d}(t) \\
& - k_{4g4} z_4 - k_{4g3} z_3 - k_{4g2} z_2 + \alpha_{4r} + \frac{\partial \alpha_3}{\partial x_2} (\tilde{p}_1 \bar{x}_3 + \tilde{p}_2 + \tilde{d}_2(t)) - \frac{\partial \alpha_3}{\partial \hat{p}} \dot{\hat{p}} \\
=& \alpha_{4r} - \phi_4^T \tilde{p} + \tilde{d}_4(t) - \frac{\partial \alpha_3}{\partial \hat{p}} \dot{\hat{p}} - k_{4g4} z_4 - k_{4g3} z_3 - k_{4g2} z_2 \qquad (6.92)
\end{aligned}$$

where ϕ_4 and $\tilde{d}_4$ are given by,

$$\begin{aligned}
\phi_4^T =& \left[-\frac{\partial \alpha_3}{\partial x_2} \bar{x}_3, -\frac{\partial \alpha_3}{\partial x_2}, -\bar{x}_3, -(x_2 + x_4), -S_f(x_2 + x_4), 1, \beta_n \alpha_4 \right] \qquad (6.93a) \\
\tilde{d}_4(t) =& \tilde{d}(t) + \frac{\partial \alpha_3}{\partial x_2} \tilde{d}_2(t) \qquad (6.93b)
\end{aligned}$$

Defining and differentiating the final Lyapunov function,

$$\begin{aligned}
V_4 =& V_3 + \frac{z_4^2}{2} \\
\dot{V}_4 =& \dot{V}_3 + z_4 \dot{z}_4 \\
=& z_1 z_2 - k_1 z_1^2 + p_1 z_2 z_3 - k_{2g} z_2^2 - k_{2g1} z_1 z_2 \\
&+ z_2(\alpha_{2r} - \phi_2^T \tilde{p} + \tilde{d}_2(t)) + z_3 z_4 \\
&+ z_3(\alpha_{3r} - \phi_3^T \tilde{p} + \tilde{d}_3(t)) - z_3 \frac{\partial \alpha_2}{\partial \hat{p}} \dot{\hat{p}} \\
&- k_{3g3} z_3^2 - k_{3g2} z_2 z_3 + z_4(\alpha_{4r} - \phi_4^T \tilde{p} + \tilde{d}_4(t)) \\
&- z_4 \frac{\partial \alpha_3}{\partial \hat{p}} \dot{\hat{p}} - k_{4g4} z_4^2 - k_{4g3} z_3 z_4 - k_{4g2} z_2 z_4
\end{aligned} \tag{6.94}$$

The parameter adaptation function is given by,

$$\tau = \sum_{i=2}^{4} \phi_i z_i \tag{6.95}$$

Based on the projection law in Eq. (6.24), the following inequality holds:

$$|\dot{\hat{p}}| = |Proj_{\hat{p}}(\Gamma \tau)| \leq |\Gamma \tau| \leq \sum_{i=2}^{4} |\Gamma \phi_i||z_i| \tag{6.96}$$

Hence the effect of the online time-varying parameter estimation is bounded above by,

$$\left| -z_3 \frac{\partial \alpha_2}{\partial \hat{p}} \dot{\hat{p}} \right| \leq \left| \frac{\partial \alpha_2}{\partial \hat{p}} \right| \left(|\Gamma \phi_2||z_2 z_3| + |\Gamma \phi_3| z_3^2 + |\Gamma \phi_4||z_3 z_4| \right) \tag{6.97}$$

$$\left| -z_4 \frac{\partial \alpha_3}{\partial \hat{p}} \dot{\hat{p}} \right| \leq \left| \frac{\partial \alpha_3}{\partial \hat{p}} \right| \left(|\Gamma \phi_2||z_2 z_4| + |\Gamma \phi_3||z_3 z_4| + |\Gamma \phi_4| z_4^2 \right) \tag{6.98}$$

Hence $\dot{V}_4$ can be rewritten as,

$$\begin{aligned}\dot{V}_4 \leq & z_1 z_2 - k_1 z_1^2 + p_1 z_2 z_3 - k_{2g2} z_2^2 - k_{2g1} z_1 z_2 \\ & + z_3 z_4 - k_{3g3} z_3^2 - k_{3g2} z_2 z_3 - k_{4g4} z_4^2 - k_{4g3} z_3 z_4 - k_{4g2} z_2 z_4 \\ & + \left|\frac{\partial \alpha_2}{\partial \hat{p}}\right| \left(|\Gamma \phi_2| sign(z_2 z_3) z_2 z_3 + |\Gamma \phi_3| z_3^2 + |\Gamma \phi_4| sign(z_3 z_4) z_3 z_4 \right) \\ & + \left|\frac{\partial \alpha_3}{\partial \hat{p}}\right| \left(|\Gamma \phi_2| sign(z_2 z_4) z_2 z_4 + |\Gamma \phi_4| z_4^2 + |\Gamma \phi_3| sign(z_3 z_4) z_3 z_4 \right) \\ & + \sum_{i=2}^{4} z_i (\alpha_{ir} - \phi_i^T \tilde{p} + \tilde{d}_i(t)) \\ = & - \bar{z}_4^T D_z \bar{z}_4 + \sum_{i=2}^{4} z_i (\alpha_{ir} - \phi_i^T \tilde{p} + \tilde{d}_i(t)) \end{aligned} \tag{6.99}$$

where $\bar{z}_4^T = [z_1,\ z_2,\ z_3,\ z_4]$ and D_z is a symmetric matrix given by,

$$D_z = \begin{bmatrix} k_1 & D_{12} & 0 & 0 \\ D_{12} & D_{22} & D_{23} & D_{24} \\ 0 & D_{23} & D_{33} & D_{34} \\ 0 & D_{24} & D_{34} & D_{44} \end{bmatrix} \tag{6.100}$$

where

$$D_{12} = \frac{1}{2}(k_{2g1} - 1) \tag{6.101a}$$

$$D_{22} = k_{2g2} \tag{6.101b}$$

$$D_{23} = \frac{1}{2}\left(k_{3g2} - p_1 - \left|\frac{\partial \alpha_2}{\partial \hat{p}}\right| |\Gamma \phi_2| sign(z_2 z_3) \right) \tag{6.101c}$$

$$D_{24} = \frac{1}{2}\left(k_{4g2} - \left|\frac{\partial \alpha_3}{\partial \hat{p}}\right| |\Gamma \phi_2| sign(z_2 z_4) \right) \tag{6.101d}$$

$$D_{33} = k_{3g3} - \left|\frac{\partial \alpha_2}{\partial \hat{p}}\right| |\Gamma \phi_3| \tag{6.101e}$$

$$D_{34} = \frac{1}{2}\left(k_{4g3} - 1 - \left|\frac{\partial \alpha_2}{\partial \hat{p}}\right| |\Gamma \phi_4| sign(z_3 z_4) - \left|\frac{\partial \alpha_3}{\partial \hat{p}}\right| |\Gamma \phi_3| sign(z_3 z_4) \right) \tag{6.101f}$$

$$D_{44} = k_{4g4} - \left|\frac{\partial \alpha_3}{\partial \hat{p}}\right| |\Gamma \phi_4| \tag{6.101g}$$

The closed-loop system dynamics in terms of tracking errors is given by,

$$\dot{\bar{z}}_4 = A_z \bar{z}_4 + B_{\dot{p}} \dot{\hat{p}} - [\Phi^T \tilde{p} - \tilde{\Delta}] \tag{6.102}$$

where $\Phi = [\phi_2,\ \phi_3,\ \phi_4],\ \tilde{\Delta} = [\tilde{d}_2,\ \tilde{d}_3,\ \tilde{d}_4]^T$, and $A_z, B_{\hat{p}}$ are defined as follows:

$$A_z = \begin{bmatrix} -k_1 & 1 & 0 & 0 \\ -k_{2g1} & -k_2 & p_1 & 0 \\ 0 & -k_{3g2} & -k_3 & 0 \\ 0 & -k_{4g2} & -k_{4g3} & -k_4 \end{bmatrix} \tag{6.103}$$

$$\begin{aligned} k_2 =& k_{2g2} + k_{2r} \\ k_3 =& k_{3g3} + k_{3r} \\ k_4 =& k_{4g4} + k_{4r} \end{aligned}$$

$$B_{\hat{p}} = \left[0,\ 0,\ -\frac{\partial \alpha_2}{\partial \hat{p}},\ -\frac{\partial \alpha_3}{\partial \hat{p}}\right]^T \tag{6.104}$$

6.7.1 Performance of DARC

Theorem : Using the DARC control law and the rate limited adaptation law structure defined above, all signals in the closed-loop system are bounded and the following conditions hold:

(A) The output tracking error has a guaranteed transient performance and a guaranteed final tracking accuracy. Furthermore, the non-negative function $V = \frac{1}{2}\bar{z}_4^T \bar{z}_4$ is bounded above by,

$$V \leq e^{-\lambda t} V(0) + \frac{\epsilon}{\lambda}(1 - e^{-\lambda t}) \tag{6.105}$$

where λ is twice the minimum eigenvalue of D_z and $\epsilon = \epsilon_2 + \epsilon_3 + \epsilon_4$.

(B) In the presence of parametric uncertainties alone (i.e., $\tilde{d} = 0$), the designed control law ensures asymptotic tracking, i.e., $z_1 \to 0$ as $t \to \infty$.

Proof of (A): $\dot{V}$ obtained from Eq. (6.99) is given by,

$$\dot{V} \leq -\bar{z}_4^T D_z \bar{z}_4 + \sum_{i=2}^{4} z_i(\alpha_{ir} - \phi_i^T \tilde{p} + \tilde{d}_i(t)) \tag{6.106}$$

The constants $k_{2g1}, k_{2g2}, k_{3g2}, k_{3g3}, k_{4g2}, k_{4g3}, k_{4g4}$ are chosen such that matrix D_z is always positive definite, i.e., $D_z > 0,\ \forall \bar{z}_4$. Defining $\Lambda = diag(\lambda_1, \lambda_2, \lambda_3, \lambda_4),\ \lambda_1 \geq$

$\lambda_2 \geq \lambda_3 \geq \lambda_4$ where λ_i are the eiqenvalues of D_z and $Q = [q_1, q_2, q_3, q_4]$ as the matrix of corresponding orthogonal eigenvectors, we have

$$\begin{aligned} -\bar{z}_4^T D_z \bar{z}_4 =& -\bar{z}_4^T Q \Lambda Q^T \bar{z}_4 \\ =& -(Q^T \bar{z}_4)^T \Lambda (Q^T \bar{z}_4) \\ =& -\sum_{i=1}^{4} \lambda_i (q_i^T \bar{z}_4)^2 \\ \leq& -\lambda_4 \sum_{i=1}^{4} (q_i^T \bar{z}_4)^2 \\ =& -\lambda_4 \bar{z}_4^T \bar{z}_4 \end{aligned} \tag{6.107}$$

Using Condition 1 in Eq. (6.77a), (6.83a), (6.91a), we obtain

$$\dot{V} \leq -\lambda V + \epsilon \tag{6.108}$$

where $\epsilon = \epsilon_2 + \epsilon_3 + \epsilon_4$ and λ is twice the minimum eigenvalue of D_z. As a result, $\dot{V}$ is negative definite w.r.t. $\bar{z}_4$, achieving asymptotic stability, a guaranteed transient performance and steady-state tracking accuracy.

Proof of (B): In the presence of parametric uncertainties alone ($\tilde{d}_i(t) = 0,\ i = 2, 3, 4$), we define a new function and its derivative as follows.

$$\begin{aligned} V_n =& V + \frac{1}{2} \tilde{p}^T \Gamma^{-1} \tilde{p} \\ \dot{V}_n \leq& -\bar{z}_4^T D_z \bar{z}_4 + \sum_{i=2}^{4} z_i (\alpha_{ir} - \phi_i^T \tilde{p}) + \tilde{p}^T \Gamma^{-1} \dot{\tilde{p}} \end{aligned} \tag{6.109}$$

Applying Condition 2 from Eqs. (6.77b), (6.83b), (6.91b), the parameter adaptation function and update law as defined in Eq. (6.95) and Eq. (6.24), respectively, and Property 2 in Eq. (6.26):

$$\begin{aligned} \dot{V}_n \leq& -\bar{z}_4^T D_z \bar{z}_4 + \tilde{p}^T (\Gamma^{-1} Proj_p(\Gamma \tau) - \tau) \\ \leq& -\bar{z}_4^T D_z \bar{z}_4 \end{aligned} \tag{6.110}$$

From part (A) of the Theorem above, $z_1, z_2, z_3, z_4 \in L_2$. It can be checked from Eqs. (6.72), (6.78), (6.85) and (6.92) that $\dot{z}_1, \dot{z}_2, \dot{z}_3, \dot{z}_4$ are bounded. Using Barbalat's Lemma, we obtain, $V_n \to 0$ as $t \to \infty$. Hence $z_1 \to 0$ as $t \to \infty$.

Table 6.3. Parameter estimate and bounds.

Parameter	**estimate**	**min**	**max**
β_n	1157		
p_1	1	0.95	1.05
p_3	2718.9	2637	2800
p_4	2059.8	1998	2121
p_5	2498.3	2423	2573
p_7	547	556	591

6.7.2 Experimental Results

The parameter estimates, upper and lower bounds for p_1 to p_7, are shown in Table 6.3. Feedback gains were chosen to obtain maximum tracking accuracy without exciting the unmodeled higher-order mode in the system. A closed-loop bandwidth of 10.5Hz was achieved. Figure 6.23 compares the desired trajectory to be tracked with the system output under the proposed controller. The tracking error is shown in Figure 6.24 where a tracking accuracy of 0.3deg was achieved. Most of the tracking error originates from the unmodeled higher-order mode of the motor-drive pulley joint. Figure 6.25 shows the measured motor torque, which is well below the maximum achievable value of 2.1Nm. Figures 6.26-6.29 show the online parameter estimates.

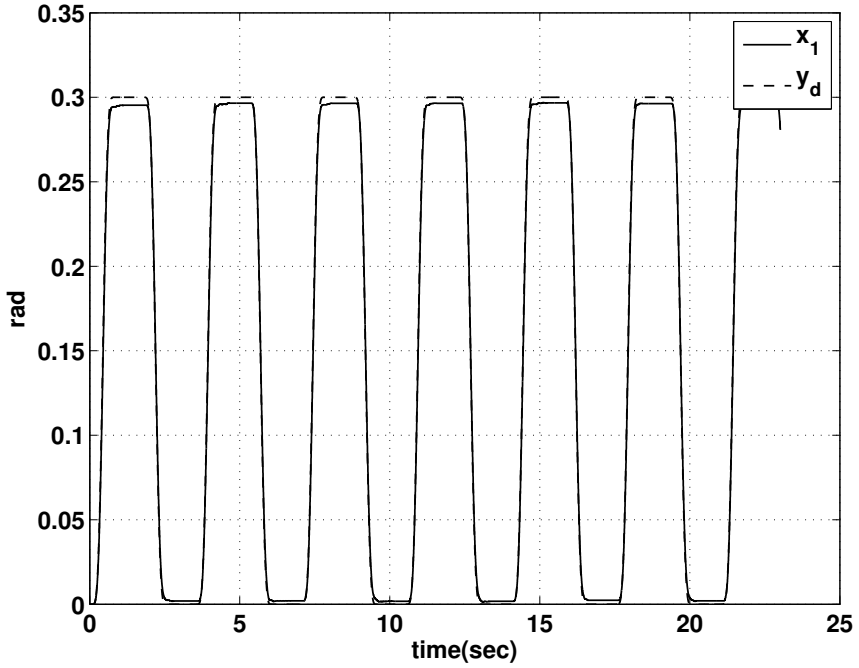

Figure 6.23. Desired trajectory (y_d) and output (x_1).

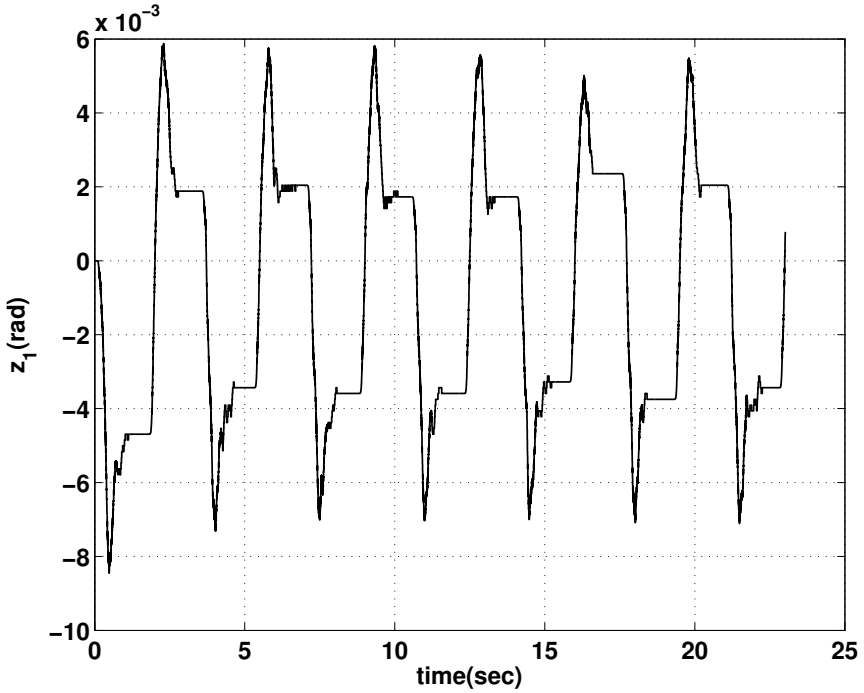

Figure 6.24. Output tracking error.

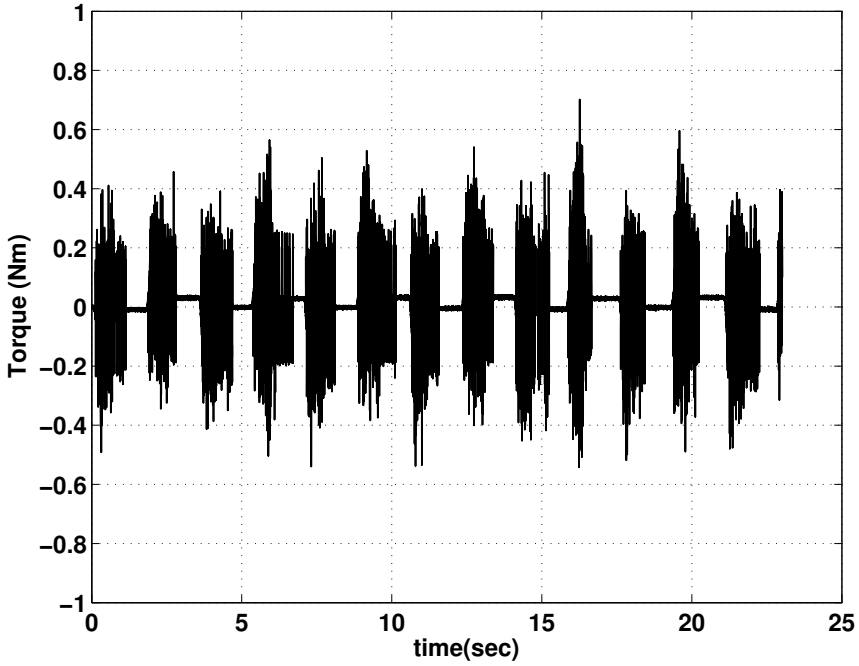

Figure 6.25. Control torque.

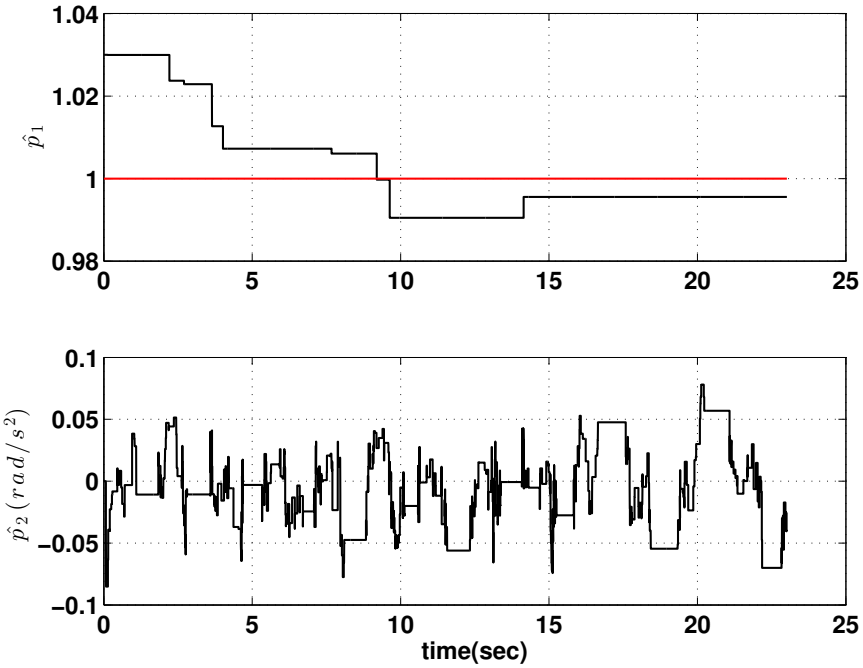

Figure 6.26. Parameter estimates $\hat{p}_1$ and $\hat{p}_2$.

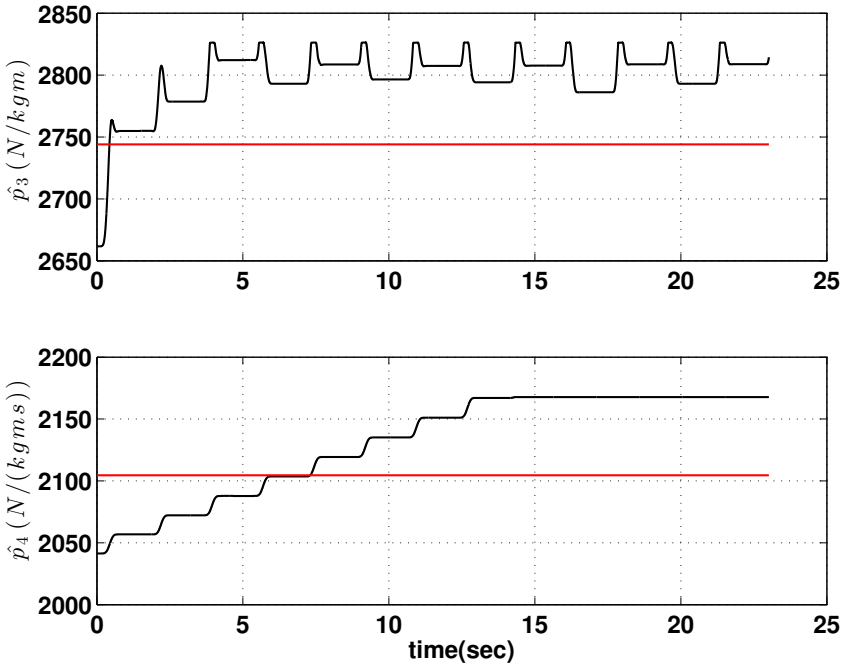

Figure 6.27. Parameter estimates $\hat{p}_3$ and $\hat{p}_4$.

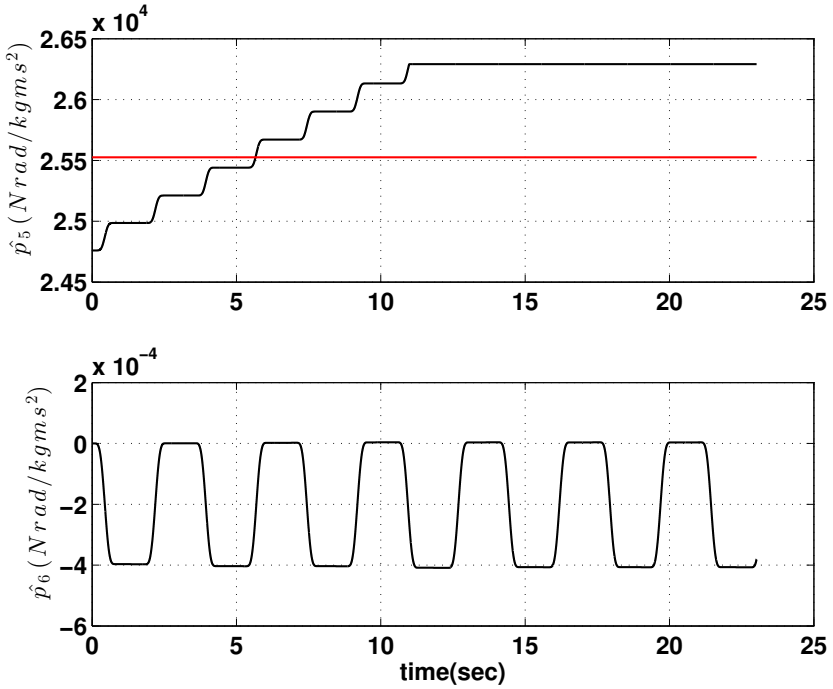

Figure 6.28. Parameter estimates $\hat{p}_5$ and $\hat{p}_6$.

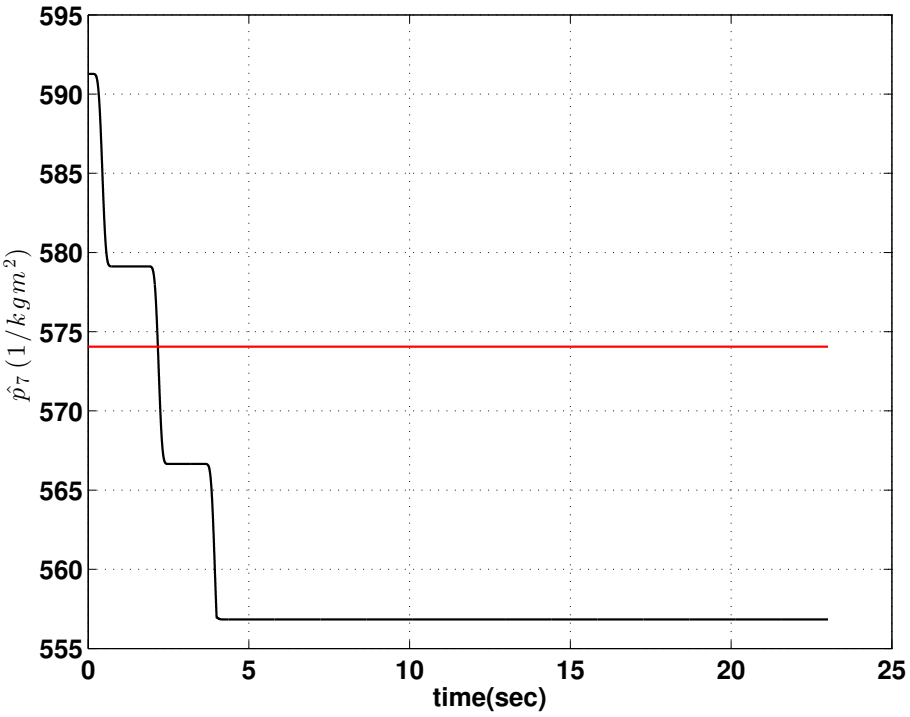

Figure 6.29. Parameter estimate $\hat{p}_7$.

7. CONCLUSIONS AND FUTURE WORK

7.1 Conclusions

Cable-actuated systems provide an effective method for precise motion control over various distances. They are widely used in areas of robotics such as surgical instruments, robotic hands, rehabilitative devices and bio-inspired robots. They are also used in mass transporter systems such as cranes, elevators, cable-cars, 3D printers and cable-mounted cameras. Cable-actuation has many advantages such as high-speed manipulation, larger payloads, larger range of motion, access to remote locations and applications in hazardous environments. They are also easier to transport, assemble/disassemble and reconfigure.

Since the cables used in such systems are inherently flexible, they are prone to vibrations in the axial and transverse directions that can lead to a loss of performance and in the worst case can cause instability. As a result, cable flexibility is an important concern especially in motion control applications requiring high bandwidth or high stiffness since it affects positioning accuracy. In this dissertation, a prototypical cable-pulley system is proposed for motion transmission and the effect of cable flexibility on the system's vibration modes is studied in detail. An analysis of the flexible modes of such a system shows that coupling between cable flexibility and discrete high-inertia pulleys leads to a drastic reduction in the fundamental longitudinal frequency that depends only on the physical properties of the system's components. This was verified experimentally as well.

Since traditional approaches to cable flexibility involved either neglect of or the assumption that the dominant flexible mode of the system is due to joint or link flexibility, the system considered in this work shows that this may indeed not be the case. In high bandwidth applications, the flexible mode due to cable elasticity cannot

be ignored or treated as a lumped model uncertainty and will need to be considered in the overall system model.

Since the cable-pulley system consists of vibrating subsystems, the phenomenon of autoparametric resonance has been studied. It has been shown that under the right design parameters, cable vibrations and pulley rotations can couple strongly. Energy can be exchanged between them leading to a growth in their vibration amplitudes. A parametric analysis shows that the right choice of pulley-to-cable mass ratios and cable tension can help avoid 1:2 internal resonance in the overall system.

Experiments on frequency response of the overall system confirm that the cables behave like axial spring-dampers. Also, the dominant flexible mode of the system is caused by cable elasticity while a higher-order mode is caused by flexible coupling between the drive motor and drive pulley. Knowledge of the system's flexible modes is used to propose simplified lumper parameter models of the overall system. Since the motor-drive pulley joint is a higher-order mode, models are proposed assuming that the joint is either rigid or flexible. A direct adaptive robust controller has been designed to achieve high closed-loop bandwidth and track point-to-point rotation by the load pulley, while assuming matched model uncertainties in the drive motor dynamics. A higher closed-loop bandwidth is achieved when the motor joint flexibility is modeled in contrast with the rigid joint assumption. When cable flexibility is ignored, vibrations are seen in the load pulley output at the dominant frequency when controlled using the direct adaptive robust controller. Both matched uncertainties in the motor dynamics and unmatched uncertainties in the load pulley dynamics are considered in the final controller design. Good tracking accuracy is achieved in the presence of both parametric uncertainties and uncertain nonlinearities such as neglected higher-order modes.

7.2 Future Work

Although key improvements to the modeling and performance of certain types of cable-driven systems have been made in this work, the following suggestions for future improvements are made.

7.2.1 Unmatched Uncertainty Including Motor Joint Flexibility

The final controller designed in Chapter 6 includes matched model uncertainties for a system with flexible cables and a rigid or flexible motor joint as well as and unmatched model uncertainties for a system with flexible cables and a rigid motor joint. Clearly, a higher closed-loop bandwidth is obtainable when both flexible modes are modeled. Hence, an adaptive robust controller could be designed that includes both cable flexibility and motor joint flexibility in the presence of unmatched model uncertainty caused by uncertain load inertia. This is application-specific since the inclusion of the higher-order motor joint flexible mode depends on the required closed-loop bandwidth.

7.2.2 Improved Parameter Estimation

The online parameter estimates using DARC are based on a gradient law with the sole purpose of reducing tracking error. However, in some applications there is a need for highly accurate online parameter estimates. Hence a modified adaptive robust controller could be designed with a different estimation algorithm independent of the tracking error dynamics, e.g., Indirect adaptive robust control (IARC) using a least square estimation algorithm based on plant dynamics.

7.2.3 Cable Transporter System Control

The current work includes a modal analysis applied to a simplified form of cable-transporter systems in an effort to understand the dominant flexible modes. A more

detailed study of the dynamics based on specific applications would be useful for the improvement of performance. For example, aerial cable-cars are generally more complicated vibrating systems subject to wind-induced forces and pendulum-like swinging behavior. Hence their complete analysis requires a more detailed study of the coupling between vibrating subsystems. Also, since the natural longitudinal frequency of such systems changes with position of the transported mass, a more complex controller may be necessary.

LIST OF REFERENCES

LIST OF REFERENCES

[1] L. Dovat, O. Lambercy, R. Gassert, T. Milner, T. Maeder, T.C. Leong, E. Burdet, "A cable-actuated rehabilitation system to train hand function after stroke", *IEEE Trans. Neural Systems and Rehabilitation Engineering*, vol. 16, no. 6, pp. 582-591, 2008.

[2] A.G. Smith and J.R. Hewit, "Control of an experimental robot arm with non-ideal transmission elements", *IEEE Intl. Workshop on Intelligent Motion Control*, 1990, pp. 485-490.

[3] M. Keennon, K. Klingebiel, H. Won, A. Andriukov, "Development of the Nano Hummingbird: A Tailless Flapping Wing Micro Air Vehicle", presented at the 50th AIAA Aero. Sc. Meeting including the New Horizons Forum and Aerospace Exposition, Nashville, Tennessee, Jan 2012.

[4] J. Nagase, N. Saga, T. Satoh, K. Suzumori, "Performance Anthropomorphic Robot Hand with Grasp Force Magnification Mechanism", *Journal of Intelligent Material Systems and Structures*, vol. 23, no. 3, pp. 345-352, 2012.

[5] T. Takaki and T. Omata, "Performace Anthropomorphic Robot Hand with Grasp Force Magnification Mechanism", *IEEE Intl. Conf. Robotics and Automation*, Kobe, Japan, May 2009, pp. 1697-1703.

[6] N.G. Dagakalis et al., "Stiffness study of a parallel link robot crane for shipbuilding applications", *J. Offshore Mech. Arch. Eng.*, vol. 111, no. 3, pp. 183-193, 1989.

[7] H. Kanki, Y. Nekomoto, H. Monobe, H. Ogura, K. Kobayashi, *Development of CMG Active Vibration Control Device for Gondola*, JSME International Journal Series C, Vol. 37, N. 3, pp. 468-470, 1994.

[8] S. Kawamura, H. Kino, C. Won, "High-speed manipulation using parallel wire-driven robots", *Robotica*, vol. 18, no. 3, pp. 13-21, 2000.

[9] A. Riechel, P. Bosscher, H. Lipkin, I. Ebert-Uphoff, "Concept paper: Cable-driven robots for use in hazardous environments", Proc. 10th Int. Top. Meet. Robot Remote Syst. Hazard. Environ., pp. 310-317, 2004.

[10] A.H. Nayfeh and D.T Mook, *Nonlinear oscillations*, New York: Wiley, 1979.

[11] G.F. Carrier, "On the non-linear vibration problem of the elastic string", *Quaterly of Applied Mathematics*, vol. 3, pp. 157-165, 1945.

[12] G.F. Carrier, "A note on the vibrating string", *Quaterly of Applied Mathematics*, vol. 7, pp. 97-101, 1949.

[13] C.A. Coulson and A. Jeffrey, *Waves*, 2 ed. London: Longman, 1977.

[14] P.M. Morse and K.U. Ingard, *Theoretical Acoustics*, New York: McGraw-Hill, 1968.

[15] E.W. Lee, "Non-linear forced vibration of a stretched string", *Br.J. Appl. Phys.*, vol. 8, pp. 411-413, 1957.

[16] G.S.S. Murthy and B.S. Ramakrishna, "Non-linear character of resonance in stretched strings", *J. Acoust. Soc. Am.*, vol. 38, pp. 461-471, 1967.

[17] G.V. Anand, "Large amplitude damped free vibration of a stretched string", *J. Acoust. Soc. Am.*, vol. 45, no. 5, pp. 1089-1096, 1969.

[18] H.P.W. Gottlieb, "Non-linear vibration of a constant-tension string", *J. Sound Vib.*, vol. 143, no. 3, pp. 455-460, 1990.

[19] H.P.W. Gottlieb, "Non-linear, non-planar transverse free vibration of a constant-tension string", *J. Sound Vib.*, vol. 191, no. 4, pp. 563-575, 1996.

[20] R. Narasimha, "Non-linear vibration of an elastic string", *J. Sound Vib.*, vol. 8, no. 1, pp. 134-146, 1968.

[21] E.V. Kurmychev, "Transverse and longitudinal mode coupling in a free vibrating soft string", *Physics Letters A* 310, pp. 148-160, 2003.

[22] A. Watzky, "Non-linear three-dimensional large-amplitude damped free vibration of a stiff elastic stretched string", *J. Sound Vib.*, vol. 153, no. 1, pp. 125-142, 1992.

[23] A. Watzky, "On the nonlinear models of the vibrating string", *J. Acoust. Soc. Am.*, vol. 118, no. 3, pp. 1973, 2005.

[24] Y. Zhang and S. Agrawal, "Coupled vibrations of a varying length flexible cable transporter system with arbitrary axial velocity", *Proc. Am. Control Conf.*, 2004.

[25] C.D. Mote, "A study of band saw vibrations", *J. Franklin Inst.*, vol. 279, pp. 430-444, 1965.

[26] C.D. Mote, "Vibration coupling in continuous belt and band systems", *J. Sound Vib.*, vol. 102, no. 1, pp. 1-9, 1985.

[27] C.D. Mote, "Vibration coupling analysis of band/wheel mechanical systems", *J. Sound Vib.*, vol. 109, no. 2, pp. 237-258, 1986.

[28] S.J. Hwang, N.C. Perkins, A.G. Ulsoy, R. Meckstroth, "Rotational response and slip prediction of serpentine belt drive systems", *ASME Journal of Vibration and Acoustics*, vol. 116, no. 1, pp. 71-78, 1994.

[29] R.S. Beikmann, N.C. Perkins and A.G. Ulsoy, "Free vibration of serpentine belt drive systems", *ASME Journal of Vibration and Acoustics*, vol. 118, pp. 406-413, 1996.

[30] R.S. Beikmann, N.C. Perkins and A.G. Ulsoy, "Nonlinear coupled vibration response of serpentine belt drive systems", *ASME Journal of Vibration and Acoustics*, vol. 118, pp. 567-574, 1996.

[31] J.W. Strutt, "On maintained vibrations", *Philosophical Magazine*, vol. 15, pp. 229-235, 1883.

[32] J.W. Strutt, "On maintenance of vibrations by forces of double frequency and on the propagation of waves through a medium endowed with periodic structure", *Philosophical Magazine*, vol. 24, pp. 145-159, 1887.

[33] J.A. Elliot, "Intrinsic nonlinear effects in vibrating strings", *Am. J. Phys.*, vol. 48, no. 6, pp. 478-480, 1980.

[34] J.A. Elliot, "Nonlinear resonance in vibrating strings", *Am. J. Phys.*, vol. 50, no. 12, pp. 1148-1150, 1982.

[35] G.V. Rao and R.N. Iyengar, "Internal Resonance and Non-linear Response of a Cable Under Periodic Excitation", *J. Sound. Vib.*, vol. 149, no. 1, pp. 25-41, 1991.

[36] A. Tondl, T. Ruijgrok, F. Verhulst, R. Nabergoj, *Autoparametric Resonance in Mechanical Systems*, Cambridge University Press, 2000.

[37] A. van der Burgh, "On the asymptotic solutions of the differential equations of the elastic pendulum", *Journal de Mécanique*, vol. 7, no. 4, pp.507-520, 1968.

[38] Y. Xia, Y. Fujino, Auto-parametric vibration of a cable-stayed-beam structure under random excitation, *J. Engineering Mechanics*, vol. 132, no. 3, pp. 279-286, 2006.

[39] J. Bhardhwaj, B. Yao and A. Raman, "Auto-parametric resonance in cable-actuated systems", *IEEE Intl. Conf. Robotics and Automation*, Hong Kong, June 2014.

[40] M. Zeinali, A. Khajepour, "Design and application of chattering-free sliding mode controller to cable-driven parallel manipulators: Theory and Experiment", ASME Mechanisms and Robotics Conference, 2010.

[41] A. Trevisani, P. Gallina, R.L. Williams II, "Cable-direct-driven robot (CDDR) with passive SCARA sup- port: theory and simulation", *J Intell Robot Syst*, vol. 46, pp. 73-94, 2006.

[42] M.H. Korayem, H.T. Bamdad, "Dynamic load carrying capacity of flexible cable suspended robot: Robust feedback linearization control approach", *J Intell Robot Syst*, vol. 60, pp. 341-363, 2010.

[43] P. Pitakwatchara, "Modelling and control of the multi-stage cable pulley-driven flexible-joint", *Intl. J. Advanced Robotic Systems*, vol. 11, no. 118, 2014.

[44] S. Behzadipour, A. Khajepour, "Stiffness of cable-based parallel manipulators with applications to stability analysis", *J. Mech. Des.*, vol. 128, no. 1, pp. 303-310, 2006.

[45] X. Diao, O. Ma, "Vibration analysis of cable-driven parallel manipulators", *Multibody Syst Dyn*, vol. 21, pp.347-360, 2009.

[46] M.A. Khosravi, H.D. Taghirad, "On the modeling and control of fully constrained cable-driven robots with flexible cables", 2nd Intl. Conf. Control, Instr. and Automation, pp. 1030-1035, 2011.

[47] M.A. Khosravi, H.D. Taghirad,, "Dynamic Modeling and Control of Parallel Robots With Elastic Cables- Singular Perturbation Approach", *IEEE Trans. on Robotics*, vol. 30, no. 3, pp. 694-704, 2014.

[48] S.S. Sergev and W.D. Iwan, *The Natural Frequencies and Mode Shapes of Cables with Attached Masses*, Journal of Energy Resources Technology, Vol. 103, pp. 237-242, 1981.

[49] J-S. Wu, C-C. Chen, *The dynamic analysis of a suspended cable due to a moving load*, Intl. J. Numerical Methods in Engineering, Vol. 28, pp. 2361-2381, 1989.

[50] H.P. Lin and N.C. Perkins, *Free vibration of complex cable/mass systems: Theory and Experiment*, J. Sound Vib., Vol. 179, No. 1, pp. 131-149, 1995.

[51] J.M.W. Brownjohn, *Dynamics of an aerial cableway system*, Engineering Structures, Vol. 20, No. 9, pp.826-836, 1998.

[52] D. Bruno, A. Leonardi, *Nonlinear structural models in cableway transport systems*, Simulation Practice and Theory 7, pp. 207-218, 1999.

[53] Y-M. Wang, *The transient dynamics of a cbale-mass system due to motion of an attached accelerateting mass*, Intl. J. Solids and Structures 37, pp. 1361-1383, 2000.

[54] H.C. Renezeder, A. Steindl and H. Troger, *On the dynamics of circulating mono cable aerial ropeways*, Proc. Appl. Math. Mech. 5, pp. 123-124, 2005.

[55] A. Sofi, G. Muscolino, *Dynamic analysis of suspended cables carrying moving oscillators*, Intl. J. Solids and Structures 44, pp. 6725-6743, 2007.

[56] K. Hoffmann, *Oscillation effects of ropeways caused by cross-wind and other influences*, FME Transactions 37, pp. 175-184, 2009.

[57] H.R. Pota, S.K. Agrawal, Y. Zhang, "A flatness based approach to trajectory modification of residual motion of cable transporter systems", *J. Sound. Vib.*, vol. 10, pp. 1441-1457, 2004.

[58] Y. Zhang ,S.K. Agrawal, H.R. Pota and I.R. Petersen, "Minimax linear quadratic gaussian control of longitudinal vibration for cable transporter systems with multiplicative nonparametric uncertainties", *International Journal of Acoustics and Vibration*, Vol. 10, No. 3, pp. 1-7, 2005.

[59] Y. Zhang ,S.K. Agrawal, P. Hagedorn, "Longitudinal vibration modeling and control of flexible transporter system with arbitrarily varying cable lengths", *Journal of Vibration and Control*, Vol. 11, No. 3, pp. 431-456, 2005.

[60] C.F. Baicu, C.D. Rahn, B.D. Nibali, "Active boundary control of elastic cables: Theory and experiment", *Journal of Sound and Vibration*, Vol. 198, No. 1, pp. 17-26, 1996.

[61] S.M. Shahruz, C.A. Narasimha, "Suppression of vibration in stretched strings by boundary control", *Journal of Sound and Vibration*, Vol. 204, No. 5, pp. 835-840, 1997.

[62] H. Canbolat, D. Dawson, C. Rahn, S. Nagarkatti, "Adaptive boundary control of out-of-plane cable vibration", *Journal of Applied Mechanics*, Vol. 65, pp. 963-969, 1998.

[63] F. Zhang, D.M. Dawson, S.P. Nagarkatti, C.D. Rahn, "Boundary control for a general class of non-linear string-actuator systems", *Automatica*, Vol. 38, pp. 821-827, 2002.

[64] Y. Zhang, S.K. Agrawal, "Lyapunov controller design for transverse vibration of a cable-linked transporter system", *Multibody System Dynamics*, Vol. 15, pp. 287-304, 2006.

[65] L. Lu, Z. Chen, B. Yao, Q. Wang, A two-loop performance-oriented tip tracking control of a linear motor driven flexible beam system with experiments, *IEEE Trans. Industrial Electronics*, vol. 3, no. 3, 2011

[66] J.A. Wickert, C.D. Mote, "Classical vibration analysis of axially moving continua", *Transactions of ASME*, Vol. 57, pp. 738-744, 1990.

[67] S.M. Shahruz, D.A. Kurmaji, "Vibration suppression of non-linear axially moving string by boundary control", *Journal of Sound and Vibration*, Vol. 201, No. 1, pp. 145-152, 1997.

[68] Z. Qu, "An iterative learning algorithm for boundary control of a stretched moving string", *Automatica*, Vol. 38, pp. 821-827, 2002.

[69] Q.C Nguyen, K-S Hong, "Asymptotic stabilization of a nonlinear axially moving string by adaptive boundary control", *Journal of Sound and Vibration*, Vol. 329, pp. 4588-4603, 2010.

[70] K. Hamamoto and T. Sugie, Controller design of 2 mass-spring system via LMI, Proc. 35th Conf. on Decision and Control, pp. 745-746, 1996.

[71] M. Kawanishi, T. Yada and T. Sugie, Controller design of 2 mass-spring system based on BMI optimization, Proc. 35th Conference on Decision and Control, pp. 2363-2364, 1996.

[72] R. Braatz, M. Morari, "Robust control for a noncolloacted spring-mass system", *Journal of Guidance, Control and Dynamics*, vol. 15, no. 5, pp. 1103-1110, 1992.

[73] M. Sznaier and H. Rotstein, "Robust Controller Design for a Collocated Spring-Mass System Via Mixed l_∞/H_∞*Optimization*", *Intl. J. Robust and Nonlinear Control*, vol. 5, pp. 53-65, 1995.

[74] W. Reinelt, "Robust control of a two-mass-spring system subject to input constraints", Proc. American Control Conference, pp. 1817-1821, 2000.

[75] J. Xu, P. Yu, T. Zhang, R. Guo, "Design of torsional vibration controller for motor-gearbox/differential drive system of electric vehicles", *Applied Mechanics and Materials*, vol. 437, pp. 56-61, 2013.

[76] Y. Konishi, N. Araki, K. Tadokoro, H. Ishigaki, "Positioning control of a 2-mass spring system with static and kinetic friction using hybrid controller", *Intl. J. Innovative Computing, Information and Control*, vol. 5, no. 10(B), pp. 3341-3349, 2009.

[77] K-Z. Liu, S. Namiki, H. Ishii, Velocity control of 2-mass-spring systems with large load uncertainty-An adaptive backstopping control approach, Proc. 42nd Conference on Decision and Control, pp. 3948-3953, 2003.

[78] B. Yao and M. Tomizuka, "Adaptive robust control of MIMO nonlinear systems in semi-strict feedback forms", *Automatica*, vol. 37, no. 9, pp. 1305-1321, 2001.

[79] J. Bhardhwaj and B. Yao, "Direct adaptive robust control of cable-pulley system", *Proc. American Control Conference*, Chicago, July 2015.

[80] R. Courant, K. Friedrichs, H. Lewy, "On the partial difference equations of mathematical physics", *IBM Journal of Research and Development*, vol. 11, no. 2, pp. 215-234, 1967.

[81] I. Celik and W.-M. Zhang, "Calculation of numerical uncertainty using Richardson Extrapolation: Application to some simple turbulent flow calculations", *J. Fluids Engineering, Transactions of ASME*, vol. 117, no. 3, pp. 439-435, 1995.

[82] A.A. Alexeenko, "Numerical Error Analysis for Deterministic Kinetic Solutions of Low-Speed Flows", *Proceedings of 25th International Symposium on Rarefied Gas Dynamics*, St. Petersburg, Russia, July 21-28, 2006.

[83] L. Ljung, *System Identification: Theory for the User*, 2nd ed, Upper Saddle River, NJ Prentice Hall, 1999.

[84] M.C. Readman, *Flexible Joint Robots*, CRC Press, 1994.

APPENDIX

A. HARDWARE SPECIFICATIONS

Table A.1. Motor characteristics.

RE 50 50 mm, Graphite Brushes, 200 Watt	**$ 592.38**
Motor length	108 mm
Outer diameter	50 mm
Values at Nominal Voltage	
Nominal Voltage	24.0 V
No load speed	5950.0 rpm
No load current	236.0 mA
Nominal speed	5680.0 rpm
Nominal torque (max. continuous torque)	405.0 mNm
Nominal current (max. continuous current)	10.8 A
Stall torque	8920.0 mNm
Starting current	232.0 A
Max. efficiency	93.8
Characteristics	
Terminal inductance	0.072 mH
Terminal resistance	0.103
Torque constant	38.5 mNm / A
Speed / torque gradient	0.668 rpm / mNm
Mechanical time constant	3.75 ms
Rotor inertia	536.0 gcm^2
Speed constant	248.0 rpm / V

Table A.2. Motor shaft encoder characteristics.

Encoder HEDL 5540, Line Driver RS 422	**$ 131.5**
Number of channels	3.0
Counts per turn	500.0
Max. speed	12000.0 rpm

Table A.3. Gearhead characteristics.

Planetary Gearhead GP 62 A 62 mm, 8 - 50 Nm	**$ 544**
Reduction	5.2
Number of stages	1.0
Intermittently permissible torque at gear output	12.0 Nm
Average backlash no load	1.0^o
Mass inertia	109.0 gcm^2
Weight	950 g
Max. motor shaft diameter	8 mm
Outer diameter	62 mm
Measurement from flange	24 mm
Recommended input speed	3000.0 rpm

VITA

VITA

Jayender Bhardhwaj was born in Chennai, India in 1983. He received his Bachelor's degree in Aerospace Engineering in June 2006 from Indian Institute of Technology Madras, India and his Master's degree in Aeronautics and Astronautics from Stanford University, Stanford in June 2008. He started his Doctoral study at the School of Mechanical Engineering at Purdue University, under the guidance of Prof. Bin Yao. In August 2015, he received his PhD degree for his research on the modeling and adaptive robust control of cable-actuated systems used for motion transmission. His research interests include system modeling, adaptive robust control and robotics.